

Review

Application of Porous Materials for CO₂ Reutilization: A Review

Amir Masoud Parvanian ^{1,*}, Nasrin Sadeghi ², Ahmad Rafiee ³, Cameron J. Shearer ⁴ and Mehdi Jafarian ^{5,*}¹ Department of Mechanical Engineering, Faculty of Engineering, University of Isfahan, Isfahan 81746-73441, Iran² Department of Chemical Engineering, Laval University, Quebec, QC G1V 0A8, Canada; nasrin.sadeghi-sarab-ghanbari.1@ulaval.ca³ Chemical Engineering Department, Faculty of Engineering, Ferdowsi University of Mashhad, Mashhad 91779-48974, Iran; ahmadrafiee@um.ac.ir⁴ Department of Chemistry, School of Physical Sciences, The University of Adelaide, Adelaide, SA 5005, Australia; cameron.shearer@adelaide.edu.au⁵ Centre for Energy Technology, School of Mechanical Engineering, The University of Adelaide, Adelaide, SA 5005, Australia

* Correspondence: a.parvanian@ma.iut.ac.ir (A.M.P.); mehdi.jafarian@adelaide.edu.au (M.J.); Tel.: +98-31-3793-2685 (A.M.P.); +61-8-8313-2306 (M.J.)

Abstract: CO₂ reutilization processes contribute to the mitigation of CO₂ as a potent greenhouse gas (GHG) through reusing and converting it into economically valuable chemical products including methanol, dimethyl ether, and methane. Solar thermochemical conversion and photochemical and electrochemical CO₂ reduction processes are emerging technologies in which solar energy is utilized to provide the energy required for the endothermic dissociation of CO₂. Owing to the surface-dependent nature of these technologies, their performance is significantly reliant on the solid reactant/catalyst accessible surface area. Solid porous structures either entirely made from the catalyst or used as a support for coating the catalyst/solid reactants can increase the number of active reaction sites and, thus, the kinetics of CO₂ reutilization reactions. This paper reviews the principles and application of porous materials for CO₂ reutilization pathways in solar thermochemical, photochemical, and electrochemical reduction technologies. Then, the state of the development of each technology is critically reviewed and evaluated with the focus on the use of porous materials. Finally, the research needs and challenges are presented to further advance the implementation of porous materials in the CO₂ reutilization processes and the commercialization of the aforementioned technologies.



Citation: Parvanian, A.M.; Sadeghi, N.; Rafiee, A.; Shearer, C.J.; Jafarian, M. Application of Porous Materials for CO₂ Reutilization: A Review. *Energies* **2022**, *15*, 63. <https://doi.org/10.3390/en15010063>

Academic Editors: Federica Raganati and Paola Ammendola

Received: 13 November 2021

Accepted: 11 December 2021

Published: 22 December 2021

Publisher's Note: MDPI stays neutral with regard to jurisdictional claims in published maps and institutional affiliations.



Copyright: © 2021 by the authors. Licensee MDPI, Basel, Switzerland. This article is an open access article distributed under the terms and conditions of the Creative Commons Attribution (CC BY) license (<https://creativecommons.org/licenses/by/4.0/>).

1. Introduction

The rising atmospheric concentration of greenhouse gases (GHGs), largely due to anthropogenic emissions, is widely associated with the simultaneous rise in the global mean temperature [1,2]. The most abundant GHGs in the Earth's atmosphere are water vapor (H₂O), carbon dioxide (CO₂), methane (CH₄), oxides of nitrogen (NO₂, NO, etc.), ozone (O₃), and chlorofluorocarbons (CFCs). While CH₄ and CFCs have a higher green-house gas effect per their unit mass than CO₂ [3], CO₂ has the major contribution to the global warming [4], owing to its larger amount in the atmosphere. The CO₂ concentration in the atmosphere has increased significantly from approximately 280 ppm in the pre-industrial times to nearly 414.5 ppm in August 2021 [5], which is mainly due to the global dependency on the fossil fuels for power production, as shown in Figure 1 [6]. However, at present, despite the urgent need to decrease CO₂ emissions, fossil fuels are still used for > 80% of the world energy demand and are expected to remain the predominant source of energy for the short to medium term, due to their low cost, availability, high energy density, existing

reliable technology, and established position worldwide [7]. Nevertheless, if no action is taken, the world would be around 4 °C warmer by the end of this century than it was at the beginning of the industrial revolution, which is anticipated to lead to significantly serious catastrophic effects on climate [8]. On this basis, the Paris Agreement (2015) was created to strengthen the global response to the threat of climate change, restricting global temperature rise to well below 2 °C in this century and preferably below 1.5 °C, which is considered as the limit to prevent the most catastrophic changes on earth [9,10]. However, to meet this need, the CO₂ concentration in the atmosphere should not exceed 450 ppm, or more than ~10% over the current concentration [10]. Therefore, there is an urgent need to develop technologies enabling the reduction in CO₂ emissions, while also reducing the substantial economic and/or political challenges that favor ‘business-as-usual’ technologies.

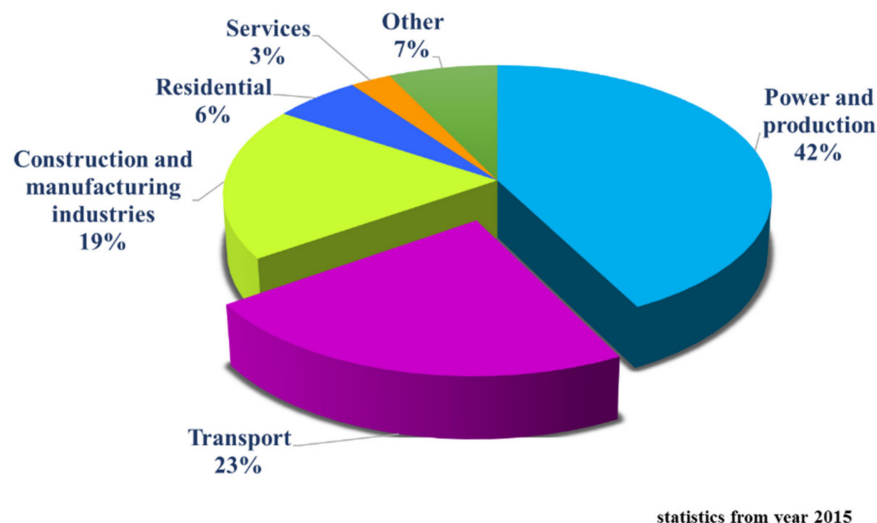


Figure 1. Anthropogenic CO₂ sources and their contribution to the total CO₂ emissions, adapted with permission from [6].

To mitigate the CO₂ emissions, the most prospective options are to reduce energy consumption (through increasing the efficiency of energy conversion and/or utilization systems), to switch to non-fossil based and renewable energy sources such as wind, solar and biomass, and, finally, to utilize Carbon Capture Storage/Reutilization (CCS/CCR) [11]. The motivation behind the development of CCS and CCR is to minimize the effect of CO₂ emission on global climate change, while also keeping the low-cost, carbon-based infrastructure. CCS and CCR typically comprise three main stages: capturing CO₂ at the generation point, e.g., power plants, compressing it to a concentrated fluid, and, lastly, either storing it in a safe and secure place, e.g., oil and gas reservoirs, or reutilizing it for the production of other chemicals. CCS can be also performed to enhance the oil and gas recovery through the injection of the captured CO₂ into the oil and gas reservoirs [6,12]. However, it is typically site and geology specific. By contrast, CCR offers the potential for value proposition, as the separated CO₂ is utilized as a valuable raw material for chemical commodity production. Commensurate with this, currently approximately 3600 Mtonnes of CO₂ are used globally as a feedstock in extensive variety of industries, e.g., urea, formaldehyde, and dimethyl ether (DME) production and methanol synthesis [13]. Figure 2 provides a list of the main industries in which CO₂ is used as feedstock and their share from the global usage [6]. Government policies, such as a carbon tax, are expected to be implemented in the coming years and would subsequently lead to the availability of CO₂ at a low or even negative price. Consequently, in addition to current technologies, the need for new technologies enabling CO₂ conversion to other valuable products is expected to increase.

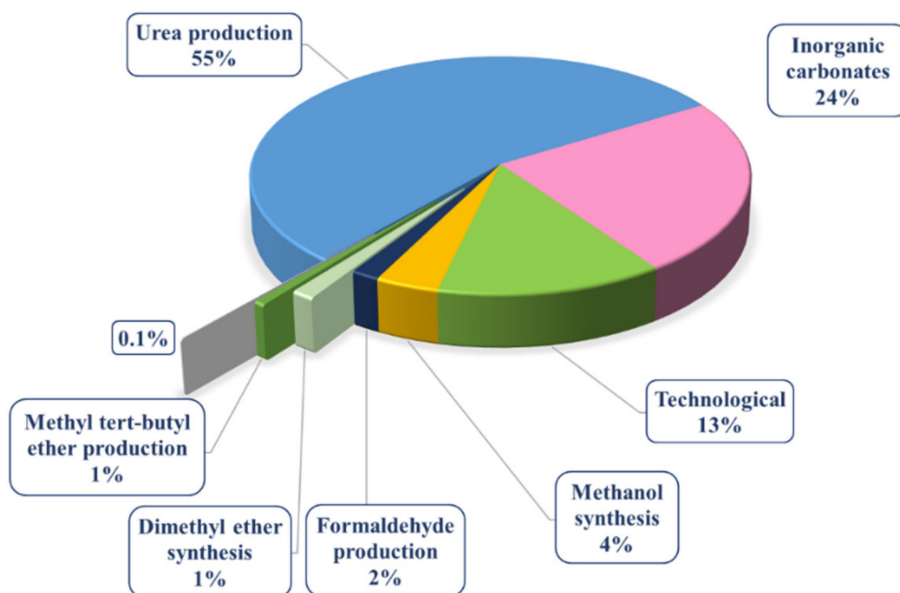


Figure 2. Industries that utilize CO₂ as a feedstock, adapted with permission from [6].

Table 1 summarizes some of the main CO₂ reutilization (CDR) processes. The state of development and the chemical reactions employed in these technologies are also listed in Table 1 of these technologies, solar thermochemical, photocatalytic, and electrochemical are still under development, while the rest are commercially available. This review paper focuses mainly on thermochemical, photocatalytic, and electrochemical CDR technologies. In each of these technologies, surface-dependent reactions are vital and, therefore, high surface area materials are employed as the catalyst reactant, substrate, or a combination of these [14–18]. Beyond just surface area, the material design in these processes has been considered as a key factor influencing the performance and techno-economic viability [19–22].

Several review papers have been published on CO₂ utilization through solar thermochemical, photochemical, and electrochemical reduction reactions. In 2010, Loutzenhiser et al. [23] reviewed the two-step solar thermochemical cycles for H₂O and CO₂ splitting with ZnO/Zn reduction and oxidation (RedOx) reactions to produce synthesis gas. They provided an outline of the underlying science and the technological advances in solar reactor engineering with Second-law, life cycle, and economic analyses. Their second-law analysis indicated the potential of achieving high solar-to-chemical energy conversion efficiencies and, consequently, economic competitiveness vis-à-vis other routes for producing solar fuels from H₂O and CO₂. This is despite that several other materials, i.e., ceria oxides, and perovskites have been recently developed and analyzed for CO₂ splitting. Kovačić et al. [24] reviewed the theoretical first principles of photocatalytic CO₂ reduction and presented the fundamentals of reaction and doping, with theoretical description including electronic calculations, kinetic modelling, macroscale simulations, calculated electronic properties, CO₂ adsorption on photoactive materials, and reaction mechanisms. Strategies to improve efficiency of the fuels' production via TiO₂-based photocatalytic CO₂ reduction were reviewed by Shehzad and co-workers [25]. They addressed the fundamentals and developments in the TiO₂-based reduction systems and covered the thermodynamics of CO₂ reduction, mass transfer of reacting compounds, selectivity of solar products, and reaction mechanism of photocatalytic CO₂ reduction. Ola and Maroto-Valer [26] reviewed the state of the art in photocatalytic CO₂ reduction over titanium oxide (TiO₂)-nanostructured materials up to 2015, with emphasis on material design and reactor configurations. Various surface modification methods, e.g., impurity doping, metal deposition, carbon-based material loading, etc., for CO₂ reduction over TiO₂ were also reviewed by Low et al. [27]. Moreover, aqueous electrochemical reduction of

CO_2 over Cu electrodes was reviewed by Gattrell et al. [28] in 2006. The dependence of the hydrocarbon products on the reaction conditions were discussed. Catalysts and reactors for CO_2 photoconversion over the metal oxides were covered by Lie et al. [29]. Some important factors including particle size, surface area, and controlling the facets for efficient CO_2 photoreduction, and reactor design were highlighted. Reaction kinetics for photoreduction of CO_2 were covered by Thompson et al. [30] in 2014. Micro-kinetic, analytics, modeling approaches, and impact of parameters on CO_2 photoreduction kinetics were discussed. Nonetheless, there is lack of a comprehensive review papers that cover the recent advances in the fields of thermochemical, photochemical, and electrochemical reduction reactions, which all rely on the use of porous structures and catalysts. This paper aims to address this gap. The paper also aims to identify technology development challenges and the required research to further advance the commercialization of the processes.

Table 1. The main CDR processes utilize CO_2 as a feedstock.

CDR Route	Main Chemical Reactions	Comments	References
Dry reforming for syngas production	$\text{CO}_2 + \text{CH}_4 \rightleftharpoons 2\text{CO} + 2\text{H}_2$ $\text{CO} + \text{H}_2\text{O} \rightleftharpoons \text{CO}_2 + \text{H}_2$	Commercially available	[12,31–36]
CO_2 hydrogenation for methanol production	$\text{CO} + 2\text{H}_2 \rightleftharpoons \text{CH}_3\text{OH}$ $\text{CO}_2 + 3\text{H}_2 \rightleftharpoons \text{CH}_3\text{OH} + \text{H}_2\text{O}$ $\text{CO} + \text{H}_2\text{O} \rightleftharpoons \text{CO}_2 + \text{H}_2$	Commercially available	[37–42]
CO_2 hydrogenation to DME	$\text{CO}_2 + 3\text{H}_2 \rightleftharpoons \text{CH}_3\text{OH} + \text{H}_2\text{O}$ $\text{CO} + 2\text{H}_2 \rightleftharpoons \text{CH}_3\text{OH}$ $\text{CO} + \text{H}_2\text{O} \rightleftharpoons \text{CO}_2 + \text{H}_2$ $2\text{CH}_3\text{OH} \rightleftharpoons \text{CH}_3\text{OCH}_3 + \text{H}_2\text{O}$	-	[40,43–45]
Urea production	$2\text{NH}_3 + \text{CO}_2 \rightleftharpoons \text{H}_2\text{N}-\text{COONH}_4$ $\text{H}_2\text{N}-\text{COONH}_4 \rightleftharpoons (\text{NH}_2)_2\text{CO} + \text{H}_2\text{O}$	Commercially available	[46–48]
Polyethercarbonate polyols	Propylene oxide ($\text{C}_3\text{H}_6\text{O}$) + $\text{CO}_2 \rightarrow$ Polyethercarbonate polyols	Commercially available	[49]
Fischer–Tropsch (FT) synthesis by dry reforming of natural gas	$n\text{ CO} + 2n\text{H}_2 \rightarrow (-\text{CH}_2-) + n\text{H}_2\text{O}$	Commercially available	[12,36,50–52]
Solar thermochemical	$\text{MO}_{\text{oxidized}} + (\Delta\text{H}) \rightarrow \text{MO}_{\text{reduced}} + 1/2 \text{O}_2(\text{g})$ $\text{MO}_{\text{reduced}} + \text{H}_2\text{O}/\text{CO}_2(\text{g}) \rightarrow \text{MO}_{\text{oxidized}} + \text{H}_2/\text{CO}(\text{g}) + (\Delta\text{H})$	Under development	[19,53,54]
Photochemical (During light irradiation, the energy of photons is absorbed. Excite electron/hole pairs are produced, which reduce and oxidize the chemical species over the surface of the photocatalyst.)	$\text{CO}_2 + 2\text{H}^+ + 2\text{e}^- \rightarrow \text{HCO}_2\text{H}$ $\text{CO}_2 + 2\text{H}^+ + 2\text{e}^- \rightarrow \text{CO} + \text{H}_2\text{O}$ $\text{CO}_2 + 2\text{H}^+ + 4\text{e}^- \rightarrow \text{HCHO} + \text{H}_2\text{O}$ $\text{CO}_2 + 6\text{H}^+ + 6\text{e}^- \rightarrow \text{CH}_3\text{OH} + \text{H}_2\text{O}$ $\text{CO}_2 + 8\text{H}^+ + 8\text{e}^- \rightarrow \text{CH}_4 + 2\text{H}_2\text{O}$ $2\text{CO}_2 + 12\text{H}^+ + 12\text{e}^- \rightarrow \text{C}_2\text{H}_5\text{OH} + 3\text{H}_2\text{O}$	Under development	[55–58]
Electrochemical (In this process, a chemical reaction occurs by the applied electrical current. It involves oxidation–reduction reactions where CO_2 is reduced on the cathode and oxygen evolves at the anode.)	$\text{CO}_2 + 2\text{H}^+ + 2\text{e}^- \rightarrow \text{HCO}_2\text{H}$ $\text{CO}_2 + 2\text{H}^+ + 2\text{e}^- \rightarrow \text{CO} + \text{H}_2\text{O}$ $\text{CO}_2 + 2\text{H}^+ + 4\text{e}^- \rightarrow \text{HCHO} + \text{H}_2\text{O}$ $\text{CO}_2 + 6\text{H}^+ + 6\text{e}^- \rightarrow \text{CH}_3\text{OH} + \text{H}_2\text{O}$ $\text{CO}_2 + 8\text{H}^+ + 8\text{e}^- \rightarrow \text{CH}_4 + 2\text{H}_2\text{O}$ $2\text{CO}_2 + 12\text{H}^+ + 12\text{e}^- \rightarrow \text{C}_2\text{H}_4 + 4\text{H}_2\text{O}$	Under development	[59–61]

In the first part of the paper, different materials for solar thermochemical RedOX reactions together with the associated developed reactors are reviewed. In the following parts of the paper, two types of porous materials, namely, TiO_2 as the most common porous material and metal-organic frameworks (MOFs) as new classes of hybrid porous materials,

are investigated for photochemical and electrochemical CDR reactions. Furthermore, methods for modification and improving the performance of these materials are discussed.

2. Solar Thermochemical Conversion

The solar thermochemical CO₂ conversion process applies solar thermal energy absorbed via Concentrated Solar Power (CSP) technology to reutilize CO₂ and convert it to value-added chemicals such as carbon monoxide (CO), diesel (C₁₀H₂₀–C₁₅H₃₂), kerosene (C₁₂H₂₆–C₁₅H₃₂), etc. through commercially available catalytic processes [62]. The CSP thermal energy is supplied via reflective surfaces, used to concentrate the solar irradiation into a focal point, where the solar receiver/reactor is typically located. The CSP solar irradiance is measured by a unit called “sun” = 1 kW m⁻² and several suns can lead to temperatures higher than 1000 °C [63]. As depicted schematically in Figure 3, CSP can be employed as a high-temperature heat source for the thermochemical two-step RedOx reactions. In the first step, the metal oxide MO_δ is reduced through an endothermic reaction (Equation (1)). Then the reduced metal oxide MO_{δ-1} reacts exothermically with CO₂, producing CO and MO_δ (Equation (2)). This is a chemical looping process in which the metal oxide is employed as the oxygen carrier being reduced and re-oxidized by CO₂ as an oxidant. The process typically produces O₂ as a by-product (Figure 3).

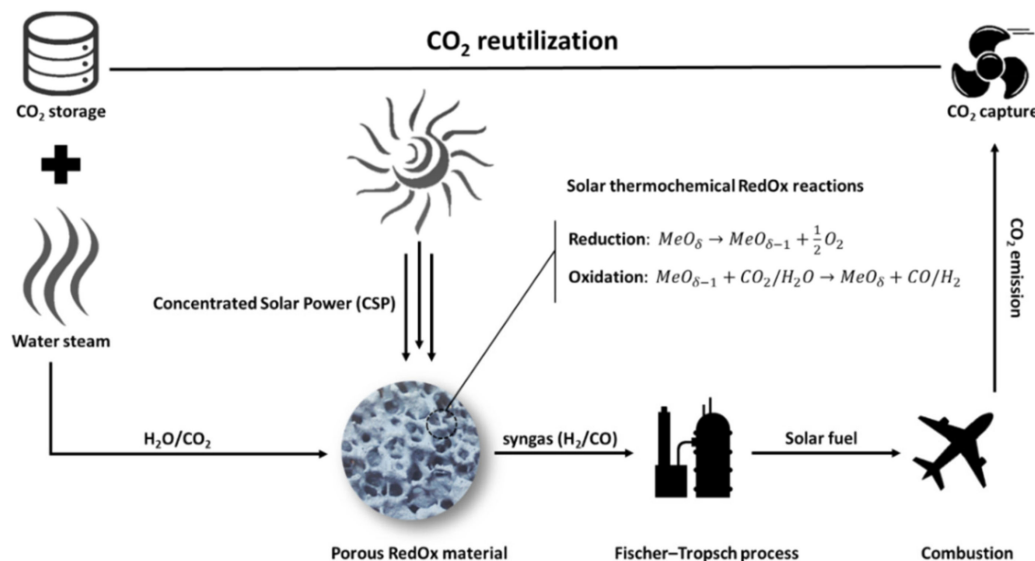


Figure 3. The CDR process via H₂O/CO₂-splitting solar thermochemical cycle as a route for solar fuels.

Reduction:



Oxidation:



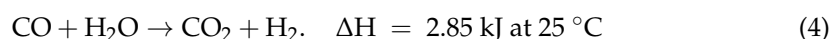
As per Le Chatelier's principle, lowering the partial pressure of O₂ within the metal oxide reduction reactor decreases the equilibrium reduction temperature and, hence, the associated parasitic losses [64]. This can be achieved through either the use of a vacuum pump [65] or a sweeping gas [64] diluting the O₂ concentration in the gas phase [66].

Similar to the production of CO from CO₂, the consecutive reduction and oxidation of the metal oxide can be also utilized for H₂ production. However, in this case, steam (H₂O) is used to oxidize the reduced metal oxide (Equation (3)).



The simultaneous production of CO and H₂ through Equations (2) and (3) will lead to the production of a gaseous mixture known as synthetic gas (or syngas in the abbreviated

form), which is potentially a feed for the production of hydrocarbon fuels [67]. H₂ can also be produced through water–gas shift reaction from CO (Equation (4)). The so produced fuels are called solar fuels enabling a closed loop of CO₂ as shown in Figure 3



Advantageously, the solar thermochemical CO and H₂ production using the metal oxide RedOx reactions enables adjusting the H₂:CO ratio to ~2:1 that is the optimal ratio for the methanol production via the Fischer–Tropsch process [68–70]. The measure of the conversion of solar heat into chemical energy for a given thermochemical process, $\eta_{\text{solar-to-fuel}}$, is defined as:

$$\eta_{\text{solar-to-fuel}} = \frac{-\Delta G}{Q_{\text{solar}}} \quad (5)$$

where ΔG is the maximum amount of the possible work by solar fuel products and Q_{solar} is the input solar heat into the reactor. Some techno-economic analyses on the commercialization of the thermochemical solar fuels synthesis processes agree on a minimum $\eta_{\text{solar-to-fuel}}$ of 20% to make the technology economically viable [71,72], while the maximum reported efficiency of the present state-of-the-art solar thermochemical technology is around 7.5% [73]. This indicates the need for the research on and development of the materials and reactor configurations, enabling significant development in the efficiency and, hence, competitiveness of the solar thermochemical technology.

In the following section, the effect of porous materials on the efficiency of the solar thermochemical processes is discussed. Firstly, various RedOx materials, capable of performing thermochemical RedOx reactions, are briefly explained. Then, the research works on porous RedOx materials are reviewed.

2.1. Reduction/Oxidation Materials

2.1.1. Classification of RedOx Pairs

Depending on the physical change of the oxygen carrier RedOx agent through the consecutive thermochemical RedOx reactions (Equations (1) to (3)), the metal oxide species can be classified into volatile and non-volatile groups. As a volatile oxide, the MO₈ undergoes gas–solid phase transition during the reduction step, while a non-volatile oxide remains in the solid phase through the complete RedOx reactions [19]. The higher oxygen exchange capability of the volatile cycles compared to nonvolatile ones enables higher oxygen release/uptake during the RedOx reactions and, hence, more fuel production per unit mass of oxide material [19]. In addition, the increased entropy due to the formation of gaseous products in volatile cycles makes the reduction reaction more thermodynamically favorable. However, the gaseous products of the reduction reaction in volatile RedOx materials (reduced MO₈, O₂ at high temperatures) need to be separated, diluted, or quickly quenched to prevent the MO₈ re-oxidation [74]. Nevertheless, these are technically challenging and add to the complexity of the process and, hence, costs [75]. It is worth mentioning that the physical phase change of the volatile oxygen carriers can lead to the regeneration of the structure of the active materials through each cycle, which can lead to the mitigation of the particle deactivation during some undesirable processes such as sintering and agglomeration [64]. This will lead to an improved material efficiency during RedOx reactions. On the contrary, the porous structure of the non-volatile materials can be altered through consecutive RedOx cycles and lead to their deactivation [64,76].

Steam and carbon dioxide are the main reacting feeding gases for the syngas production through the solar thermochemical process. The Gibbs free energy of formation of water ($\Delta G_f, \text{H}_2\text{O} = 56.7 \text{ kJ mol}^{-1}$) is slightly lower than that of the carbon dioxide ($\Delta G_f, \text{CO}_2 = 61.3 \text{ kJ mol}^{-1}$). Thus, water splitting can be thermodynamically more favorable than CO₂ and has been the focus of some research on the application of RedOx materials. However, the obtained results could be potentially generalized to CO₂ splitting as well as

due to the small difference in ΔG_f of both species. Therefore, in this part, the volatile and non-volatile RedOx materials for both CO₂ and H₂O splitting are briefly reviewed.

ZnO/Zn

The RedOx reactions of the ZnO/Zn pair for CO and H₂ production have been extensively investigated [23,77–81]. Nevertheless, the process requires high temperatures of ca. 1800 °C for the reduction of ZnO to Zn and O₂ [77], which can lead to significant parasitic re-radiation and convection heat losses from the reduction reactor [63,82,83]. Moreover, thermal dissociation of ZnO at high temperatures leads to the formation of a gaseous mixture of Zn(g) and O₂(g), due to relatively low melting and boiling points of Zn, i.e., 420 °C and 907 °C, respectively. However, this gaseous mixture is substantially explosive, leading to the recombination of Zn and O₂ to generate ZnO. Therefore, significant attempts have been made to efficiently separate the Zn(g) from O₂(g) [77,80]. Methods include diluting the mixture with an inert gas like argon or rapidly quenching it to temperatures of less than 420 °C, where Zn is solidified and, hence, separated [77]. A series of solar reactors have been also developed to perform the endothermic thermal dissociation of ZnO using concentrated solar radiation [77], such as the one shown schematically in Figure 4. In this directly irradiated solar cavity rotating reactor, which was developed at the Paul Scherrer Institute (PSI), a bed of ZnO particles is irradiated with highly concentrated solar radiation [79]. The cavity reactor is sealed from the environment using a quartz glass window such that the concentrated solar radiation is introduced into the reactor while the leakage of the gaseous products from the reactor or infiltration of the air into the reactor is avoided. Consecutive thermal dissociation of ZnO in temperatures of 1534–1634 °C has been demonstrated. Nevertheless, some Zn condensation has been also observed over the quartz window that can lead to a change in transmissivity of the window and significant technical challenges, e.g., breakage of the window due to the thermal stress [79]. The challenges become even more substantial if the window size is increased. The complete cycle of ZnO/Zn for CO₂ and H₂O splitting has been also demonstrated at bench scale but not at the pilot scale, mainly due to the above discussed limitations [23,78,84].

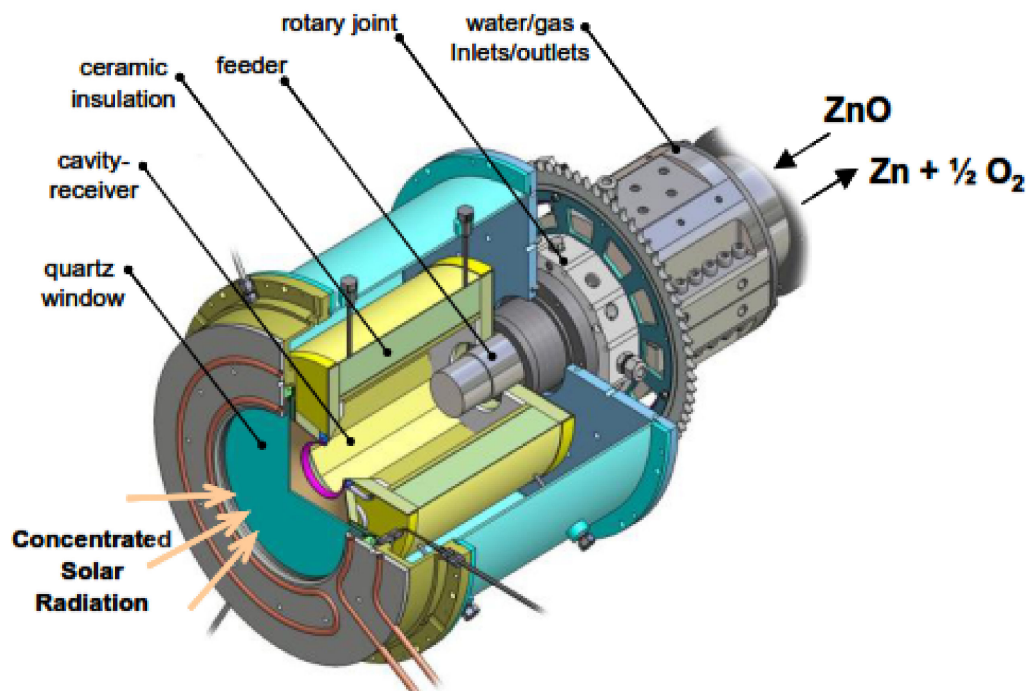


Figure 4. Schematic representation of the 10-kW directly irradiated solar reactor used for thermal decomposition of ZnO to Zn and O₂, developed at PSI [79].

SnO_2/SnO

The use of a SnO_2/SnO pair for the thermochemical water and CO_2 splitting has been investigated in several projects [85–88]. For example, at PROMES-CNRS (France), a solar-aided thermal reduction reactor, working at a temperature of $\sim 1600\text{ }^\circ\text{C}$, was employed for thermal dissociation of SnO_2 to SnO and metallic tin ($T_m\text{Sn} \sim 232\text{ }^\circ\text{C}$), followed by a hydrolysis reactor, in which H_2 is produced through oxidation of SnO/Sn with H_2O at $600\text{ }^\circ\text{C}$ [86]. The reactivity of SnO and Sn/SnO_2 nano-powders in reaction with CO_2 and H_2O has been also investigated using thermogravimetric analyzers (TGA) [88]. It was found that the SnO_2/SnO pair is more reactive to H_2O than to CO_2 in the range of $550\text{--}650\text{ }^\circ\text{C}$. Activation energies of $101 \pm 10\text{ kJ mol}^{-1}$ and $53 \pm 1\text{ kJ mol}^{-1}$ for the Sn/SnO_2 oxidation with CO_2 and H_2O were also measured, respectively. Similarly, the reactivity of SnO nanopowder in reaction with H_2O and CO_2 was investigated by Abanades [87] et al. They used a thermogravimetric analyzer system heated by concentrated solar radiation and found a high conversion rate of 88% for SnO with H_2O at a lower temperature (at $700\text{ }^\circ\text{C}$) than with CO_2 (at $800\text{ }^\circ\text{C}$).

2.1.2. Non-Volatile RedOx Pairs

The non-volatile pairs can be further classified as stoichiometric and non-stoichiometric materials, in which solid solutions are formed upon reduction due to the changes in the anion and/or cation vacancies, although they can still remain crystallographically stable [19]. A series of studied non-volatile RedOx pairs are reviewed here.

Iron-Oxide Based Cycle

These cycles typically exploit the oxygen storage capability of magnetite/wüstite ($\text{Fe}_3\text{O}_4/\text{FeO}$) pair (Equations (6) and (7)) and ferrites, in which a transition metal is substituted in the magnetite lattice e.g., $\text{M}_x\text{Fe}_{3-x}\text{O}_4$, $\text{M} = \text{Ni}, \text{Co}$.

Reduction



Oxidation with CO_2



Figure 5 shows the stability phase diagram of iron and oxygen [89]. As shown, hematite (Fe_2O_3) begins to reduce into magnetite (Fe_3O_4) and then wüstite (Fe_{1-x}O) at an oxygen pressure (P_{O_2}) of 10^{-6} mbar and $1207\text{ }^\circ\text{C}$, which is relatively close to the melting points of Fe_3O_4 and FeO that are $1597\text{ }^\circ\text{C}$ and $1377\text{ }^\circ\text{C}$, respectively (Figure 5) [68,90,91]. This can lead to sintering of the active materials during the RedOx cycles, if the reduction of Fe_2O_3 is performed at such high temperatures. Sintering of the active materials decreases their active surface area for the reactions and hence the reaction conversion efficiency [92–94]. As shown in Figure 5, lowering the partial pressure of oxygen can reduce the required reduction temperature; which, in addition to the mitigation of material sintering, can significantly decrease the challenges associated with the operation and construction of the high-temperature solar reactors (beyond $1500\text{ }^\circ\text{C}$) and the associated processes [68,90]. It is noteworthy to mention that the partial pressure of O_2 within the reduction reactor can be reduced via the application of a vacuum pump or a diluting gas, reducing the partial pressure of O_2 in the reactor [76,95]. Nevertheless, this can add to the complexity of the reactor design, heat recovery and the associated exergy losses. Thus, to increase the iron oxide reactivity, mechanical stability and mitigate the sintering effects, ferrites materials can be introduced as magnetite lattice doped with some transition metal ions e.g., Ni and Co ($\text{M}_x\text{Fe}_{3-x}\text{O}_4$, $\text{M} = \text{Ni}, \text{Co}$). In this regard, Allen et al. [96] found that cobalt ferrite (CoFe_2O_4) in 8 mol% yttria-stabilized zirconia (8YSZ) lowers the reduction temperature compared to the pure magnetite by at least $200\text{ }^\circ\text{C}$. Moreover, they found that this material possesses a relatively high stability through consecutive RedOx reactions, as such the

syngas product remained relatively constant over 50 consecutive RedOx cycles. The pore structure of the RedOx pair was then further developed via the decomposition of graphite as the pore former and the porous structure containing 10 wt% of CoFe₂O₄-YSZ found to have a higher thermal stability and also CO production per unit mass of the material than nonporous materials. In another work, Gokon et al. [97] used monoclinic ZrO₂ supported ferrites of Fe₃O₄ and NiFe₂O₄ powder particles (Fe₃O₄/m-ZrO₂ and NiFe₂O₄/m-ZrO₂). A hydrogen/oxygen ratio of 2 to 1 for both materials was reported with greater oxygen release rate for NiFe₂O₄ powder. Lastly, coating of NiFe₂O₄/m-ZrO₂ on the MPSZ and testing in a Xe-light reactor showed a successful repeatable production of H₂ with a ferrite conversion efficiency of 24–76% [97].

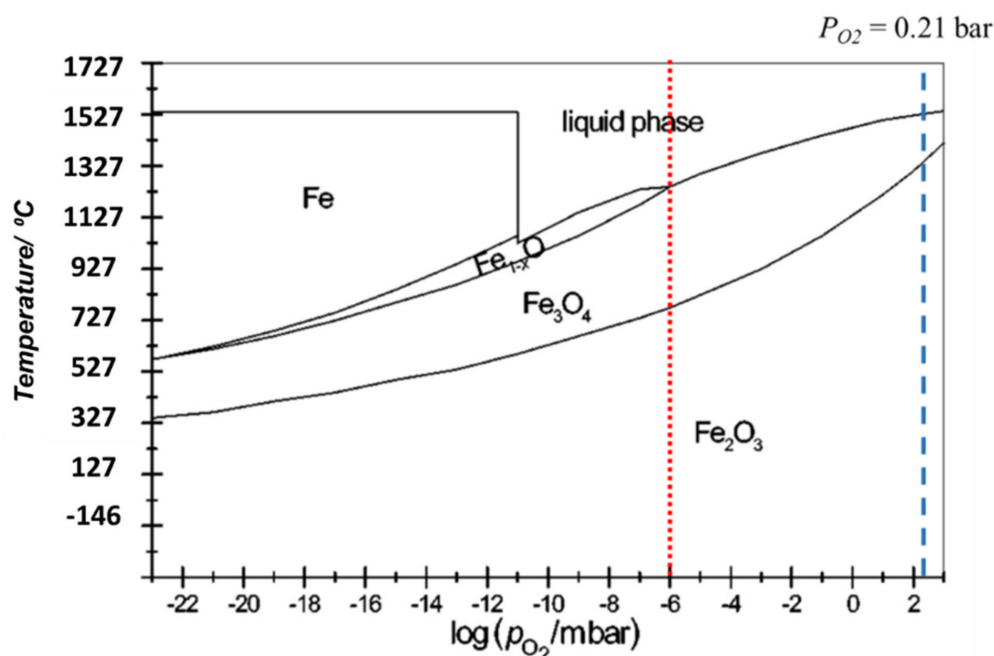


Figure 5. The stability phase diagram of iron and oxygen [89].

Doping of iron oxides for the improvement of their thermochemical properties was also investigated [98,99]. For instance, co-sintered iron oxides and YSZ were used in a TGA setup (TR: 1400 °C and CDS: 1100 °C) [98]. The results suggested that Fe in the form of a solid solution with YSZ (8 mol% Y₂O₃ in ZrO₂) is more reducible compared to bulk iron oxide. Furthermore, the co-sintering process helped the cyclability of the ferrites.

Hercynite

Another class of nonvolatile stoichiometric RedOx materials is aluminum spinel in the form of hercynite or $(A_x, B_{1-x})^{+2}Al_2^{+3}O_4$, in which 'A' and 'B' sites can be elements such as Ni, Co, Fe, Cu, etc. with +2 oxidation state [100–103]. For instance, atomic layer deposition of CoFe₂O₄ (with a 5-nm film thickness) on Al₂O₃ substrates showed a lower reduction temperature (TR: 1200 °C) than the coated form on ZrO₂ (TR: 1400 °C), which is due to the hercynite evolution as a result of reacting ferrite with the substrate [100]. In another study [101], water splitting was carried out with the O₂ and H₂ yields of 1.6 and 0.37%, respectively, by using Al-Cu ferrite. A recent study [102] was performed on the CO₂ conversion capability of NiFe₂O₄ on porous Alumina foams within a directly irradiated solar reactor heated by a high-flux solar simulator using CO₂ and CH₄ as the reactive gases. Results showed the formation of hercynite class materials (FeNiAlO₄ and FeAlO₄), because of high temperature reduction reaction, could result in a relatively higher thermal-to-chemical energy conversion efficiency. Similarly, a work on spinel aluminates revealed a tradeoff between the thermodynamics and kinetics of H₂ production reaction

with the positive effect of Co addition on CO₂ reduction kinetics (Co_{0.4}Fe_{0.6}Al₂O₄), while the highest fuel yield was reported for the composition without Co (FeAl₂O₄) [103].

CeO₂/Ce₂O₃

Substantial research focused on ceria (CeO₂/Ce₂O₃) as a nonvolatile non-stoichiometric cycle, for both CO₂ and water splitting [70,87,104–124]. This, in addition to the relatively high morphological stability of the CeO₂/Ce₂O₃ in consecutive RedOx cycles, is because of the high capability of ceria oxide in releasing oxygen through relatively fast reduction reactions [109]. However, despite the fast kinetics, cerium oxide (CeO₂) requires high temperatures even at low P_{O2} to reduce to Ce₂O₃, as shown in the stability phase diagram of Ce and O (Figure 6). This, in turn, leads to significant parasitic losses, e.g., radiative and convective from the reactor [82,125,126], which adds to the capital and operational costs of the process. It also limits the material compatibility, enabling significantly harsh operating conditions. On the other hand, ceria tends to sinter at high temperatures that strongly decrease its active surface and, thus, oxygen conductivity [127]. Therefore, significant effort has been allocated to the development of doped crystal structures of cerium oxide to reduce the required reduction temperature. For example, Call et al. [116] assessed zirconia-doped cerium oxide in the form of Ce_{1-x}Zr_xO₂ powder particles for a CO₂ splitting process using a thermogravimetric analyzer (TGA). Here 'x' is the stoichiometric amount of a doping element, i.e., Zr in this case. They found that an optimum value of x is in the range of 0.15 ≤ x ≤ 0.225 and can enhance the splitting process by up to 50% compared to the pure ceria. However, besides the improvements in the lowering of the reduction temperature and the needed partial pressure of O₂, P_{O2}, some deactivation of the active materials over 100 sequential RedOx reactions was also observed [116]. On the other hand, it has been found that increasing Zr content to x = 0.38 could lower the performance as low as pure ceria. Meng et al. [110] carried out some experiments on ceria doping in the form of Ce_{0.9}M_{0.1}O_{2-δ} ceramics with M = Mg, Ca, Sr, Sc, Y, Dy, Zr, and Hf followed by a comparison on their reactivity in H₂O splitting. They showed that the doping of cations with higher valences and a smaller ionic radius could efficiently enhance the O₂ released during the reduction step. It was concluded that the higher bulk ionic conductivity could enhance the amount of H₂ evolved through the oxidation step by improving the ratio of H₂ to O₂. Although they found Ce_{0.9}Hf_{0.1}O₂ with the highest reactivity, they suggested some doping of lower valence cations as well as for a better bulk ionic conductivity and, thus, an improved amount of evolved H₂. The RedOx pair of CeO₂/Ce₂O₃ was investigated at lab scale for hydrogen production with complete hydrolysis of Ce₂O₃ within 5 min with sublimation at temperatures greater than 2000 °C [106]. It was found that a higher activation energy for CO₂ dissociation is needed compared to that of H₂O dissociation when non-stoichiometric cerium oxide (CeO₂-CeO_{2-δ}) is employed [107]. Thereafter, doping ceria lattice by Y, La, Sm, Gd, Mn, Al, Fe, YSZ, Cu, Zn, Zr, and Co elements was assessed to improve the oxygen ion mobility [87,115,120]. Some noticeable improvements in the reducibility of ceria were reported for doping the structure with zirconia, with a linear increase in the range of 0–54%, while Y, La, Pr, and Gd were found to just affect the material stability during consecutive cycles [115].

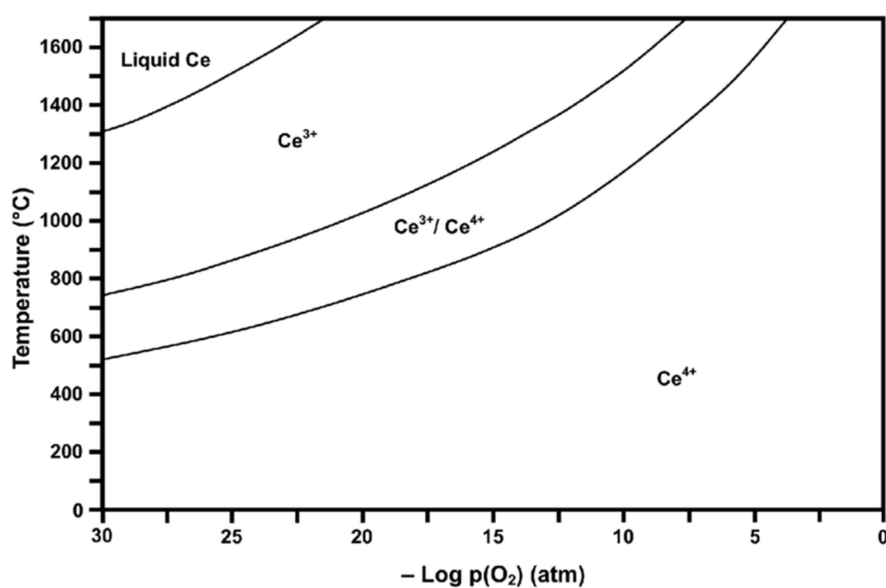


Figure 6. Ce-O stability phase diagram in different partial pressures of O₂ [127].

Perovskites

Perovskites, with a general form of ABO₃, have been traditionally used as bipolar plates in fuel cells. However, recently they have been also suggested as an oxygen carrier in thermochemical reactions [128–131]. The attempt for the use of perovskites in the thermochemical CO₂ splitting process returned back to 2013, when Scheffe et al. [130] used Lanthanum–Strontium–Manganese perovskites for splitting of H₂O and CO₂ using a TGA. In another work, disk-shaped pellets of La_{1-x}Sr_xMO₃ (M = Mn, Fe) were exploited for hydrogen production, through water splitting [130]. The maximum weight losses of 5.5 wt% for x = 1 in La_{1-x}Sr_xMnO₃ and 1.7 wt% for x = 0 in La_{1-x}Sr_xFeO₃ were observed. Lanthanum–strontium–manganese perovskites with Sr content of 0.3 and 0.4 wt% in the form of LSM30 and LSM40, respectively, were assessed at the Paul Scherrer Institute (PSI) facilities for both water and CO₂ splitting. In another work at Sandia National Laboratories (SNL), Sr- and Mn-doped lanthanum aluminate perovskites (La_{1-x}Sr_xMn_yAl_{1-y}O_{3-δ}) were considered for two-step solar-thermochemical CO₂ and water splitting cycles [129]. Interestingly, the mass of H₂ and CO produced per mass of the RedOx materials employed in this cycle, known as splitting capacity, increased by factors of nine and six, respectively, while, in addition to a higher stability, the required reduction temperature was decreased by ~300 °C compared to the pure ceria cycle. In another survey, Fe-doped CaTiO₃ was used as the RedOx active material and a similar performance to that of Ce/CeO₂ pair was observed [131]. In a recent study [132], Ba, Ca, or Y (A site) and Al, Mg (B site)-doped La_{1-x}Sr_xMnO_{3-δ} perovskite were used as active material for CO₂ splitting. High RedOx activities were observed for La_{0.6}Sr_{0.4}Mn_{0.83}Mg_{0.17}O_{3-δ} (LSMMg17). Decreasing of the reduction temperature was observed by doping Y³⁺ in the perovskite structure, while it could bring some difficulties in terms of the oxidation cycle [132]. Moreover, doping Mg²⁺ provides an enhanced solid–gas reaction kinetics, thermal stability, and resistance to sintering [132]. Bork et al. [133] tried to lower the operational temperature by using perovskite materials in the form of La_{0.6}Sr_{0.4}Cr_{1-x}Co_xO_{3-δ} using TGA followed by experiments in a fluidized bed reactor. They showed that the CO₂ conversion can be increased by ~25 times for cobalt doping at x = 0.2 compared to ceria within the temperature range of 800–1200 °C, which is ~300 °C lower than that of the ceria cycle. This implies a great potential for less heat loss from the process and, thus, higher efficiency per mass of the RedOx materials. The investigations on the perovskite materials typically showed improvement in the reduction part of the cycle via achieving a relatively lower reduction temperature, while the re-oxidation part of the cycle with CO₂ and H₂O still needs further development [130]. Therefore, a trade-off should be considered between lowering the reduction temperature

and re-oxidation capability of the perovskite materials in reaction with CO₂ and H₂O. Through an investigation of eight formulations of the lanthanum manganite perovskite group, Cooper et al. [134] showed that the Sr- and Ca-doped perovskites in the form of La_{0.6}Sr_{0.4}Mn_{0.6}Al_{0.4}O₃ and La_{0.6}Ca_{0.4}Mn_{0.6}Al_{0.4}O₃ can lead to a 5–13-fold enhancement in the reduction extent, i.e., higher oxygen release compared with the ceria cycle in the range of 1200–1400 °C. Thermodynamic analysis by Takacs et al. [135] discovered that the lanthanum manganite perovskites doped with Ca, Al, in the A and B sites, respectively (La_{0.6}Ca_{0.4}Mn_{0.6}Al_{0.4}O₃), had the highest mass specific oxygen release, 0.290 mol O₂ per mass of the metal oxide at T = 1500 °C and p_{O2} = 2.36 × 10⁻³ bar and 0.039 mol kg⁻¹ at T = 1300 °C and p_{O2} = 4.5066 × 10⁻² bar. This comparative study was carried out for the La_{0.6}A_{0.4}Mn_{1-y}Al_yO₃ (A = Ca, Sr and y = 0, 0.4) family and the results showed that, despite the reduction extents of the perovskites being higher compared to CeO₂, their re-oxidation with H₂O and CO₂ was thermodynamically less favorable. Consequently, a lower mass specific fuel productivity compared to CeO₂ under the conditions of relevance to the solar thermochemical cycles was obtained [135]. This was attributed mainly to the lower standard partial molar enthalpy ($\Delta\text{H}^\circ_{\text{O}}$) and partial molar entropy ($\Delta\text{S}^\circ_{\text{O}}$) of the perovskites relative to the cerium oxides.

2.2. Application of Porous Materials in Solar Thermochemical Conversion

Re-oxidation of the reduced RedOx materials during the thermochemical cycles is strongly dependent on the available solid surface area for the reactions. Thus, the use of porous materials, enabling a high surface-to-volume (S/V) ratio, is substantially advantageous in terms of reaction kinetics and mass transfer [14,15,17,18,73,97,112,114,118,119,136–139]. Different types of porous materials including reticulated porous ceramics (RPCs) [18,73,114,140], honeycombs [141,142], foams [14,97,137,138,143], and felts as well as 3D ordered macroporous materials have been utilized successfully in this regard. These materials were either applied entirely made of active RedOx agent or as a thin layer of RedOx coating over a stable structure. The pore size of the RPCs can be classified as micro (<2 nm), meso (2–50 nm), and macro (>50 nm) [144]. In the following sections, the application of porous materials in solar thermochemical CO₂ conversion is reviewed. In addition, a chronological list of works on solar thermochemical conversion processes are presented in Table 2. Since the oxide materials for carbon dioxide and water splitting can be used interchangeably in a similar series of reactions (Equations (2) and (3)), the application of porous materials in both CO₂ and water splitting are summarized here.

Table 2. List of research items on the application of porous materials for solar thermochemical conversion processes.

Year	Porous Support	RedOx Coating Material	Chemical Process	Performance	References
1989	Alumina honeycomb/foam	Rh	CO ₂ methane reforming	more efficiency for honeycomb structure compared to foams	[145,146]
2005	re-crystallized SiC honeycomb	Mn/Zn ferrites	water splitting	conversion efficiency ~80% and hydrogen yield >90% at low oxidation temperatures (800 °C)	[141,147]
2008	c-YSZ / MPSZ foam	Fe ₃ O ₄	water splitting	ferrite conversion of 20–27% for a 10.5 wt% Fe ₃ O ₄ -coated porous MPSZ	[137]
2009	MPSZ foam	m-ZrO ₂ supported NiFe ₂ O ₄ , Fe ₃ O ₄	water splitting	ferrite conversion of 24–76% for a 25 wt% NiFe ₂ O ₄ coating on porous MPSZ	[97]
2008 ¹	1:3 Co _{0.67} Fe _{2.33} O ₄ /YSZ, Al ₂ O ₃ and TiO ₂	-	water splitting	unfavorable side reactions of ferrite with the YSZ supports and, thus, weak performance of the porous RedOx material	[127,148]
2010	cerium oxide (CeO ₂) monolith	-	water splitting/carbon dioxide splitting	with $\eta_{\text{solar-to-fuel}} = 0.7\text{--}0.8\%$ and the possibility of improvement through upscaling and removing the heat losses' effects	[70]
2011	siliconized SiC monoliths	Fe/Zn mixed oxide	water splitting	conversion efficiency ~30% and RedOx materials' degradation due to zinc content volatilization and inhomogeneous temperature distribution	[149]
	MPSZ foam	zirconia supported Fe ₃ O ₄ or NiFe ₂ O ₄	water splitting	maximum ferrite conversion of 60% for NiFe ₂ O ₄ /m-ZrO ₂ /MPSZ foam device	[143]
2012 ²	75 vol% YSZ and 25 vol% Fe ₂ O ₃	-	carbon dioxide splitting	yttria addition led to the oxygen conductivity improvement and Iron oxide conversion (max: 58%) and the stability of the CO production in consecutive RedOx cycles. The increasing of co-extruded honeycomb substrates' surface area from ~2.6 to ~8.5 cm ² did not lead to a notable improvement in CO generation per unit volume	[142]
	porous ceria felt	-	water splitting/carbon dioxide splitting	ceria sublimation and deposition on reactor components were detected as the main technical challenges, which eventually were responsible for deterioration of the active material and, thus, reactor yield	[150]
	ceria RPC	-	carbon dioxide splitting	with mean $\eta_{\text{solar-to-fuel}} = 1.73\%$ and max $\eta_{\text{solar-to-fuel}} = 3.53\%$, a 17 times' improvement in the fuel yield per cycle compared to ceria felt in previous study	[114]
2013	3DOM ³ CeO ₂ , NOM 4 CeO ₂	-	carbon dioxide splitting	more structural stability and CO production rate (10-fold) of porous structures over non-porous ones in over 55 cycles	[151]

Table 2. Cont.

Year	Porous Support	RedOx Coating Material	Chemical Process	Performance	References
2014	ceria RPC with dual porosities	-	carbon dioxide splitting	a 10 times higher yield for samples with porous struts (44% porosity) compared to samples with non-porous solid struts. The mean $\eta_{\text{solar-to-fuel}}$ of 1.72% was also detected in a 3.8-kW solar cavity receiver	[118]
	MPSZ	NiFe ₂ O ₄ /m-ZrO ₂ and CeO ₂	water splitting	lower yields of NiFe ₂ O ₄ /m-ZrO ₂ /MPSZ compared to CeO ₂ /MPSZ as a result of some sintering effects	[138]
2015	SiC, Ni, Cu foams	ZrO ₂ -supported CeO ₂	methane reforming/water splitting	higher gas yields for the Ni and Cu foams than for SiC. The poor thermal conductivity of SiC foam was also responsible for CeO ₂ particle sintering and, thus, an overall efficiency decrement.	[112]
2017	porous ceria	-	carbon dioxide splitting	high degree of reactivity (even after 2000 cycles) was reported	[152]
2019	ceria RPC with dual porosities	-	carbon dioxide splitting	molar CO ₂ conversion of 83% and $\eta_{\text{solar-to-fuel}} = 5.25\%$	[139,153]
2019	Ceria RPC	-	water splitting/carbon dioxide splitting	max. $\eta_{\text{solar-to-fuel}} = 5.22\%$ while increasing methane flow rate and decreasing the reduction temperature will enhance the nonstoichiometry value and, thus, syngas yield	[154]
2020	SiC RPC with dual porosities	La _{0.6} Ca _{0.4} Mn _{0.6} Al _{0.4} O _{3±δ} (LCMA)	carbon dioxide splitting	CO ₂ conversion with [CO%] = 3.2. A coagulation of smaller pores because of reaction between LCMA coating and SiC substrate was reported. The smallest pore size of 75 ppi delivered the highest CO yield of ca. 0.07 mol g ⁻¹ LCMA and $\delta = 0.4$	[18,136]
	ceria RPC (with gradient porosities 10–60 ppi)	-	water splitting/carbon dioxide splitting	max. $\eta_{\text{solar-to-fuel}}$ of ~7.5% after 64 cycles was measured with a high stability of the porous RedOx structures	[73]
	ceria RPC	La _{0.5} Sr _{0.5} Mn _{0.9} Mg _{0.1} O ₃ (LSMMg)	water splitting/carbon dioxide splitting	max. $\eta_{\text{solar-to-fuel}} = 5.3$ and the perovskite coating had just a positive effect on the reduction extent, which hindered oxidant gas (H ₂ O or CO ₂) accessing the reactive ceria and can result in the poor re-oxidation compared to the pure, uncoated ceria RPC	[14]

¹. monolithic, honeycomb-type structures entirely made from RedOx materials' rods ². monolithic, honeycomb-type structures through polymer-based co-extrusion of ceramics ³. three-dimensionally macroporous ⁴. non-ordered macroporous.

The very first application of porous materials in solar thermochemical CO₂ utilization dates back to 1989 when the deposition of Rh on an alumina-based honeycomb or foam structures for CO₂ methane reforming was investigated [145,146]. In this study, the performance of the honeycomb structure (4-mm square holes, 0.5-mm wall thickness) proved to be more efficient than that of the 10-ppi (pores per inch) foam. Nevertheless, it was conducted to make a comprehensive conclusion, and more assessment is needed. In the HYDROSOL project in 2005, a monolithic honeycomb medium made from re-crystallized silicon carbide (reSiC) was used in the framework of a solar reactor (Figure 7) [141]. The porous materials were structurally similar to the automobile catalyst media and consisted of Mn/Zn ferrites coated on reSiC honeycombs. They were tested within a series of reduction (1300 °C) and oxidation (800 °C) reactions for water splitting. The reactor reached a conversion efficiency of ~ 80% and hydrogen yield of >90% at oxidation temperatures as low as 800 °C. The measured hydrogen evolved in these experiments was in a good agreement with the laboratory experiments with the oxides in the form of powders, showing that the RedOx materials coated on a porous substrate with mean $d_p = 6 \mu\text{m}$ maintained their reactivity [141,147]. The main advantage of the HYDROSOL reactor is that it has no moving parts or even particles. Moreover, it enables controlling the temperature and the reactor operation through adjusting the mass flux density in each reactor module, in response to the variations in the inlet solar heat flux. This is significantly important given the diurnal and annual variations of the solar insolation.



Figure 7. The HYDROSOL solar receiver-reactor used for water splitting showing the installment position and configuration of Mn/Zn-ferrite coated SiC honeycombs [141].

The next work in this field was published in 2008 when Gokon et al. [137] conducted an experimental study on the application of Fe₃O₄, as RedOx agent, coated on both cubic yttria-stabilized zirconia (Fe₃O₄/c-YSZ) and magnesia partially stabilized zirconia (MPSZ) to compare the potentials for water splitting and production of hydrogen. The aerial oxidation of the aqueous suspensions of Fe(II) hydroxide was used to coat Fe₃O₄ on zirconia doped

with 8 mol% Y_2O_3 as the active powder material. To coat MPSZ substrates, YSZ was loaded on the porous MPSZ to increase the surface area. The structure was then impregnated into the iron nitrate solution to be coated with Fe_3O_4 . Coating of Fe_3O_4 on a substrate mainly prevents the coagulation or sintering of particles. The thermal reduction and water splitting reactions were performed in two different reactors equipped with infrared furnaces. The results revealed a ferrite conversion of 20–27% for a 10.5 wt.% Fe_3O_4 -coated porous MPSZ after 32 consecutive cycles of hydrogen production (TR: 1400–1450 °C and WS: 1100 °C) and an irradiation period of 60 min during each RedOx cycle. However, it seems that performing thermochemical reactions in two separate reactors could lead to some uncertainty in the measurements, while the use of a single reactor for both RedOx reactions may enable a better control over the reactor atmosphere and the inlet/outlet gases and, hence, more accurate measurements. In their next work [97], monoclinic zirconia (m-ZrO_2)-supported NiFe_2O_4 and Fe_3O_4 powders were similarly tested in powder and coated on MPSZ foam for water splitting process. A ferrite conversion of 24–76% was obtained after 10 repeated cycles and an irradiation period of 30 min in each cycle. These demonstrated the competency of foam-like RedOx materials compared to powder materials and the significance of the surface area in reactions.

Due to the significance of the surface-to-volume (S/V) ratio, a substantial attempt was also allocated to the direct fabrication of the RedOx powders into monolithic structures through methods like robocasting and slurry processes [127,148]. For example, cast 3D lattice-structured monoliths were manufactured from 1: 3 $\text{Co}_{0.67}\text{Fe}_{2.33}\text{O}_4$: YSZ to enhance the vacancies within the structure and, thus, oxygen mass transfer within solids. Similarly, polymethylmethacrylate (PMMA) as pore former was added to the materials to increase porosity within rods. These porous networks were utilized in cyclic lab scale and on sun water splitting reactions within the temperature range of 1000–1400 °C. Although the structure's integrity was improved, the 1:3 $\text{Co}_{0.67}\text{Fe}_{2.33}\text{O}_4$:YSZ showed limited capability for the cyclic water splitting, due to unfavorable side reactions of ferrite with the YSZ supports [127].

Porous, monolithic ceria was used in a directly irradiated solar cavity receiver/reactor for H_2O and CO_2 splitting. The material demonstrated stable and rapid oxidation reactions for CO and H_2 production over 500 cycles with $\eta_{\text{solar-to-fuel}} = 0.7\text{--}0.8\%$, which was argued to be dependent on the system scale and design rather than materials' chemistry. That is because both the reaction rates and the efficiency of the reactor were found to be limited mainly by the thermal losses as a result of both convective and radiative heat losses [70].

In another work, two adjacent thermochemical reactors consisting of nine siliconized silicon carbide (SiSiC) monoliths ($146 \times 146 \text{ mm}^2$) coated with iron-zinc mixed oxide were employed as chambers within a 100-kW_{th} directly irradiated solar water splitting reactor with a reduction temperature of ~1200 °C, followed by water splitting at 800 °C [149]. The conversion of steam was reported to be ~30%, while slight degradation and deactivation of the RedOx material were also observed, which were due to both the volatilization of the zinc oxide content of the porous structure and inhomogeneous temperature distribution within the solar reactor. Nonetheless, this was a successful demonstration of the use of RedOx-coated porous absorbers at a pilot-scale solar receiver/reactor. Gokon et al. [143] utilized ferrite/zirconia foam spin-coated with zirconia-supported Fe_3O_4 or NiFe_2O_4 , i.e., $\text{Fe}_3\text{O}_4/\text{m-ZrO}_2$, $\text{Fe}_3\text{O}_4/\text{c-YSZ}$, $\text{NiFe}_2\text{O}_4/\text{m-ZrO}_2$, and $\text{NiFe}_2\text{O}_4/\text{c-YSZ}$ coated on MPSZ as RedOx materials. These materials were tested for the two-step water splitting in a directly irradiated solar reactor by means of a Xe lamp solar simulator with a power output of $4 \times 10^6 \text{ kW}_{\text{th}}$. The highest reactivity was observed from the $\text{NiFe}_2\text{O}_4/\text{m-ZrO}_2$ pair coated on MPSZ with a relatively constant hydrogen production rate and maximum ferrite conversion of 60% in 20 consecutive cycles [142]. Polymer-based coextrusion ceramic honeycombs of zirconia and iron oxide (Figure 8) were used for splitting of carbon dioxide. This synthesis method enables controlling the surface area of the honeycombs. Moreover, the addition of 3 mol.% and 8 mol.% of yttria improved the oxygen conductivity of the materials, leading to a noticeable increase in both iron oxide conversion from 41% to 58%

and the stability of the CO production in consecutive RedOx cycles. Additionally, the results showed that the CO generation significantly depended on the reaction temperature and CO₂ flow rate. Interestingly, the increasing of substrates' surface area from ~2.6 to ~8.5 cm² did not lead to a significant improvement in CO generation per unit volume of the extruded honeycomb structure, as it did not significantly differ in terms of pore size. The reaction mechanism was also found to be initially spontaneous over the surface of the RedOx materials, while, over time, the diffusion mass transfer through pore structure became dominant and the reaction rate controlling, which can be attributed to the enhanced transport phenomena [142].

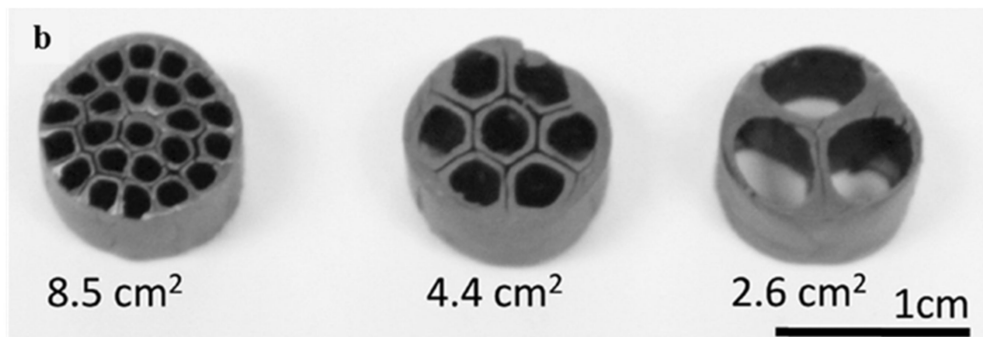


Figure 8. Polymer-based coextrusion ceramic honeycombs made from homogeneous composites of iron oxide and zirconia for the solar thermochemical dissociation of CO₂ to CO [142].

Furler et al. [150] examined porous ceria felt for thermochemical CO₂ and water splitting in a solar directly irradiated cavity-receiver, exposed to a mean solar concentration ratio of 2865 suns (TR: 1527 °C and WS/CDS: 827 °C). The dependence of the composition of the product syngas on the composition of the feeding mixture of CO₂ and H₂O in a range of 0.8 to 7.7 was investigated. Advantageously, it has been found that the composition of the product syngas can be optimized enabling a H₂ to CO ratio of ~2, which is needed in Fischer-Tropsch processes, through varying the feeding ratio of the H₂O to CO₂ for the oxidation of the porous ceria felt. Nevertheless, ceria sublimation and deposition on other reactor components, in particular irradiation widow, were found as the main technical challenges, which can lead to thermal stress and crack in the reactor structure. Sublimation of the ceria also leads to the loss of active materials and reduction of the oxygen transfer capacity and hence reactor yield over consecutive RedOx cycles. This directly irradiated solar reactor was further scaled up to accommodate four RPC rings, entirely made from ceria as depicted in Figure 9a [114]. A mean solar to fuel energy conversion efficiency of 1.73% together with a maximum spontaneous efficiency of 3.53% was reported for CO₂ splitting. They also observed oxygen deficiency (δ), ranging from 0.016 to 0.04 for the temperatures of 1400 to 1600 °C. Also, the use of porous RedOx material in this setup (Figure 9b) was compared with the optically thick ceria felt used in their previous study [150] and confirmed a 17 times improvement in the fuel yield per cycle.

Three-dimensionally macro-porous (3DOM) CeO₂ and non-ordered macroporous (NOM) CeO₂ were also used for CO₂ splitting [151]. These structures were synthesized using polymeric colloidal spheres as templates and tested in an infrared furnace (TR: 1200 °C, CDS: 850 °C). The results in this case confirmed the advantages of using porous over non-porous structures, as the structure of the porous RedOx materials was almost stable in over 55 cycles, leading to a considerable improvement in the CO production rate (10-fold enhancement) relative to that of the nonporous CeO₂ structure. This was attributed to the differences in reactivity of materials because of differences in their surface accessibility by the oxidative gas through the oxidation cycle. This research revealed the importance of pore engineering of porous materials through pore templating that could potentially improve the interconnectivity of the three-dimensional pore structure and mass

transfer, especially through the oxidation stage, and, thus, the kinetics of the oxidation step besides improving the resistivity toward sintering.

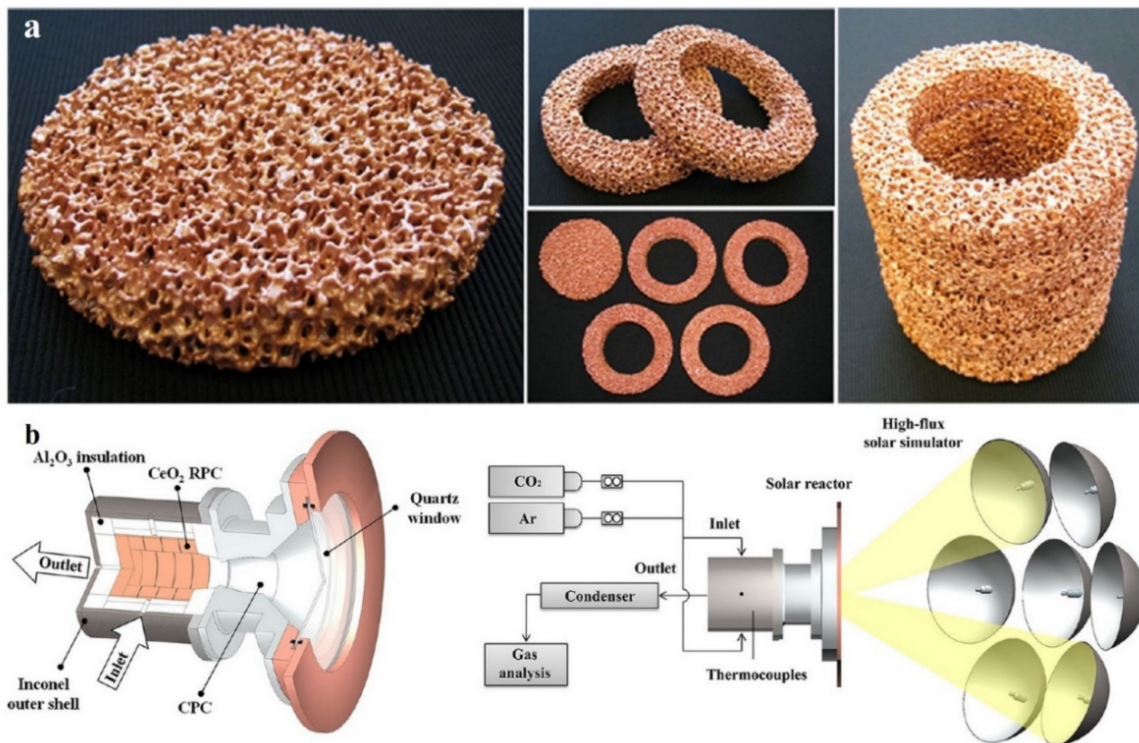


Figure 9. (a) Ceria-coated RPCs consisting of a 20-mm thickness, 100-mm o.d. disk, and four 20-mm thicknesses, 60-mm i.d., 100-mm o.d. rings; (b) High-Flux Solar Simulator and the configuration of porous modules' assembly at the Swiss Federal Institute of Technology (ETH) (bottom) [114].

The novel configuration of ceria RPCs with dual scale porosity, i.e., larger macropores, between struts and smaller μm -sized pores inside struts, was also examined [118]. In doing so, some ceria foams were manufactured with pore sizes in the millimeter range ($d_{\text{mean}} = 2.5 \text{ mm}$ and $\epsilon = 0.76\text{--}0.82$) macroscopically through the bulk and micrometer order ($d_{\text{mean}} = 10 \mu\text{m}$ and $\epsilon_{\text{strut}} = 0\text{--}0.44$) inside the struts by using some sacrificial carbon-based pore-forming agent with particle sizes of $0.4\text{--}12 \mu\text{m}$. The synthesized dual-scale ceria foam is shown in Figure 10. Thermogravimetric experiments (TR: 1500°C and CDS: $600\text{--}1000^\circ\text{C}$) revealed a 10 times' higher yield for the samples with porous struts (porosity: 0.44) compared to samples with non-porous solid struts. It was hypothesized that the millimeter pores could enhance the reduction reaction, providing an improved penetration of thermal irradiation into depth and, thus, a uniform heating, while the micrometer pores could help the oxidation kinetics by providing a better surface area for such a surface-limited process and decreasing the oxidation time to about one-ninth. Indeed, there was trade-off between the specific mass of active RedOx material per unit volume and porosity. While a higher specific mass led to a higher conversion, due to the availability of more active materials, a low porosity resulted in less radiation penetration and, hence, reduction extent. Finally, for a validation of TGA results, the dual-scale RPC was used in a solar cavity-receiver (3.8-kW radiative power at 3015 suns) and showed a mean $\eta_{\text{solar-to-fuel}}$ of 1.72% [139]. MPSZ foams coated with ferrite supported on monoclinic zirconia ($\text{NiFe}_2\text{O}_4/\text{m-ZrO}_2/\text{MPSZ}$) and cerium oxide (CeO_2/MPSZ) were also tested in a directly irradiated receiver/reactor equipped with a Xe solar simulator for water splitting [138]. Results showed that the $\text{NiFe}_2\text{O}_4/\text{m-ZrO}_2/\text{MPSZ}$ RedOx material had lower yields than CeO_2/MPSZ as a result of some sintering effects at reduction temperatures of TR = 1450 and 1550°C . The effects of the porous substrates' materials on the methane

reforming for syngas production and water splitting was also investigated [112]. SiC, Ni, and Cu foams coated with zirconia-supported cerium oxide were heated to 900 °C using a solar simulator. Results revealed higher gas yields for the Ni and Cu foams than for the SiC one. This was related to the catalytic nature of Ni and Cu for the methane reforming reactions and the better radial thermal distribution within these metals. Indeed, the poor thermal conductivity of the SiC foam substrate compared to the metallic ones resulted in CeO₂ particle sintering in consecutive cycles and, thus, a decrement on the overall efficiency.

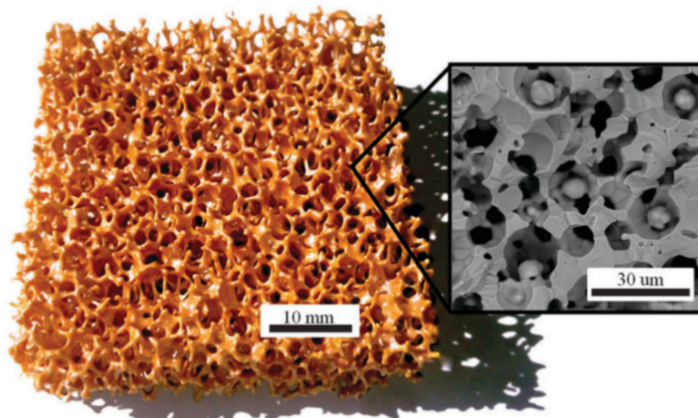


Figure 10. Ceria RPC with dual-scale porosities; macro-porous structure with mm-sized pores that are ideal for reduction and μm -sized pores inside struts (SEM micrograph) responsible for oxidation reaction in the carbon dioxide splitting process [118].

The cerium oxide as a RedOx material was examined in various works. For example, the powder and porous forms of the cerium (IV) oxide was tested for CO₂ splitting in a thermogravimetric analyzer (TGA) setup (TR: 1450 °C and CDS: 1100 °C) [152]. The results showed a mean value (after 2000 cycles) of $\delta = 0.0197$ in CeO₂ → CeO_{2-δ} cycle with a maximum value of $\delta = 0.0383$ at 1450 °C. Higher degrees of non-stoichiometry (δ) led to more oxygen storage/loss and mobility, while also maintaining the crystallographic fluorite structure of ceria, leading to more fuel production yield. The porous samples were reported to slightly lose some of their surface area. However, the porous structure maintained its reactivity even after 2000 cycles, which is a prerequisite if the RedOx cycle based on the cerium oxide is going to be commercialized.

Some efforts on the bench scale as a prerequisite for large-scale demonstration and commercialization of the RedOx materials have been also reported [139,153]. For example, in a recent attempt, a 4-kW solar reactor featuring a ceria RPC with dual porosities as shown in Figure 11a was developed and utilized for CO₂ splitting [139]. The thermal reduction was carried out at $T_{\text{reduction}} = 1450\text{--}1500$ °C and vacuum pressures ($p_{\text{total}} = 10\text{--}1000$ mbar) by means of a solar simulator with a power of 2.4–4.1 kW. By turning off the solar simulator and cooling down into $T_{\text{oxidation}} = 700\text{--}1000$ °C, the oxidation reaction occurred at CO₂ flow rates of 3–7 L min⁻¹ completing a 15-min RedOx cycle. Through a temperature/pressure-swing operation within a reactor depicted in Figure 11b, separate streams of O₂ and CO with almost 100% selectivity were produced. Also, a molar CO₂ conversion to CO of 83% together with $\eta_{\text{solar-to-fuel}} = 5.25\%$ were obtained, which is around three times more than the previously reported values i.e., 1.73% on average and 3.53% at peak [118].

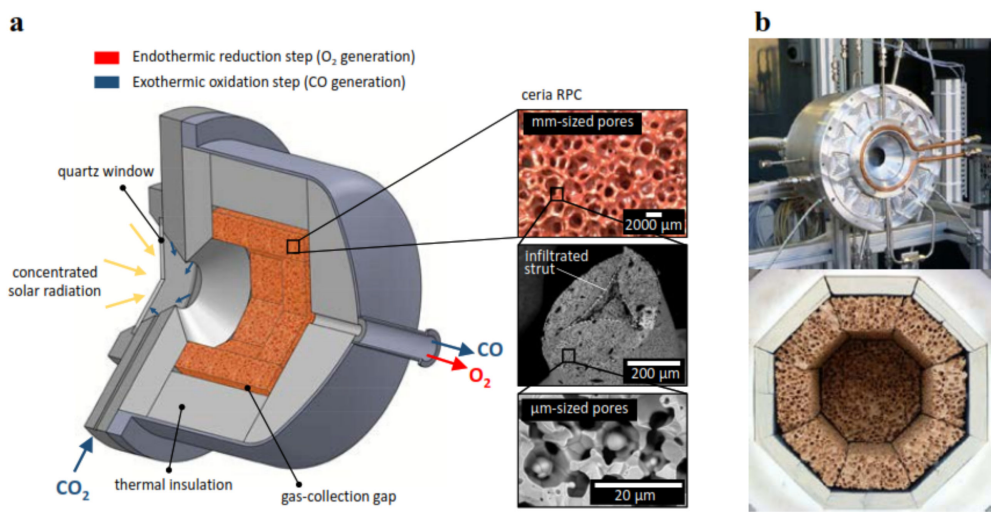


Figure 11. (a) Schematic representation of the solar reactor for carbon dioxide splitting, comprising a windowed cavity-receiver containing a ceria RPC with dual pore sizes (mm- and μm -sized pores); (b) images of the front face of the solar reactor with the windowed aperture and its interior containing the octagonal ceria RPC structure insulated with a line of alumina [153].

A volumetric, directly irradiated solar cavity receiver equipped with 5-ppi ceria RPC was directly irradiated in the temperature range of 950–1050 °C for syngas production and isothermal $\text{H}_2\text{O}/\text{CO}_2$ splitting [154]. The ceria reduction was performed with methane (partial oxidation of methane), while the oxidation was completed by $\text{H}_2\text{O}/\text{CO}_2$ under the same operating temperature. Methane was employed to reduce the reduction temperature and, hence, the technical challenges associated with the high temperatures and the parasitic losses. Various operating parameters such as methane flow rate and reduction temperature were studied on the CO_2 conversion and, thus, syngas yield. It was shown that an increase in the methane flow rate and decrease in temperature resulted in carbon formation during methane cracking, while increasing the nonstoichiometry value (δ up to 0.38) led to greater syngas yields, with a maximum value of 8.08 mol of methane per kg of CeO_2 . The material stability was reported to be high enough after 15 successive ceria RedOx cycles with the highest solar-to-fuel energy conversion efficiency of 5.22% and the energy upgrade factor in the range of 0.97–1.10. Nonetheless, further cyclic RedOx assessments are needed to justify the material stability.

Despite the significant effort that has been allocated to the development of various RedOx pairs, the cerium oxide and perovskite materials have been relatively more attractive. This is due to their potential for higher efficiency and durability over successive RedOx cycles. In a recent, unprecedented work, a nano perovskite-coated silicon carbide RPC with dual pore sizes of macro pores between struts ($d_p = 2.54 \text{ mm}$) and μm -sized pores inside struts ($d_p = 490 \mu\text{m}$) was tested in an infrared furnace to assess the capability of the developed materials for CO_2 splitting [18]. The porous structure was coated by the dip-coating method [155] with ca. 15-mm thickness of $\text{La}_{0.6}\text{Ca}_{0.4}\text{Mn}_{0.6}\text{Al}_{0.4}\text{O}_{3\pm\delta}$ (LCMA) as active RedOx material. The LCMA-coated porous substrate could convert CO_2 to CO with a concentration of $[\text{CO}\%] = 3.2$ in a controlled atmosphere of 10 vol.% CO_2 feed gas at 1050 °C after around 1.5 h of reduction reaction at 1240 °C. However, the XCT characterization revealed that the process distorted the RPC by coagulation of smaller pores within struts and some diffusion of LCMA into struts' pores. As a complementary work [136], three different pore sizes of porous substrates, i.e., 5, 12, and 75 ppi, were also investigated to assess the effects of pore architecture on CO_2 conversion efficiency. Figure 12 illustrates the 2D tomograms of 12 ppi sample (a) before; (b) after LCMA perovskite coating; (c) after tomograms registration showing the perovskite coating layer. Although the sample with pore size of 12 ppi possessed the most homogeneity of RedOx coating layer as much as the highest perovskite loading, 75 ppi porous sample with the smallest pore sizes delivered

the highest CO yield of ca. 0.07 mol g^{-1} LCMA. The non-stoichiometry oxygen was also calculated to be $\delta = 0.4$.

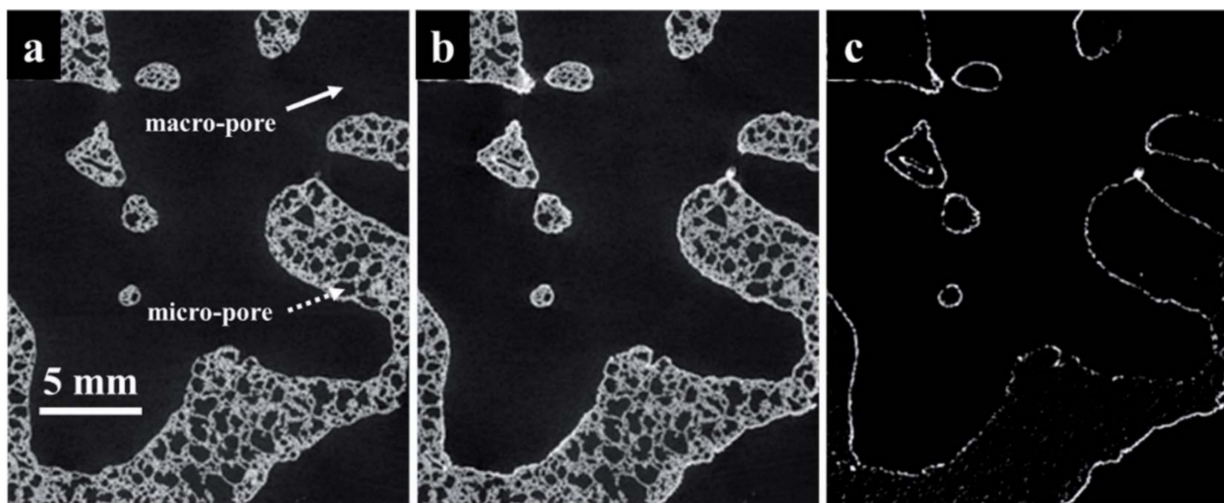


Figure 12. The 2D tomogram slices of a porous SiC sample with dual-scale pore sizes including macro pores between struts and μm -sized micropores inside struts; (a) before; (b) after LCMA perovskite coating; and (c) after tomograms' registration showing the perovskite mapping [136].

Haeussler et al. [73] tested a series of ceria RPCs with gradient pore sizes in the range of 10–60 ppi within a $1.5 \text{ kW}_{\text{th}}$ directly irradiated solar reactor. The temperature-swing RedOx reactions were performed (TR: $1400\text{--}1450^\circ\text{C}$ and WS/CDS at $700\text{--}1100^\circ\text{C}$) to produce pure H_2 or CO inside the same reactor (Figure 13). Similarly, the results demonstrated that the degree of ceria reduction increases with decreasing of both the temperature and the operating pressure. Moreover, it was found that the oxidation rate could be improved (up to $9.3 \text{ mL g}^{-1} \text{ min}^{-1}$) by increasing the inlet CO_2 flow rate which is attributed to the increasing of the reactions driving force. A maximum $\eta_{\text{solar-to-fuel}}$ of $\sim 7.5\%$ was also measured after 64 cycles with a high stability of the porous RedOx structures [73].

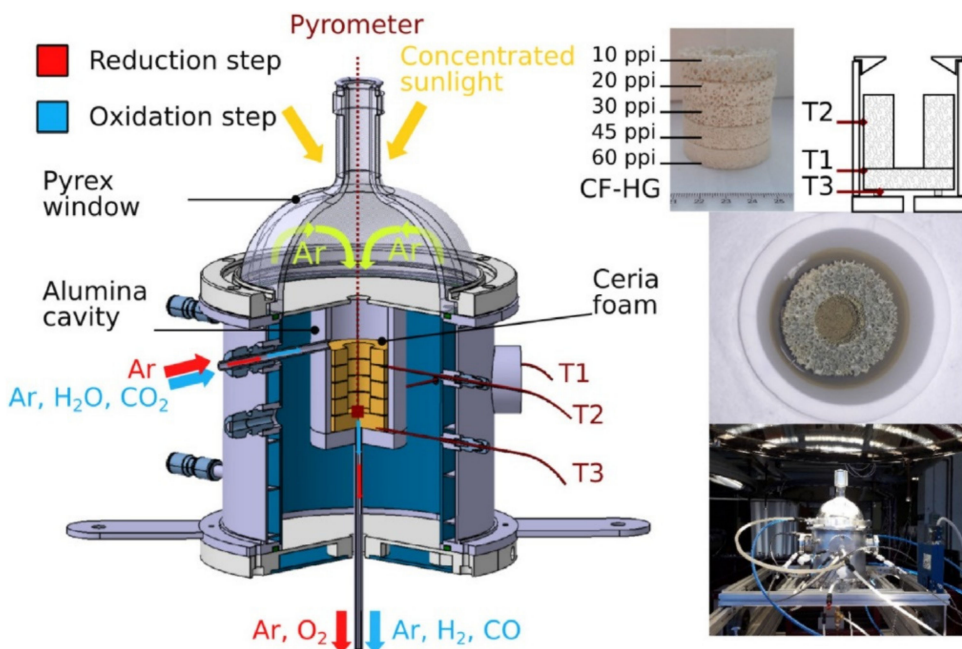


Figure 13. Schematic of the $1.5 \text{ kW}_{\text{th}}$ directly irradiated solar reactor equipped with a series of ceria RPCs with 10–60-ppi gradient pore sizes used for H_2O or CO_2 splitting [73].

Subsequent to the previous work, the $\text{La}_{0.5}\text{Sr}_{0.5}\text{Mn}_{0.9}\text{Mg}_{0.1}\text{O}_3$ (LSMMg)-coated ceria foam was tested for steam and carbon dioxide splitting [14]. The results showed an improved reduction extent mainly due to the perovskite layer, but no improvement was observed in the re-oxidation and the fuel production rate compared to the pure uncoated ceria RPC. It was concluded that the use of LSMMg perovskite coating ($\sim 10\text{-}\mu\text{m}$ thickness) worked as a layer that hindered the oxidant gas (H_2O or CO_2) from accessing the reactive ceria, which possessed a higher re-oxidation capability. However, it was shown that by optimization of some reaction parameters such as pressure during the reduction cycle and the total gas flow rate as well as the oxidant molar fraction during the re-oxidation step the fuel production rate could be increased. This research on porous RedOx materials with coupled positive aspects of two different active materials showed a maximum $\eta_{\text{solar-to-fuel}} = 5.3$, which was very close to the value for the uncoated ceria foam (peak $\eta_{\text{solar-to-fuel}} = 5.5$). The role of this composite synthesis was synergistic oxygen release in the reduction cycle and resulted in a higher total fuel production relative to the uncoated ceria.

The majority of the proposed and assessed reactors for the thermochemical CO_2 and H_2O splitting was based on the direct irradiation of the porous oxygen carriers in a cavity receiver/reactor [69]. This is mainly because the cavity shape has been found as the most suitable configuration for efficient harnessing of highly concentrated solar radiation [156], due to its potential for the mitigation of the re-radiation and convection heat losses [82,125,126,157]. However, recently, an indirectly heated reactor concept for the two-step partial RedOx cycles was proposed by Yuan et al. [158], which is heated indirectly by a molten metal heat transfer fluid (MLHTF). In this system, the MLHTF is first heated within a solar cavity receiver and then is transferred and used to feed the solar energy captured in the receiver to the reactor. The reactor comprises an array of sealed reaction chambers that are interconnected with a piping network, which allows the LMHTF to transfer heat between the chambers. The liquid metal also facilitates efficient heat both within the solar receiver and the reaction chambers [159]. The overall thermal-to-chemical efficiency of this system (from the thermal energy in the liquid metal to the chemical energy in the hydrogen fuel) is estimated to be $\sim 20\%$ when ceria is employed as the reactive oxygen storage material [158]. The estimated efficiency of this system is an order of magnitude higher than that of previous designs based on direct irradiation of the reduction reactor. Additionally, it offers potential both to integrate solar thermal energy storage into the system, i.e., via a series of tanks [7,64], and to mitigate the power density mismatch between the demand of the reduction reactor and the concentrated solar radiation [158]. However, this technology is at the embryonic stage of development and faces significant challenges in regard to material compatibility, handling, containment, and transfer of molten metals through various components of the system [160,161] and needs significant further assessments and developments.

2.3. Potentials and Critical Research Challenges

From a fundamental point of view, using sunlight as a source of thermal energy provides advantages over photocatalytic approaches. This is because it enables the use of the entire solar spectrum, as opposed to only using the high energy portion of the spectrum with energy greater than the photocatalyst bandgap [158]. Techno-economic analyses have also shown that the production of solar fuels through thermochemical methods can be economically viable, if the solar-to-fuel efficiency of a system exceeds 20% [71,72]. Notwithstanding the potential advantages of the use of solar thermal energy for thermochemical CO_2 and H_2O splitting, this technology is still at a relatively early stage of development with all demonstrations being at bench scale. Therefore, further research, development, and pilot-scale demonstrations are required if the technology is to be implemented in large scale. In particular:

1. RedOx material improvements are necessary to reduce both the required temperature of the RedOx reactions preferably to less than $1000\text{ }^\circ\text{C}$, and the degradation of the

materials over a very large number of cycles. This is especially important for the reduction of the oxygen carriers used in the RedOx cycles (Equation (1)), because:

- a. The heat loss from the solar systems increases significantly with temperature [82,125,126,157]. The re-radiation heat losses from the cavity solar receiver and reactors increases with the fourth power of the reactor absolute temperature [7,63,75,162], while the challenges associated with the start-up and shut-down of the solar receiver and reactors and the associated parasitic losses also increase with the temperature [63].
- b. Material compatibility is a substantial challenge of the state-of-the-art reactors, which can be greatly reduced through lowering the operating temperature of the system. Commensurate with this, operating temperatures of less than ~1000 °C would enable the use of commercially available stainless steels with a lower cost of insulation and, hence, bring down the capital costs [68].
- c. To achieve temperatures of more than 1000 °C within the solar receiver and reactors there is need for high concentration ratios from the heliostat field, which, in turn, increase the spillage losses and capital costs of the solar concentrators.

Porous structures have been shown to assist in the increasing oxidative capacity and durability and, hence, are likely to be a key part in the commercial implementation of thermochemical cycles for CDR.

2. Along with the progress in material synthesis and design, improvement in the performance of the reactors is needed to efficiently utilize the solar heat to drive the endothermic reduction reactions.
 - i. The majority of the proposed and assessed RedOx cycles are based on the directly irradiated solar reactors [83,163–165], employing a quartz glass window [68]. Windows are often used in laboratory-based reactors [68]. In commercial application there are potential issues with the high cost of large quartz windows and the need to maintain/clean them in the field [68]. That is because the windows are vulnerable to particle deposition, thermal shock, and high/low pressures, while also they need effective sealing [166–168]. To avoid directly irradiated, windowed solar reactors, an approach is to use highly concentrated solar radiation to heat a heat transfer fluid (HTF), which is transported into an indirectly heated reduction reactor and used to provide the required heat of the endothermic reactions [158,159]. Nevertheless, the concept has recently begun to be explored such that the full extent of its potentials and challenges are yet to be identified. It is worth noting that potentially a relatively higher thermodynamic efficiency can be achieved in directly irradiated solar receiver/reactors relative to indirectly heated ones, due to the elimination of the exergy losses associated with the heating of the intermediate HTF and the temperature difference needed within the required heat exchangers to efficiently transfer heat from HTF to reactors and other components of the process [64]. It is also worth mentioning that a high-temperature pump has been recently developed and demonstrated to circulate molten tin at 1200–1400 °C in such a system [169]. Another potential approach is to use a windowless reactor [170]. This avoids the issues of using a window [64], although this would be achieved at the expense of a lower efficiency. The concept of windowless reactors has been recently explored at bench scale by Long et al. [170]. They characterized the isothermal flow-field within a vortex-based solar cavity receiver with an open aperture. However, further demonstration and assessments are needed to better understand the performance of these receiver/reactors under more realistic conditions, e.g., on solar towers, where they are well above the ground wind boundary layers and exposed to substantial turbulence from relatively permanent wind in different directions [82].

Finally, further research in whole cycle configurations is needed to identify process configurations that enable minimum exergy loss through efficient heat recovery.

3. Photoreduction of CO₂

Photocatalytic conversion of CO₂ into hydrocarbons offers the potential for low-cost and sustainable amelioration of energy shortages and CO₂ emissions [21]. Nevertheless, despite significant improvement in the efficiency of the photoreduction process since the first report in 1979 [171], it is still far from being economically viable [172]. Therefore, widespread attention has been allocated to this technology. In this method, as shown in Figure 14, the photocatalyst is excited via absorption of photons with energy higher or equal to the energy of a gap between the valence band (VB) and conduction band (CB). The irradiated energy excites an electron from the VB to the CB, creating a deficit of negative charge in the VB (referred to as a “hole”), and acts as a positive charge carrier. Then, the electrons act as a reducing agent for the adsorbed CO₂ molecules on the surface of the photocatalyst, and the holes drive a charge-balancing oxidation reaction. Finally, the produced molecule has to desorb and diffuse to the gas or liquid phase to accomplish the conversion process [24,173,174].

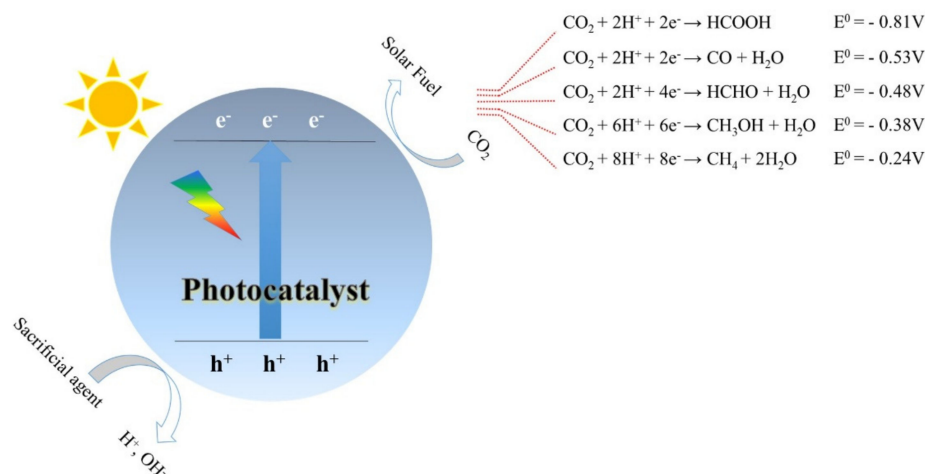


Figure 14. Schematic of the overall photocatalytic reaction process for CO₂ reduction (E° Potential (V) vs. NHE at pH 7).

Among the various known photocatalysts, TiO₂ has been found as the most promising material due to its availability, high chemical stability, and low cost [25,175]. Furthermore, the use of metal-organic frameworks (MOFs) as a new class of organic-inorganic hybrid materials with an extended 3D network has recently drawn widespread attention, which is mainly due to their unique properties such as structural flexibility, tunable and well-ordered porous structures, and high specific surface area. TiO₂ and MOFs along with their modification methods will be the focus of this section.

3.1. TiO₂ Photoreduction Catalyst

The use of TiO₂ for CDR offers significant advantages such as high photoactivity, high physical and chemical stability, non-toxicity, low cost, and widespread availability [176–178]. Notwithstanding these significant advantages, TiO₂ has also the drawback of its wide band gap (3.2 eV), which limits its activation only to the UV region, which accounts for only 5% of solar insolation [26,179–181]. In addition, TiO₂ shows relatively low CO₂ reduction efficiency and selectivity due to the fast electron-hole recombination and the competing side reaction of the hydrogen evolution reaction (HER, 2H⁺ + 2e⁻ → H₂) [182,183]. Thus, extensive works have been performed to enhance TiO₂-based photocatalyst performance. These include doping with metals and non-metals, surface sensitization, and

coupling with other semiconductors to enhance visible light absorption and reduction efficiency [27]. In the following sections, these are discussed in more detail.

3.1.1. Metals' and Non-Metals' Doping and Cocatalysts

Doping with metals or non-metals is a method that is extensively applied to increase the spectral response of TiO₂-based nanocomposites. In this method, the excitation of the electrons from the valence band (VB) to the conduction band (CB) is facilitated by reducing the absorption edge of TiO₂ [184,185]. Additionally, doping TiO₂ with metals reduces the electron-hole recombination by trapping photo-generated charge carriers [186]. A list of research items on the doping of TiO₂ with metal and non-metals is presented in Table 5. Indium (In) is an efficacious metal to increase TiO₂ photoactivity and selectivity, since In-metal can produce large number of electrons and reduce recombination of photogenerated charges over TiO₂. Besides, In-metal has other particular characteristics, e.g., it is relatively cheaper and has multiple oxidation states and low toxicity [187,188]. Therefore, In-doped TiO₂ nanoparticles were synthesized for CO₂ photoreduction with H₂O vapor under UV light irradiation in a cell-type photoreactor. The reaction was performed at 373 K and 0.2 bar with a CO₂-to-H₂O feed ratio (P_{CO₂}/P_{H₂O}) of 1.43. The presence of the indium over TiO₂ produced the anatase phase of mesoporous TiO₂ with smaller particle size and larger surface area. As shown in Table 5, CO and CH₄ were the main products. The maximum yield rates for CH₄ and CO were obtained over 10 wt.% In-doped TiO₂ of 244 and 81 μmol, which are 7.87 and 1.76 times greater than that pure TiO₂, respectively. On the other hand, the selectivity of CH₄ was increased from 40% over TiO₂ to 70% over In-doped TiO₂. As a result, the In-doped TiO₂ catalyst showed better catalytic performance compared to the pure TiO₂ due to the higher active surface area, efficient production, and suppressing recombination of photogenerated electron-hole pairs. [184].

Among noble metals, platinum demonstrates the highest work function (5.65 eV) and, thus, lowest Fermi level, and, therefore, the strongest photoexcited electron-extracting capacity from the conduction band of TiO₂, which prolongs the electron lifetime and enhances Pt/TiO₂ catalytic activity compared to bare titania. Notably, Pt has indicated higher selectivity to CH₄ compared to other cocatalysts in photocatalytic CDR [189–191]. In this regard, additional factors, other than the purely electronic, ones should play a crucial role in differentiating Pt nanoparticles, such as surface chemistry and interaction with adsorbates [189,191,192]. Therefore, Pt was deposited on a composite of commercial TiO₂ (Degussa P25) using mesoporous silica (COK-12) to prepare Pt/TiO₂ and Pt/TiO₂-COK-12 photocatalysts with various amounts of Pt. The CO₂ photoreduction test was performed in the presence of H₂O as a reductant under UV light irradiation inside a continuous flow photoreactor. After a 16-h irradiation, H₂, CH₄, and CO were detected as the main products. Moreover, CO was the main product when pure TiO₂ was applied as a photocatalyst. They also found that the optimum amount of Pt can improve CO₂ photoreduction toward CH₄ with approximately 100% selectivity. Furthermore, supporting the Pt/TiO₂ photocatalyst on COK-12 keeps the CH₄ selectivity and also improves the overall photoactivity of the Pt/TiO₂ photocatalyst due to the increment of the surface area and titania dispersion [182,186,193].

Larimi et al. [194] applied supported Pt-TiO₂ photocatalyst on carbonaceous supports such as multi-walled carbon nanotubes (MWCNT), single-walled carbon nanotubes (SWCNT), reduced graphene oxide (rGO), and activated carbon (AC) as a photocatalyst for CO₂ reduction in the presence of water vapor under visible light irradiation in a continuous gas-phase fixed-bed photoreactor. Carbonaceous materials have excellent properties such as high surface area, high mechanical and chemical resistance, and great electron transfer properties. They act as electron acceptor, consequently suppressing the electron-hole recombination of synthesized photocatalyst. As shown in Table 5, the highest CH₄ yield was obtained for Pt-TiO₂/MWCNT (1.9 μmol g_{cat}⁻¹ h⁻¹), which implied that smaller particles improve photocatalytic performance. Furthermore, it implies better catalytic activity compared to the other types of carbonaceous supports Table 5. Co-doped TiO₂ exhibits better

light absorption in the visible range compared to the bare titania and single-doped samples because of the decreasing recombination of photogenerated electron-hole pairs. Among transition metals, nickel has good properties such as high activity for CH₄ production, is cheaper than noble metals, and has better optical properties. Additionally, the electron-hole recombination rate efficiently reduced in the presence of Ni [195–198]. On the other hand, doping Bi ion in TiO₂ shows high CO₂ adsorption and also increases visible light absorption, resulting in improving photocatalytic properties of TiO₂ [199–201]. With all these in mind, different amounts of Ni and Bi were utilized to prepare Ni-doped TiO₂, Bi-doped TiO₂, and co-doped samples. The results showed that the synthesized samples had narrower band-gap energy and significantly increased visible light adsorption with a decreased rate of electron-hole recombination. Ni and Bi atoms can act as trapper for photogenerated electron-hole pairs and reduce the recombination rate. When the doped Ni ions trap the photogenerated charge carriers, the valence layer of the Ni²⁺ (3d8) is changed from high spin state to low spin state, resulting in a remarkable spin energy loss. The trapped charge carriers will migrate to the adsorbed water molecules on the surface to reinstate its energy. This will finally inhibit the recombination of electron-hole (e⁻/h⁺) pairs. Among these samples, 1 wt.% Ni-3 wt.% Bi co-doped TiO₂ demonstrated the highest methane production (21.13 μmol/g_{cat.}), which was about 6.5 times greater than pure TiO₂ [186].

In addition, copper can also inhibit electron-hole pair recombination. Therefore, Spadaro et al. investigated alternative reactor designs for direct conversion of CO₂ exhaust using 0.5 wt% CuO/TiO₂ photocatalysts [202]. The comparison of three different photoreactor systems, a continuously stirred “semi-batch” (SB) photoreactor, a packed-bed (PB) photoreactor, and a multi-tubular (MT) photoreactor, was performed. Different reaction conditions were applied for the systems as follow:

- (a) SB photoreactor: photoreactor tests were carried out in water media and gas mixture of 92% CO₂ and 8% N₂ at room temperature. Then, 1.5 g of photocatalyst and 600 mL of K₂CO₃ solution (0.1 M) were loaded.
- (b) PB photoreactor: 90% gas mixture (i.e., 92% CO₂/N₂) and 10% of water vapor at the saturated pressure of 46 °C were applied. The reaction was performed at room temperature and pipelines were heated at 50 °C to prevent water condensation.
- (c) MT photoreactor: This type of photoreactor was utilized to perform CO₂ photoreduction tests in the industrial environment. For this purpose, a gas treatment unit was utilized to enrich CO₂ content up to 60–80%. Thereafter, the MT photoreactor with 20 Pyrex reactor tubes connected in series was applied. The photoreaction was performed continuously with a stream of 60% CO₂/N₂ at 60–70% of relative humidity (RH).

The obtained results have been showed in Table 3. According to Table 3, TiO₂ promotes CH₄ formation which is two times greater than methanol formation. On the other hand, Cu-TiO₂ demonstrates a low rate of CH₄ formation and a higher rate of CH₃OH formation (47 μmol g_{cat.}⁻¹ h⁻¹) after 60 h irradiation. A comparison between quantum efficiency and thermal energy of MT (0.063% of AQE_{max} and 5 W h/m²) and PB (6% of AQE_{max} and 315 W h/m²) photoreactors implies that PB photoreactor is the greatest performing technical choice [202].

Non-metal dopants create a heteroatomic surface structure, which leads to decreasing the band gap energy, which subsequently increases photoactivity in the visible light region. In other words, dopants narrow down the TiO₂ band-gap through introducing new energy states above VB and promote electrons' excitation from VB to CB. Among various non-metal dopants, nitrogen (N) has been widely studied [25,203,204]. That is because nitrogen has an almost similar atomic size to oxygen, so it is possible to introduced it easily into the titania structure in both substitutional and interstitial positions. Doping with nitrogen can change the band edge of the TiO₂, resulting in extending activity into the visible region. Notably, doping TiO₂ with nitrogen induces optical transitions from N 2p states and the band-gap narrows by mixing with O 2p. Finally, it leads to obtaining better structural and morphological properties [205,206]. Liu et al. [186] synthesized Cu-N-co-doped TiO₂ and

N-doped TiO₂ for CO₂ photoreduction with the presence of water in the liquid phase under UV irradiation. The acetone yield of N₃/TiO₂ and Cu_{0.6}N₄/TiO₂ (Cu: 0.6 wt.% and N: 4 wt.%) were 52.6 and 33.2 μmol/g h, respectively. The obtained results showed that the smaller particle sizes and little higher band gap of the N-doped TiO₂ than Cu-N-co-doped TiO₂ led to improving the UV light absorption and, hence, a higher photoactivity than pure TiO₂. Furthermore, Matejova et al. [207] prepared nitrogen-doped TiO₂ through various methods such as the sol-gel method combined with calcination (N/TiO₂-SG-C), the hydrothermal method combined with calcination (N/TiO₂-HT-C), and the sol-gel method combined with pressurized fluid processing (N/TiO₂-SG-PFE). The prepared photocatalysts were utilized for CO₂ reduction in 0.2 M NaOH solution as a reduction medium under UV light irradiation. CO, CH₄, and H₂ were the detected products with the yields' (μmol g⁻¹cat.) order of CO > H₂ > CH₄. Surprisingly, the presence of nitrogen caused the decline of the formation of all products, in particular over TiO₂-SG-C. In the CO₂ photoreduction, the structure of the surface phase junction within the bicrystalline mixture of anatase and brookite played a crucial role instead of defect sites because it caused decreasing electron-hole recombination. Therefore, the nitrogen loading did not lead to CO₂ photoreduction enhancement.

Table 3. Results of CO₂ photoreduction reaction under UVA 285-W/m² irradiation [202].

Photoreactor.	Photocatalyst.	Product Formation Rate (μmol g _{cat.} ⁻¹ h ⁻¹)			Photoreactor Configuration	
		CH ₃ OH	CH ₄	CO	Energy (Wh/m ²)	AQE _{max} (%)
SB	TiO ₂	4.3	-	-	4.6	1.19
	Cu-TiO ₂	22	-	-		
PB	TiO ₂	5	9	-	315.2	5.7
	Cu-TiO ₂	47	3	-		
MT	Cu-TiO ₂	-	37.5	40	5.3	0.063

3.1.2. Surface Photosensitization

In this method, light-sensitive materials are utilized in conjunction with TiO₂ to facilitate electron transfers from their CB into the TiO₂ CB, as shown in Figure 15. This, in turn, enables TiO₂ to be applicable under visible light [25], in addition to the UV band. That is TiO₂ surface photosensitization is found to improve the photoactivity through modifying the optical features, enabling more effective harvesting of the visible light illumination. Table 5 provides a list of materials investigated as surface sensitizer onto TiO₂. Li et al. [208] used N,S-containing carbon quantum dots (NCQDs) as a sensitizer onto TiO₂ to enhance light absorption through acting as a bridge for carrying and transferring electrons from TiO₂. The nanocomposite was applied as a photocatalyst for CO₂ reduction with H₂O as a reductant and proton donor under solar irradiation. After 1 h irradiation, 0.769 and 1.153 μmol CH₄ and CO, respectively, obtained which are 7.79 and 7.61-fold greater than pristine TiO₂. This photoactivity enhancement of NCQDs/TiO₂ is due to excellent light absorbance and effective charge separation induced by CQDs. Furthermore, photogenerated electrons transfer from TiO₂ to NCQDs, suppressing recombination of photogenerated electron-hole pairs. On the other hand, NCQDs act as electron reservoirs. Ionic liquids (ILs) such as azolate-, alcoholate-, phenolate-, amino acid containing anion- and pyridine-containing anion-based ILs have been also extensively investigated for efficient CO₂ capture at ambient conditions and conversion. Specifically, ILs demonstrate remarkable potential in increasing CO₂ photoreduction nevertheless, few studies have been conducted in this context [209–212]. Recently, Chen et al. [213] applied tetrabutylphosphonium citrazenate ([P₄₄₄₄]₃[p-2,6-O-4-COO]), tetrabutylammonium citrazenate ([N₄₄₄₄]₃[p-2,6-O-4-COO]), and [P₄₄₄₄]₂[pH-2,6-O-4-COO] as ILs and anatase TiO₂. The photoreaction was performed in the dimethyl sulfoxide (DMSO) solution of IL (50%) with triethanolamine (TEOA) as

hole scavenger under visible light irradiation ($\lambda > 420$ nm). The obtained results are shown in Table 5. The IL, $[P_{4444}]_3[p\text{-}2,6\text{-O}\text{-}4\text{-COO}]$, significantly improved CO_2 photoreduction ($3.52 \mu\text{mol g}^{-1} \text{ h}^{-1}$ for CH_4) and selectivity (96.2%) compared to the other ILs, which can be attributed to both the higher absorption capacity to CO_2 and superior visible light absorbance after CO_2 absorption.

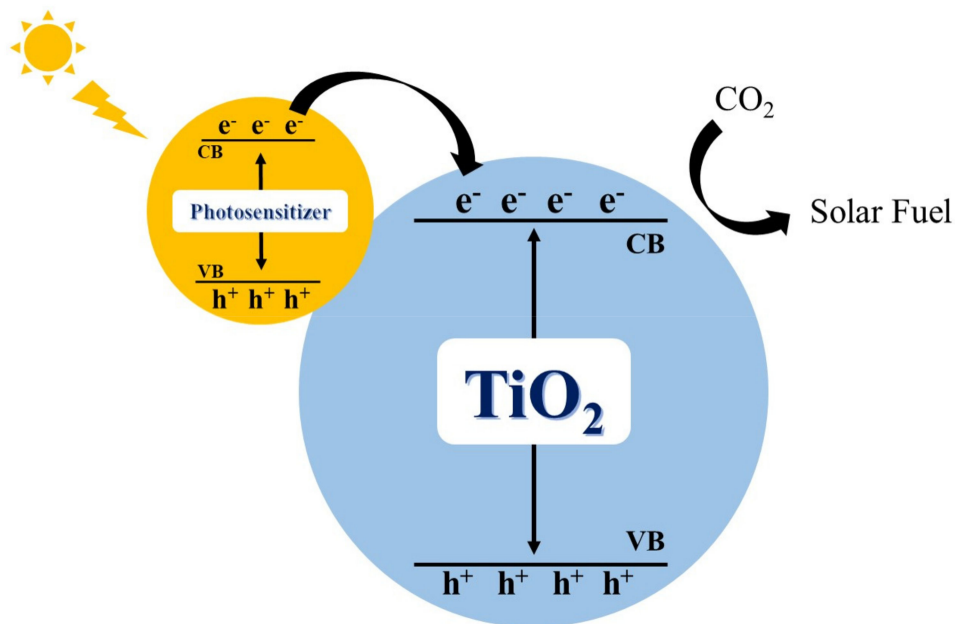


Figure 15. Schematic of the Surface photosensitizer.

Generally, TiO_2 surface photosensitization is highly recommended to improve photoactivity significantly through modifying the optical features so that it can effectively harvest the visible light illumination.

3.1.3. Semiconductor Coupling

Coupling TiO_2 with a low band gap semiconductor can induce red shift to the band gap and reduce electron-hole recombination, improving the photocatalyst performance [214,215]. Xu et al. [216] utilized an amorphous- TiO_2 -encapsulated CsPbBr_3 nanocrystal (CsPbBr_3 NC/- TiO_2) hybrid structure to increase CO_2 photoreduction. This structural improvement influenced significantly the CH_4 production rate which is more thermodynamically favorable than CO and H_2 formation despite the kinetic challenges due to the eight electrons involvement. This hybrid structure increased photoactivity from 2.06 to $20.15 \mu\text{mol}_{\text{CH}_4} \text{ g}_{\text{cat}}^{-1}$ after 3 h photocatalytic reaction (see Table 4). Generally, the photoactivity enhancement was related to accelerated photoinduced charge separation and the multiplied CO_2 adsorption. It is worth mentioning that TiO_2 provides surfaces with high CO_2 adsorption. Furthermore, increasing tetrabutyl titanate (TBT) precursor, decreasing nanocrystal size which would increase the specific surface area of $\text{CsPbBr}_3\text{NC}/\text{a-TiO}_2(x)$, and therefore contributing to the performance of photocatalyst. In this regard, the stable chemical state of CO_2 activated by incorporating with Ti-O bonds, which facilitated the kinetics of subsequent photoreactions. Therefore, a- TiO_2 has a synergistic influence on the increment of photocatalytic performance through charge improvement.

Table 4. CO₂ photoreduction performances after 3 h [216].

Photocatalyst	Production Yield ($\mu\text{mol g}^{-1}$)			Sel. for CO ₂ Reduction (%)	Particle Size (nm)
	H ₂	CO	CH ₄		
CsPbBr ₃ NC	1.64	3.35	2.06	90.3	16.4
CsPbBr ₃ NC/a-TiO ₂ (10)	5.08	7.73	10.12	90.5	13.4
CsPbBr ₃ NC/a-TiO ₂ (20)	4.38	11.71	20.15	95.5	8.5
CsPbBr ₃ NC/a-TiO ₂ (30)	4.42	8.05	14.40	93.7	7.8
CsPbBr ₃ NC/a-TiO ₂ (50)	5.01	8.72	6.47	87.4	5.9

In 2019, Crake et al. [217] synthesized TiO₂/carbon nitride nanosheets' (CNNS) heterostructures using a hydrothermal in situ growth method and utilized for CO₂ photoreduction into CO under UV-Vis light irradiation with H₂ and H₂O as reductant. The TiO₂/CNNS composites synthesized in the presence of HF and deionized water were named Ti-NS/CN and Ti-ISO/CN, respectively. Notably, porosity and surface area are important properties of a photocatalyst, which increase interactions between the reactants and the active sites. In this respect, Ti-NS/CN showed the highest surface area (174 m²g⁻¹) compared to the Ti-ISO/CN (119 m²g⁻¹). Furthermore, the porosity of Ti-NS/CN (V_{total} = 0.294 cm³g⁻¹) was increased compared to the parent materials (V_{total}(TiO₂-NS) = 0.085, V_{total}(CNNS) = 0.141 cm³g⁻¹), which can be attributed to the self-assembly of TiO₂-NS in the presence of CNNS forming a porous structure. Therefore, the Ti-NS/CN structure can provide efficient pathways and enhance the concentration of reactants in the vicinity of catalytic sites. As it was expected, Ti-NS/CN exhibited higher CO evolution rates (2.04 $\mu\text{mol g}^{-1}\text{cat. h}^{-1}$) compared to the Ti-ISO/CN (1.55 $\mu\text{mol g}^{-1}\text{cat. h}^{-1}$). Furthermore, H₂ and O₂ were products in addition to CO when the reaction proceeded in the presence of H₂O over Ti-NS/CN. Under these conditions, CO and H₂ evolution rates were 0.8 and 2.67 $\mu\text{mol g}^{-1}\text{cat. h}^{-1}$, respectively. This decline in CO production was due to the H₂ production from water splitting. On the other hand, under UV-vis illumination, both CNNS and TiO₂ reduced CO₂ to CO because both of them absorb photons and generate electron-hole pairs. The increase of Ti-NS/CN photoactivity was due to the availability of CO₂ and photoexcited electrons. Furthermore, CO₂ concentration on the catalytic sites was increased due to their greater CO₂ adsorption. Additionally, photogenerated electron-hole pairs' recombination was suppressed. In another study [218], chromium (III) oxide (Cr₂O₃), a p-type semiconductor, was utilized to prepare core-shell Cr₂O₃@TiO₂ nanoparticles. The prepared X-Cr₂O₃@TiO₂ (X refers to the calcination temperature) was used as a photocatalyst to reduce CO₂ into CH₄ with H₂O as a sacrificial agent under UV illumination. The results are shown in Figure 16. The highest yield rates for CH₄ increased with increasing calcination temperature from about 105 $\mu\text{mol g}^{-1}\text{cat. h}^{-1}$ for 400-Cr₂O₃@TiO₂ to approximately 168 $\mu\text{mol g}^{-1}\text{cat. h}^{-1}$ for 700-Cr₂O₃@TiO₂. The increment in the CH₄ production over X-Cr₂O₃@TiO₂ core-shell structure was due to the close contact between the formed p-n junction of Cr₂O₃ and TiO₂. Additionally, the formed p-n junction reduced the migration distance of the photogenerated electrons.

In 2020, Iqbal et al. [219] synthesized ZnFe₂O₄/TiO₂ heterojunctions for CO₂ photoreduction into methanol under visible light illumination. The BET surface areas of ZnFe₂O₄, ZnFe₂O₄/TiO₂ (2:1 w/w), and ZnFe₂O₄/TiO₂ (1:1 w/w) were 2.479, 5.027, and 6.521 m²g⁻¹, respectively. Therefore, ZnFe₂O₄/TiO₂ (1:1 w/w) had highest BET surface area and better morphological structure. Furthermore, ZnFe₂O₄/TiO₂ (1:1 w/w) showed the highest methanol yield, 693.31 $\mu\text{mol g}^{-1}\text{cat.}$, which highlights the importance of surface area in heterogenous catalysis.

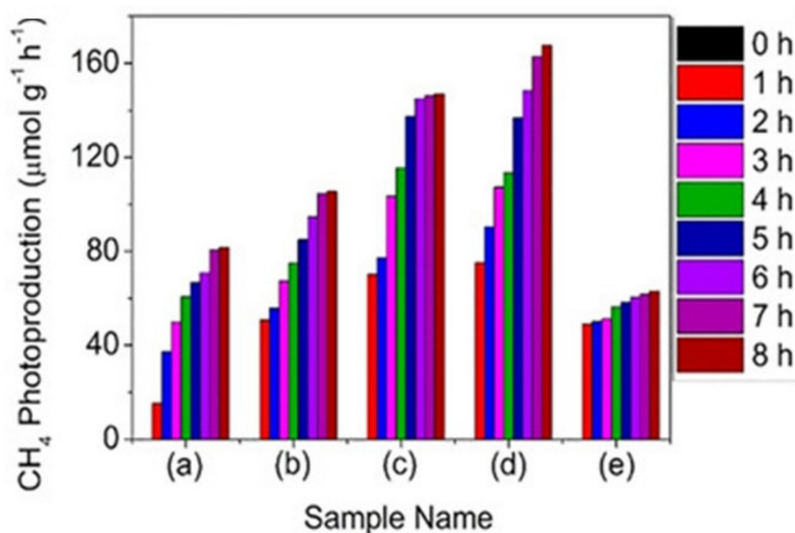


Figure 16. CH₄ photoreduction using Cr₂O₃ coupled with TiO₂ photocatalysts showing (a) Cr₂O₃, (b) 400-Cr₂O₃@TiO₂, (c) 550-Cr₂O₃@TiO₂, (d) 700-Cr₂O₃@TiO₂, and (e) 850-Cr₂O₃@TiO₂ [218].

3.2. CO₂ Photoreduction by Metal-Organic Frameworks (MOFs)

MOFs as new porous hybrid materials that are composed of organic linkers and metal ions have unique properties such as extremely large surface area (up to 8000 m²g⁻¹), uniform and tunable porous structure, and tailorabile chemistry, which have led to the development of these materials as potential photocatalysts for CO₂ reduction [220,221]. In 2006, Garcia et al. [222] made a historic work, which has drawn widespread attention toward MOFs as a new type of promising photocatalysts. In order to accelerate the photogenerated charge separation and transfer and, consequently, increasing photocatalytic performance, different forms of MOFs are utilized as photocatalyst. Furthermore, MOFs' light absorption ability can be facilely tuned by modifications on the metal ions and the organic linkers, owing to versatile coordination chemistry of the metal cations, availability of variety organic linkers, and the feasibility to modulate the composition, structure, and properties of the MOFs. Therefore, efficient utilization of solar energy by MOFs can be obtained [223]. These modification methods will be discussed in the following sections.

3.2.1. NH₂-Modified MOF

Among different functional groups, amine groups are most investigated for functionalizing MOFs due to their strong affinity to acidic gas molecules, and they also can provide active sites for catalysis. In this respect, NH₂-MIL-125 (Ti) was synthesized by using 2-aminoterephthalate acid (H₂ATA) as an organic linker to utilize as a photocatalyst for CO₂ reduction. The photoreaction was performed in the presence of triethanolamine (TEOA) as a sacrificial agent under visible light irradiation. After a 10-h illumination, the parent MIL-125 (Ti) did not show any photoactivity, whereas NH₂-MIL-125 (Ti) demonstrated moderate activity, with 8.14 μmol HCOO⁻ produced. These results confirmed the visible light photoactivity of NH₂-MIL-125 (Ti) was induced by amino functionality, which was also confirmed by UV/Vis spectra, Figure 17 [224].

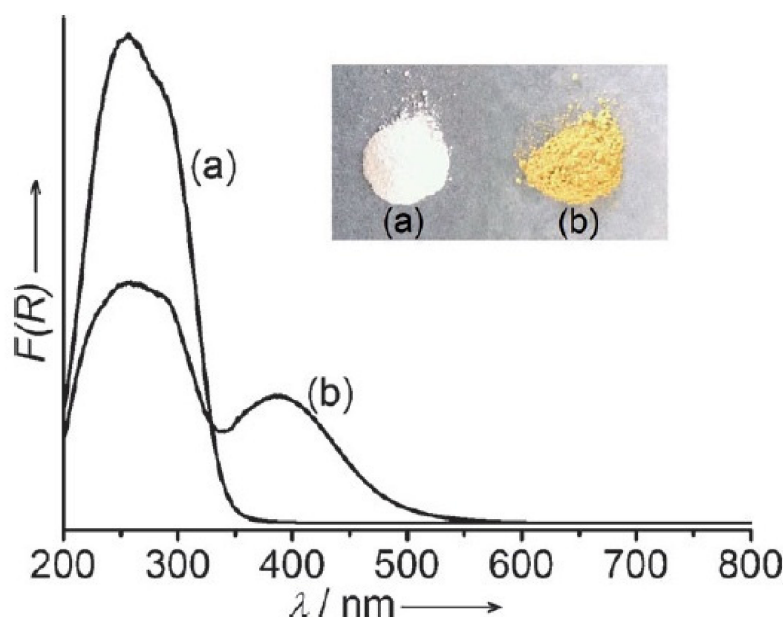


Figure 17. UV/Vis spectra of (a) MIL-125 (Ti) and (b) NH₂-MIL-125 (Ti) [224].

In another study [225], NH₂-UiO-66(Zr) was utilized as a photocatalyst for CO₂ reduction and showed higher photocatalytic activity than a prior study, NH₂-MIL-125(Ti), under visible-light irradiation. It is worthy to note that the RedOx potential of Zr^{IV}/Zr^{III} is more negative than Ti^{IV}/Ti^{III}, which is more favorable for CO₂ photoreduction reaction. Furthermore, UiO-66, a zirconium-based MOF, is a potential material for CO₂ capture and storage because of its higher chemical and thermostability compared to NH₂-MIL-125(Ti). Furthermore, UiO-66 shows semiconductor behavior that can promote charge transfer and harvest solar light. Besides, the prepared, mixed NH₂-UiO-66 (Zr), which was synthesized by mixing 2-aminoterephthalate (ATA) and 2,5-diaminoterephthalic acid (H₂DTA), demonstrated an improvement in photoactivity of >50% compared with the pure NH₂-UiO-66(Zr) for the reduction of CO₂, which was attributed to the increasing of both CO₂ adsorption and light adsorption in the visible region. Iron is an earth-abundant element. Fe-containing complexes are generally utilized as catalysts and photocatalysts. Particularly, Fe-based MOF materials are highly attractive due to their visible-light-response, which originates from Fe-O clusters. Therefore, a series of both parent and amine-functionalized Fe-containing MOFs (MIL-101 (Fe), MIL-53 (Fe), MIL-88B (Fe)) were applied as a photocatalyst for CO₂ reduction, producing formate under visible light irradiation. While a remarkable increase in photoactivity was observed for all assessed materials, MIL-101(Fe) and its amino-functionalized structure showed the best photoactivity of 59 and 178 $\mu\text{mol HCOO}^-$, respectively. That was attributed to the existence of dual pathways: (1) direct excitation of Fe-O clusters and (2) NH₂ functionality excitation followed by an electron transfer to the metal center. This phenomenon is schematically shown in Figure 18. Generally, this study confirmed that the structure of the MOF can significantly influence photocatalytic activity [226].

In order to improve the photoactivity of NH₂-UiO-66, for the first time, Cheng et al. [22] used 2,4,6-tris (4-pyridyl) pyridine (tpy). The tpy facilitated charge transfer because of its strong electron-donating ability and can lead to improvement in CO₂ to CO conversion as illustrated in Figure 19a, therefore, the performance of modified MOF is improved for CO₂ photoreduction reaction. Furthermore, commensurate with this Figure 19b presents the variations of the CO evolution as a function of the time and clearly shows that the photocatalytic performance of NH₂-UiO-66-tpy is greatly improved for CO₂ reduction in comparison with the NH₂-UiO-66.

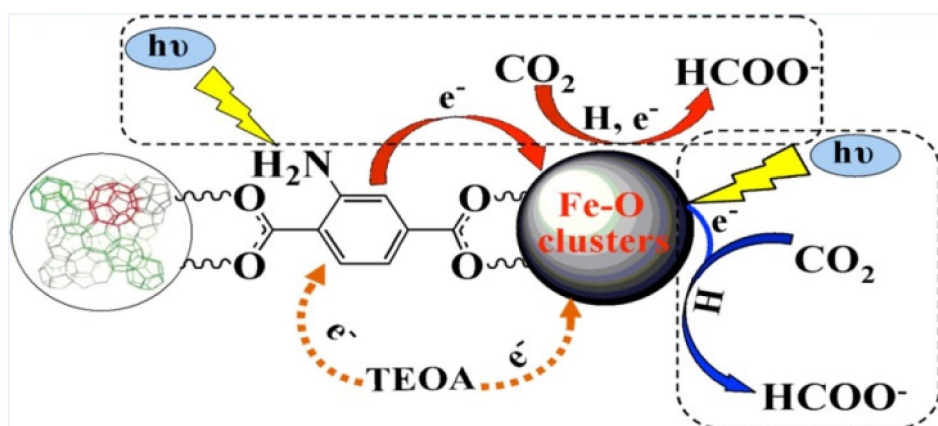


Figure 18. Reaction pathways over $\text{NH}_2\text{-MOFs (Fe)}$ [226].

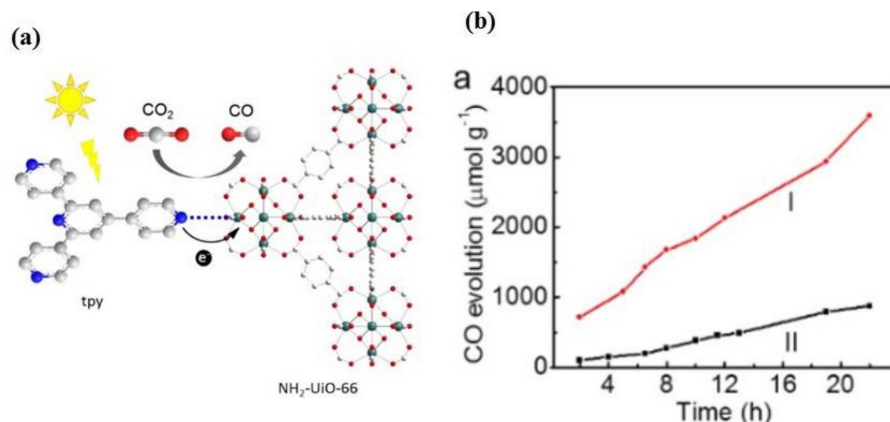


Figure 19. (a) Reaction pathway of CO_2 photoreduction over $\text{NH}_2\text{-UiO-66-tpy}$. N: blue, O: red, Zr: indigo, C: light gray. (b) CO evolution over $\text{NH}_2\text{-UiO-66-tpy}$ (I) and $\text{NH}_2\text{-UiO-66}$ (II) as a function of time [22].

3.2.2. Semiconductor MOF Composite

Since semiconductor photocatalysts have high CO_2 photoreduction activity, also, MOF materials have great CO_2 capture ability, the incorporation of these two materials is a useful method to design and synthesize composite photocatalysts that integrate the advantages of both materials. The integration of semiconductor and MOF structures possess better capability on light harvesting because of the synergistic effect [227]. Conjugated graphitic carbon nitride ($\text{g-C}_3\text{N}_4$) polymers possess an extreme thermal stability up to $550\text{ }^\circ\text{C}$ in air and high chemical stability, high specific surface area, with great semiconductor RedOx energetics for CO_2 reduction [228–230]. Furthermore, zeolitic imidazolate frameworks (ZIFs) have excellent structural stability in water, high thermal and chemical stability, also, have excellent CO_2 adsorption properties [231]. Wang et al. [232] investigated $\text{g-C}_3\text{N}_4$ integrated with cobalt-containing zeolitic imidazolate framework (Co-ZIF-9) for CO_2 conversion under visible light illumination. Besides, bipyridine (bpy) and TEOA were utilized as an auxiliary electron mediator and electron donor to reduce CO_2 into CO , Figure 20a. As illustrated in Figure 20b, the rate of CO production increased throughout the reaction. However, this increase was more significant in the first 2 h of the experiment, which was attributed to the CO_2 and bpy depletion/degradation, while Co-ZIF-9 and $\text{g-C}_3\text{N}_4$ are stable to retain their intrinsic reactivity. In addition, the stability of the photocatalyst was investigated by introducing fresh bpy and CO_2 into the reaction after each 2 h of reaction. Obtained results implied that the original catalytic activity was not changed even after seven repeated operations (Figure 20b, inset).

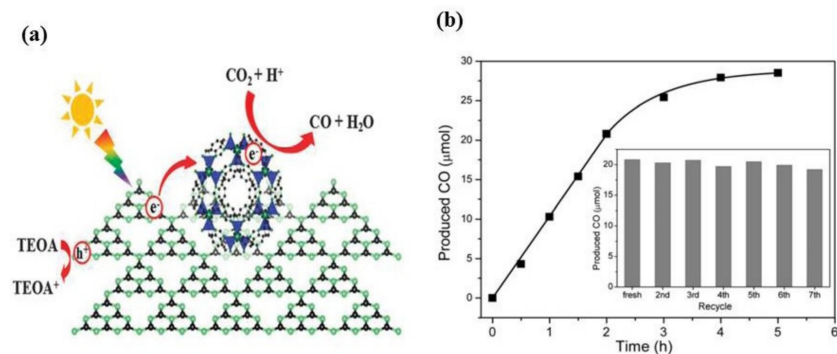


Figure 20. (a) Reaction pathway of the cooperation of Co-ZIF-9 and g-C₃N₄ for CO₂ photoreduction under visible light illumination, (b) CO production from the Co-ZIF-9 and g-C₃N₄-based hybrid system as a function of the reaction time. Inset: recycling tests for CO₂ photocatalytic reduction under visible light illumination [232].

To increase the efficiency of the photocatalysts for gaseous reactions, it can be integrating the gas adsorption into MOF with electron-hole generation by an inorganic semiconductor which can efficiently transfer photoexcited electrons from the semiconductor to the MOF. In this respect, Cu₃(BTC)₂@TiO₂ core-shell structure was utilized as a photocatalyst to reduce CO₂ into CH₄ under UV-light irradiation in the presence of the H₂O in the gas phase. As shown in SEM and TEM images (Figure 21), the synthesized core-shell structures preserve the octahedral profile of the Cu₃(BTC)₂ cores and the layer of shell formed on it, Figure 21a,b. Their results show that the photogenerated electrons can be efficiently transferred from TiO₂ (shell) to the Cu₃(BTC)₂ (core) which promotes charge separation in the semiconductor. Furthermore, it supplies energetic electrons to gas molecules adsorbed on Cu₃(BTC)₂. Besides, the microporous structure of TiO₂ improves gas molecules capture in the cores (Cu₃(BTC)₂) and create adequate surface area. As demonstrated in Table 5, the yield of produced CH₄ with Cu₃(BTC)₂@TiO₂ was over five times more than pure TiO₂ under same reaction conditions. In addition, no products were found except CH₄ which implies that the selectivity of CO₂ to H₂O is significantly improved through this catalyst design [233]. CO₂ photoreduction reaction can proceed in two pathways to produce CH₄, formaldehyde and carbene pathways, which are illustrated in Figure 22 [234].

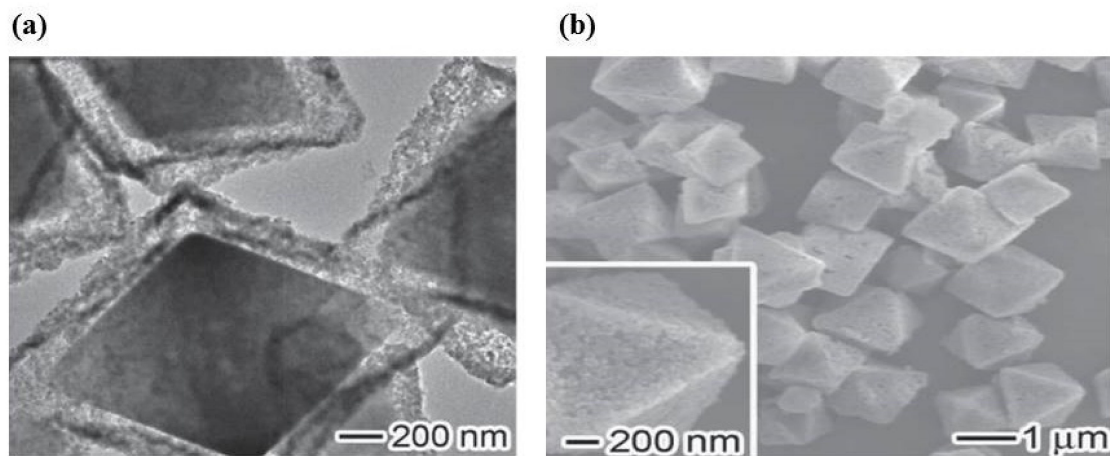


Figure 21. (a) TEM and (b) SEM images of the synthesized Cu₃(BTC)₂@TiO₂ core-shell structures [233].

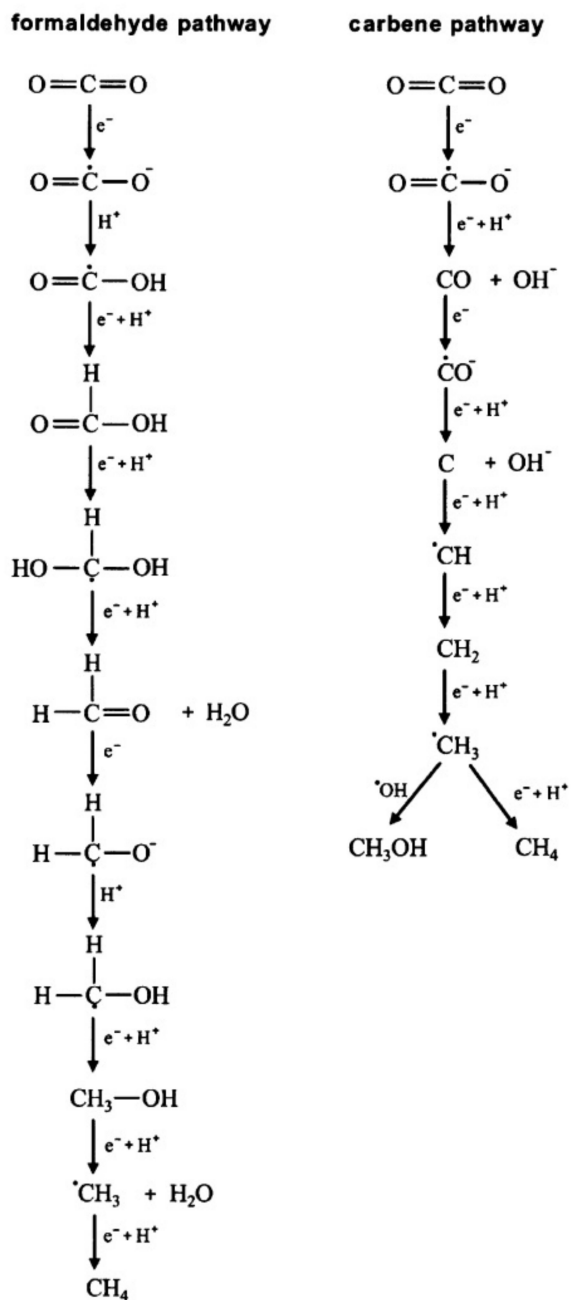


Figure 22. Two proposed pathways for the CO_2 photoreduction into CH_4 : formaldehyde (left) and carbene (right) [234].

Graphene-based materials have drawn attention because of their great properties, e.g., high surface area (up to $2600 \text{ m}^2 \text{ g}^{-1}$), tunable band gap, mechanical and chemical stability, high electrical and thermal conductivity that makes them as potential photocatalysts. Besides, graphene as an excellent electron acceptor-transporter plays significant role in increasing the transfer and preventing electron-hole pairs recombination, resulting in improving the photoactivity of CO_2 reduction [55,235–237]. Graphene-based MOF ($\text{NH}_2\text{-rGO}/\text{Al-PMOF}$) was applied for CO_2 photoreduction. For this purpose, tetrakis (4-carboxyphenyl) porphyrin (TCPP) was utilized as a ligand to prepare Al-PMOF. To find out the impact of the graphene on the structure and performance of photocatalyst, different percentages of $\text{NH}_2\text{-rGO}$ were utilized to synthesize $\text{NH}_2\text{-rGO}$ (0, 5, 15, 25 wt.%) / Al-PMOF. Figure 23 compares the SEM images of the morphology of the prepared samples. As shown, the morphology of the photocatalyst was changed from cubes to platelets with increas-

ing the amount of NH₂-rGO, which, in turn, led to increasing the electrons' generation, enhancing the accessibility to the CO₂ molecules, resulting in increment in CO₂ photoreduction. Moreover, the thin platelets of NH₂-rGO (25 wt %)/Al-PMOF were observed to agglomerate, which decreased the crystallinity of the structure, preventing the irradiated light adsorption by photocatalyst and, consequently, the generation rate of photoinduced electron-hole pairs was reduced. In other words, with increasing NH₂-rGO content in the structure, the Al-PMOF molecules were wrapped by NH₂-rGO sheets, which can act like a shield to prevent the light adsorption. Therefore, the photocatalyst activity for CO₂ reduction was decreased. The photoreactor test of NH₂-rGO (5 wt %)/Al-PMOF showed significant photoactivity for CO₂ reduction. The amount of produced HCOO⁻ was continuously increased to 205.6 μmol after a 6-h visible-light irradiation in the presence of TEOA as a sacrificial agent, which was significantly higher than values obtained in other studies [238].

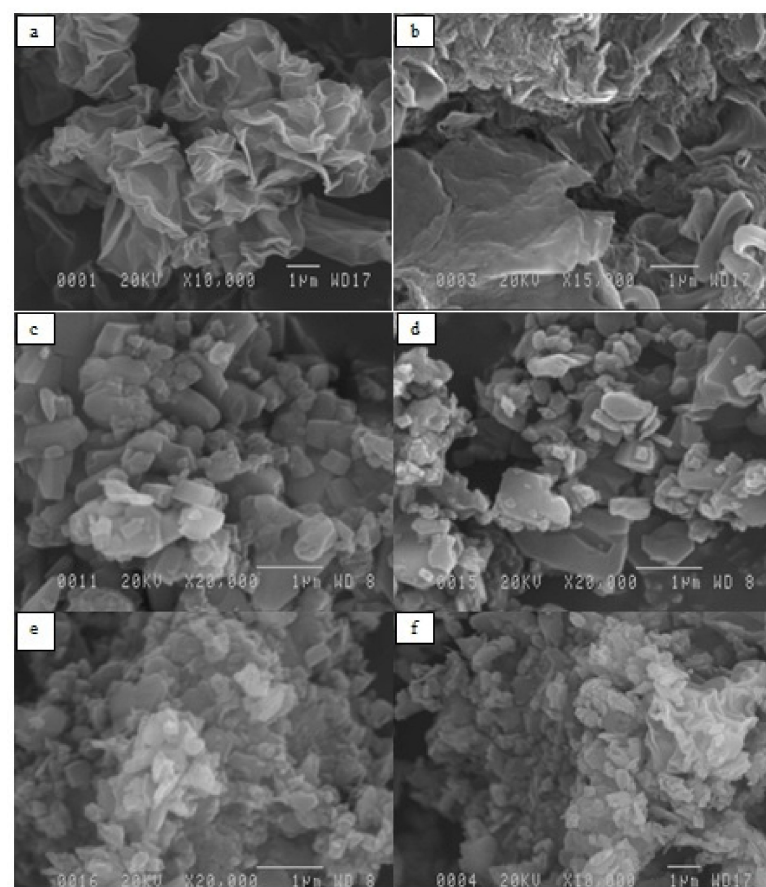


Figure 23. SEM images of (a) GO, (b) NH₂-rGO, (c) Al-PMOF, (d) NH₂-rGO (5 wt %)/Al-PMOF, (e) NH₂-rGO (15 wt %)/Al-PMOF, and (f) NH₂-rGO (25 wt %)/Al-PMOF [238].

The synthesized ternary photocatalysts' structure could integrate the advantages of each component such as high CO₂ adsorption capability, efficient light adsorption, and rich, accessible, active sites. In this context, the leaf-like zeolitic imidazolate frameworks (ZIF-L) were grown on a branch-like TiO₂/C nanofiber to fabricate different leaf–branch TiO₂/C@ZIF-L composite photocatalysts. Notably, the CO₂ photoreduction was performed without the addition of any sacrificial reagents. Additionally, the metal Lewis sites in ZIF-L are interesting for converting CO₂ into CO. The existing Lewis sites in the MOF structure promoted CO₂ activation to form a *COOH intermediate, which was favorable in terms of CO selectivity improvement. The CO production rate of TiO₂/C@ZnCo-ZIF-L was 28.6 μmol h⁻¹ g⁻¹, which was more than those of TiO₂/C@Co-ZIF-L and TiO₂/C@Zn-ZIF-L, 22.7 and 18.7 μmol h⁻¹ g⁻¹, respectively. On the contrary, TiO₂@ZnCo-ZIF-L showed a

low CO production rate, $6.6 \mu\text{mol h}^{-1} \text{g}^{-1}$. These results implied that graphitic carbon with superior electron mobility plays a crucial role for accepting and transferring electrons between TiO_2 and ZnCo-ZIF-L [239]. Since the bandgap of the PCN-224(Cu) is narrow, about 1.68 eV, it can absorb solar light. Furthermore, it contains a nitrogen-rich skeleton, providing higher CO_2 adsorption during the photocatalysis process. Therefore, coupling PCN-224(Cu) with other semiconductors can promote light absorption and suppress the electron-hole recombination due to the accelerated charge transfer [240,241]. Wang et al. [242] formed a photocatalyst by the growth of TiO_2 PCN-224 (Cu) (simplified as P(Cu)) to prepare P(Cu)/ TiO_2 composites. As shown in Table 5, the sample of 15% P(Cu)/ TiO_2 was an optimal photocatalyst with the highest potential for CO production. The photocatalytic performance of prepared photocatalysts increased with increasing P(Cu) content. This was attributed to the increasing of the charge separation efficiency at the interface between TiO_2 and P(Cu) as a result of the broad absorption edge. Notably, increasing P(Cu) content from 15% to 30% decreased photoactivity, which was speculated to be due to the side reaction of $\text{O}_2 + 2\text{H}^+ + 2\text{e}^- \rightarrow \text{H}_2\text{O}_2$, which can be dominant over P(Cu).

3.2.3. Metal-MOF Composite

Metal-MOF composites as an important type of MOF were studied. The d-block transitions metals were the most applied metals due to their d-block electrons showing great functionality regarding their complex-forming capability and acid–base interactions. Furthermore, more than one type of metal atom also can be utilized in composites [243,244]. The M-doped $\text{NH}_2\text{-MIL-125}$ (Ti) (M = Pt and Au) was synthesized and applied as a photocatalyst in saturated CO_2 with TEOA as a sacrificial agent under visible-light irradiation. The results showed that both hydrogen and formate were produced over the M/ $\text{NH}_2\text{-MIL-125}$ (Ti) photocatalyst and the rate of formate evolution was promoted compared with the use of pure $\text{NH}_2\text{-MIL-125}$ (Ti) as a photocatalyst. On the contrary to the pure $\text{NH}_2\text{-MIL-125}$ (Ti), hydrogen was produced as the main product over M/ $\text{NH}_2\text{-MIL-125}$ (Ti) under similar conditions. Notably, Pt and Au had different effects on photocatalytic activity for formate formation. While Pt/ $\text{NH}_2\text{-MIL-125}$ (Ti) was found to increase the photoactivity for formate formation, Au showed a negative effect on this reaction [245]. Recently, Guo et al. [20] applied a bimetallic photocatalyst, Ni/Mg-MOF-74, in pure CO_2 in the presence of MeCN/TEOA (5:1 v/v) as a sacrificial agent and $[\text{Ru}(\text{bpy})_3]\text{Cl}_2$ (bpy = 2,2'-bipyridine) as a photosensitizer. The reaction was performed under visible-light illumination for 0.5 h. It was observed that $\text{Ni}_{0.75}\text{Mg}_{0.25}\text{-MOF-74}$ has the highest formate evolution rate of $0.64 \text{ mmol h}^{-1} \text{ g}^{-1}$, which was more than $\text{Ni}_{0.87}\text{Mg}_{0.13}\text{-MOF-74}$, $0.54 \text{ mmol h}^{-1} \text{ g}^{-1}$. Meanwhile, the monometallic photocatalyst Ni-MOF-74 showed $0.29 \text{ mmol h}^{-1} \text{ g}^{-1}$ and Mg-MOF-74 was inactive. All of these results exhibit that the reactivity of photocatalysts rely on metal nodes.

3.2.4. Other Forms of MOF-Based Photocatalyst

In comparison with all the transition metals, e.g., copper, vanadium, and chromium, cobalt is applied as the most efficient dopant to enhance the light response and photoactivity of TiO_2 , besides acting as an active component for photo/electrochemical water oxidation. Generally, cobalt-based materials have attracted intense research interest because of their low cost and toxicity, earth abundance, and simple RedOx transformation between different chemical valence states, resulting in a high performance with tunable properties [220,246,247]. A Cobalt-containing zeolitic imidazolate framework (Co-ZIF-9) was utilized as a cocatalyst with a ruthenium-based photosensitizer to convert CO_2 into CO. The obtained turnover number (turnover number is the number of reacting molecules or product molecules formed per surface active site for heterogeneous photocatalyst) was about 450 after 2.5 h [248]. In addition, 2D Co/PMOF was synthesized by utilizing TCPP as a linker and cobalt as a node and applied as a photocatalyst for CO_2 reduction into formate (HCOO^-) under visible-light irradiation in the presence of TEOA as a sacrificial agent. They assumed that the formed C-O-metal bond acted as the electron charge transfer

channel between TCPP and Co and accelerated the ligand-to-metal charge transfer (LMCT). The photocatalytic properties of the TCPP ligand behaved as a light-harvesting unit controlled and modified by inserting the metal cations into the porphyrin ring. Co/PMOF had significant metal coordination stability due to the chelation effect of the aromatic ligand and occupied cis-coordination sites, which can hinder different possible side reactions and result in a selective photocatalyst process [220]. Chambers et al. [249] utilized UiO-67 and Cp^{*}Rh (Cp^{*} = pentamethylcyclopentadiene) to prepare a Cp^{*}Rh@UiO-67 photocatalyst with different percentages of rhodium loading. The low rhodium loading catalysts not only showed higher initial rate selectivity for formate but also unprecedented stability and recyclability. On the contrary, formate selectivity was lost at a larger loading because of the decomposition of formate into CO₂ and H₂ catalyzed by UiO-67. In another study [21], Al-PMOF was synthesized utilizing TCPP as a ligand and denoted as S_p, and then Cu²⁺ was embedded in the structure (denoted as S_{Cu}). The prepared photocatalysts were applied to reduce CO₂ into CH₃OH in the presence of triethylamine (TEA) as a sacrificial agent. The CH₃OH generation rate with S_{Cu} (262.6 ppm g⁻¹ h⁻¹), which was higher than that of S_p (37.5 ppm g⁻¹ h⁻¹), indicated that the incorporation of coordination-unsaturated Cu²⁺ improved CO₂ adsorption ability and, consequently, improved photocatalyst performance. Sadeghi et al. [250] used TCPP as a ligand to prepare Zn/PMOF and applied it as a photocatalyst to reduce CO₂ in the presence of H₂O vapor as a sacrificial electron donor. The results showed that the CO₂ conversion when using Zn/PMOF (10.43 μmol) was ~80.6% greater than bare ZnO. On the other hand, no other products were detected, which confirmed the reaction over Zn/PMOF had high selectivity. Notably, from the reader's perspective, to avoid prolonging the article, other studies in each section are summarized in Table 5. to get a quick glance of the development. It is worth noting that it is hard to decide which experiment or photocatalyst is better or has the best activity because of different issues: (1) Different sacrificial agents were applied, which leads to producing different products, and (2) photoreduction reactions were performed in the different photoreactors under different conditions. Therefore, there is a lack of widely adopted, standardized, and complete reporting of reactor operating conditions such as illumination intensity and spectral distribution of the light source; furthermore, different conventions were used in normalizing production rates, with a lack of reference calibrations. With all these in mind, comparing different studies by different research groups remains a challenge. Notably, from the reader's perspective, to avoid prolonging the article, other studies in each section have been summarized in Table 5 to get a quick glance of the development.

Table 5. Photocatalytic CO₂ reduction systems.

	Reaction Media	Light Source	Product	Product Formation Rate [μmol h⁻¹g⁻¹]	Comment	References
TiO ₂ -Based Photocatalyst						
Metals and Non-metals Doping	10 wt.% In/TiO ₂	H ₂ O vapor	UV light	CH ₄ CO C ₂ H ₄ C ₂ H ₆ C ₃ H ₆ C ₃ H ₈ CH ₄ CO C ₂ H ₄ C ₂ H ₆ C ₃ H ₆ C ₃ H ₈	244 81 0.06 2.78 0.02 0.02 31 46 0 0 0 0	[182]
TiO ₂					The Bi ion has appropriate conductivity and remarkable CO ₂ adsorption. Therefore, the presence of Bi in the Bi-TiO ₂ structure enhanced the number of adsorbed CO ₂ and H ₂ O molecules.	
5 mol% Bi-TiO ₂	H ₂ O vapor	UV light	CH ₄	34,000		[251]
N ₃ /TiO ₂ Cu _{0.6} N ₄ /TiO ₂ N/TiO ₂ -SG-PFE	water 0.2 M NaOH	UV light	CH ₃ COCH ₃ CO CH ₄ H ₂	52.6 33.2 0.2 0.0014 0.012		[184] [207]

Table 5. Cont.

Reaction Media	Light Source	Product	Product Formation Rate [$\mu\text{mol h}^{-1}\text{g}^{-1}$]	Comment	References	
TiO ₂ /MgO-1%	0.1 M NaOH	UVC light ($\lambda_{\max} = 253.7 \text{ nm}$)	HCOOH CH ₃ COOH CH ₄ CO	0.8125 1.037 1.437 2.946	With increasing the amount of MgO, the catalytic efficiency decreased due to the full coverage of the TiO ₂ by MgO layers, consequently hindering the transferring of the photogenerated charge carriers at the TiO ₂ surface and thereby photoactivity was reduced.	[252]
TNi ₁ Bi ₃ Pt-TiO ₂ /MWCNT Pt-TiO ₂ /SWCNT Pt-TiO ₂ /rGO Pt-TiO ₂ /AC	H ₂ O vapor	Visible light	CH ₄	2.113	[186] [194]	
	H ₂ O vapor	Visible light	CH ₄	1.9		
				0.7		
				0.5		
				0.16		
0.3% Mo-doped TiO ₂	H ₂ O vapor	Xe lamp (300 W)	CO CH ₄	13.67 16.33	CH ₄ selectivity increased with increasing Mo concentration to 0.3 wt.%. Thereafter, CH ₄ selectivity decreased with increasing Mo concentration.	[253]
Surface Sensitizer	NCQDs/TiO ₂	H ₂ O vapor	Solar	0.769	[208]	
			CH ₄	1.153		
TiO ₂ -[P ₄₄₄₄] ₃ [p-2,6-O-4-COO]	TEOA	Visible light ($\lambda > 420 \text{ nm}$)	CH ₄ H ₂	3.52 0.14	This was attributed to the decrease in electron-hole separation efficiency.	[213]
TiO ₂ -[P ₄₄₄₄] ₂ [p-2-O-4-COO]			CH ₄	0.19		
TiO ₂ -[P ₄₄₄₄] [p-2-O]			CH ₄	0.17		
TiO ₂ -[P ₄₄₄₄] [p-4-COO]			CH ₄	0.1		
Other Semiconductors	CsPbBr ₃ NC/a-TiO ₂ (20)		CH ₄	0.07	[216]	
			CH ₄	0.1		
			H ₂	0.06		
			CH ₄	6.72		
			CO	3.9		
			H ₂	1.46		
			H ₂	0.55		

Table 5. Cont.

Reaction Media	Light Source	Product	Product Formation Rate [$\mu\text{mol h}^{-1}\text{g}^{-1}$]	Comment	References	
Ti-NS/CN	H ₂	UV-Vis. light	CO	2.04	[217]	
Ti/ISO/CN			CO	1.55		
Ti-NS/CN	H ₂ O		CO	0.8		
			H ₂	2.67		
700-Cr ₂ O ₃ @TiO ₂	H ₂ O	UV light	CH ₄	167.69	[218]	
			CO	0.488		
ZnFe ₂ O ₄ /TiO ₂ (1:1)	Na ₂ S, Na ₂ SO ₃ , KOH in water	Visible light	CH ₃ OH	693.31	[219]	
ZnFe ₂ O ₄ /TiO ₂ (1:2)				519.69		
ZnFe ₂ O ₄ /TiO ₂ (2:1)				33.53		
(20)TNPs-CN/450	CH ₄	Solar simulator ($\lambda = 320\text{--}780\text{ nm}$)	CO	4.71	The sensitivity factors were investigated and implied the order of F _C (Catalyst amount) > F _E (Calcination temperature) > F _B (CH ₄ to CO ₂ ratio) > F _D (TNPs loading) > F _A (Absolute pressure). [254]	
(20)P ₂₅ -CN/450				2.77		
Bulk g-C ₃ N ₄				2.275		
MOF-Based Photocatalyst						
NH ₂ -Modified MOFs	MIL-125 (Ti)	MeCN/TEOA (5:1)	Visible light	HCOO [−]	0	[224]
NH ₂ -MIL-125 (Ti) UiO-66(Zr)	MeCN/TEOA (5:1)	Visible light	HCOO [−]	16.28	In addition to TEOA, benzyl alcohol, ethylenediaminetetraacetic, and methanol were utilized as reaction media and no HCOO [−] was produced	[225]
NH ₂ -UiO-66(zr) MIL-101 (Fe)	MeCN/TEOA (5:1)	Visible light	HCOO [−]	0		
NH ₂ - MIL-101 (Fe) MIL-53 (Fe)				26.4	MIL-101 (Fe) demonstrated the best photocatalytic performance due to the presence of coordination unsaturated Fe metal sites (CUSs) in its structure. [248]	
NH ₂ -MIL-53 (Fe) MIL-88(Fe)				147.5		
NH ₂ -MIL-88(Fe)				445		
				74.25		
				116.25		
				22.5		
				75		

Table 5. Cont.

Reaction Media	Light Source	Product	Product Formation Rate [$\mu\text{mol h}^{-1}\text{g}^{-1}$]	Comment	References
NH ₂ -UiO-66 (Zr)	MeCN/TEOA (4:1) BNAH (0.1 M)	Visible light	HCOO [−] 0	Introducing Ti ions into UiO-66 structure created new energy levels and broader light absorption and also improved charge transfer, which increased photoactivity of the MOF structure.	[255]
NH ₂ -UiO-66 (Zr/Ti) (NH ₂) ₂ -UiO-66 (Zr/Ti)	MeCN/TEOA (11:1)	Simulate sunlight ($350 < \lambda < 780$ nm)	CO 741 1052.3 ± 54.7		
NH ₂ -UiO-66			34		
NH ₂ -UiO-66-tpy			209.2		
g-C ₃ N ₄ -Co-ZIF-9	MeCN/H ₂ O/TEOA (3:2:1)20 mg g-C ₃ N ₄ , 10 mg bpy, 1 mg MOF cocatalyst	Visible light ($\lambda > 420$ nm)	CO 495		
TiO ₂ -Co-ZIF-9	H ₂ O vapor	Visible light ($200 < \lambda < 900$)	H ₂ 78.6 CO 8.8		[248]
Zn ₂ GeO ₄ -Zn-ZIF-8 TiO ₂ @Cu ₃ (BTC) ₂ HKUST-1/TiO ₂	Na ₂ SO ₃ (0.1 M) H ₂ O vapor	500 W Xe arc lamp UV light	CH ₃ OH CH ₄ H ₂ CO 0.22 2.64 ^a 256.3 ^a	Cocatalyst Co-ZIF-9 can facilitate CO ₂ adsorption and activation and also improve charge transfer.	[256]
TiO ₂			CO 11.48 ^a	HKUST-1 was selected because of the high porosity and surface area, about 40.7% and over 600 m ² /g, respectively. Introducing TiO ₂ into the HKUST-1 matrix increased CO ₂ photoreduction efficiency. Additionally, the hydrophilicity of HKUST-1 led to simultaneous adsorption of water (H ₂ O), resulting in improving CO ₂ photoreduction processes.	[231] [233] [257]

Table 5. *Cont.*

Reaction Media	Light Source	Product	Product Formation Rate [$\mu\text{mol h}^{-1}\text{g}^{-1}$]	Comment	References		
TiO ₂ -Mg-CPO-27	H ₂ O vapor	UV lamps ($\lambda = 365$)	CO CH ₄	4.09 2.35	CPO-27-Mg was selected due to the superior CO ₂ adsorption capacity (about 35.2 wt.%) and consisted of great concentration of alkaline metal sites (Mg ²⁺), which led to improved CO ₂ activation.	[258]	
CNNS-UiO-66 (Zr) CNNS UiO-66 (Zr)	MeCN/TEOA (4:1)	Visible light ($400 < \lambda < 900$)	CO	2.9 0.99 0		[259]	
TiO ₂ -NH ₂ -UiO-66 (Zr) (18.5%) ^b TiO ₂ NH ₂ -UiO-66 (Zr) NH ₂ -rGO (5 wt%)/Al-PMOF Al-PMOF	CO ₂ /H ₂ (1.5:1)	Visible light $\lambda > 325$	CO	4.24 2.85 1.5		[260]	
TiO ₂ /C@ZnCo-ZIF-L TiO ₂ /C@Co-ZIF-L TiO ₂ /C@Zn-ZIF-L TiO ₂ /C ZIF-L	MeCN/TEOA (5:1)	Visible light	HCOO [−]	685.6 165.3		[238]	
PCN-224 (Cu)	-	Visible light	CO	28.6 22.7 18.7 7.8 0.36		[239]	
6% PCN-224 (Cu)/TiO ₂ 7.5% PCN-224 (Cu)/TiO ₂ 10% PCN-224 (Cu)/TiO ₂ 15% PCN-224 (Cu)/TiO ₂ 30% PCN-224 (Cu)/TiO ₂	Water	Xe lamp ($\lambda > 300$)	CO	3.72 19.35 26.78 31.67 37.21 26.04 0.82		[242]	
Metal-MOF composite	Pt/NH ₂ -MIL-125(Ti) Au/NH ₂ -MIL-125(Ti)	MeCN/TEOA (5:1)	Visible light	HCOO [−]	32.4 16.3		[245]

Table 5. Cont.

Reaction Media	Light Source	Product	Product Formation Rate [$\mu\text{mol h}^{-1}\text{g}^{-1}$]	Comment	References
Ni _{0.87} Mg _{0.13} -MOF-74	MeCN/TEOA (5:1) [Ru(bpy ^c) ₃] Cl ₂ as photosensitizer	Visible light	HCOO [−] CO H ₂	540 520 2240	[20]
Ni _{0.75} Mg _{0.25} -MOF-74			HCOO [−] CO H ₂	640 460 2610	
Other form of MOF-based photocatalyst	Zn/PMOF	H ₂ O vapor	UV/Visible light	CH ₄ 8.7	[250]
UiO-67-Cp [*] Rh ^d (5,5'-dcbpy) Cl ₂ (10%)	MeCN/TEOA (5:1)	Visible light ($\lambda > 415$)	HCOO [−] H ₂	271 457	[249]
Al-PMOF embedded Cu ²⁺	H ₂ O/TEA (99:1)	Visible light	CH ₃ OH	262.6 (ppm h ^{−1} g ^{−1})	CO ₂ adsorbed chemically on the prepared photocatalyst, which led to bending the linear CO ₂ molecule, resulting in lower photoreduction barrier and subsequently improving the photocatalytic efficiency.
Al-PMOF				37.5 (ppm h ^{−1} g ^{−1})	
Co/PMOF	MeCN/TEOA (5:1)	Visible light	HCOO [−]	23.21	[220]

^a Product formation rate calculated by applying the mass of TiO₂ (g), ^b the weight percentage content of NH₂-UiO-66 in the semiconductor-NH₂-UiO-66(Zr) composite, ^c bpy = 2,2'-bipyridine, ^d Cp^{*} = pentamethylcyclopentadiene.

3.3. Potentials and Critical Research Challenges

Global warming and energy shortage are the main environmental concerns for humankind in the 21st century. Among all the renewable sources, solar energy is expected to tackle the energy demand, owing to its ubiquitous and cost-free nature. Therefore, among different methods that have been utilized for reducing CO₂ in the atmosphere, the photocatalytic conversion of CO₂ into valuable fuels and chemicals (e.g., CO, CH₄, CH₃OH, HCOOH) is considered as one of the most economical, sustainable, and environmentally friendly methods for ameliorating energy shortages and greenhouse effects.

In addition to applying clean and abundant solar energy, this process can be performed in almost mild conditions (room temperature and pressure) and also can directly convert CO₂ into short-chain hydrocarbons, which reduce the increasingly tense energy crisis. Nevertheless, there are several challenges that limit CO₂ photoreduction commercialization.

A major critical challenge is the low CO₂ solubility in water [29]. To overcome this drawback, different organic solvents such as methanol [261–264], isopropanol [265], and acetonitrile [220,225,226,266] have been used. Despite their higher CO₂ solubility and photoactivity, they are toxic, environmentally unfriendly, and not economic. Alternative solvents with high CO₂ solubility, low cost, and low environmental impact are required to advance CO₂ photoreduction.

A further challenge of water as a solvent is the kinetically favorable hydrogen evolution reaction (HER) [267]. This leads to severe competition between CO₂ reduction and HER from water, which is adsorbed in greater quantity onto the catalyst surfaces compared to CO₂.

Beyond limitations of CO₂, photocatalysis in general requires material improvement to improve efficiency. The efficiency limitations are mostly due to poor light-harvesting (large band-gap of material), low charge separation and transport (intrinsic properties of the semiconductor), and dependence on solar insolation. In this regard, findings in photocatalytic water splitting have recently shown a quantum efficiency of >95%. These improvements may be applied to driving CO₂ photoreduction [268]. These findings include aliovalent doping of the semiconductor to reduce recombination [269] and use of specific co-catalysts' systems to drive each reaction that occurs in water splitting without also catalyzing the reverse reaction [270].

Selectivity of reaction is vital considering CO₂ photoreduction may follow a series of pathways and is often in competition with HER. This is a particular challenge since the mechanisms and reaction pathways of CO₂ reduction on heterogeneous photocatalysts are still vague. Here, improvements in DFT calculations can assist in driving experimental design [271]. Porous materials and controlling adsorption of reactants appear to be the most promising strategies to controlling selectivity. Porous materials with active sites within the porous matrix can be used to drive a particular product, while also enhancing adsorption of reactant.

From a photocatalyst deactivation point of view, photocatalytic deactivation is observed after illumination for a long time. This phenomenon can be attributed to the (1) adsorption or accumulation of intermediate product/by-product on the active sites of photocatalyst and (2) desorption of produced hydrocarbons from photocatalyst surface not being complete. These two items can hinder the adsorption of CO₂ or H₂O on the surface of the photocatalyst and subsequently deactivate the CO₂ photoreduction efficiency after long-time irradiation. Therefore, more detailed studies are necessary about photocatalysts' deactivation in future works, which are crucial to have a deep and clear understanding of the reaction mechanisms.

4. Electrochemical Reduction of CO₂

Electrochemical CO₂ reduction is a promising method that has drawn widespread attention of researchers because it can be performed in ambient conditions and be driven by the electricity generated from renewable resources. Nonetheless, high energy demand for CO₂ reduction due to relatively low efficiency and the presence of competitive reactions

(e.g., hydrogen evolution reaction) are the main disadvantages of this process. Therefore, finding efficient electrocatalysts that decrease energy demand and suppress the competitive reaction have a crucial importance [59,272]. Metallic electrodes (e.g., Au, Pt, Cu, Ni, Ag) have been extensively utilized as electrocatalysts because of their excellent conductivity. However, low selectivity and a small surface area of the metal electrodes compared to other porous materials are drawbacks, preventing their development [273,274].

An ideal electrocatalyst is expected to have high stability (>20,000 h), selectivity ($\geq 90\%$), and current density ($>200 \text{ mA cm}^{-2}$) [275–277]. In this context, different metal-organic frameworks (MOFs) with various metal centers have been utilized for CO_2 electroreduction. That is because of the permanent porosity, large surface area, tunable structure, and abundant active sites of the MOFs [278–280]. Fe-based MOFs have been extensively applied as photocatalysts and for water splitting, utilized as electrocatalysts for CO_2 conversion [281,282]. Dong et al. [283] utilized Zr_6 , a clusters-based MOF of PCN-222(Fe), $[\text{Zr}_6\text{O}_8(\text{OH})_4(\text{H}_2\text{O})_4][\text{TCPP-Fe(III)-Cl}]_2$, which is built from Fe-TCPP, with the ligand as a catalyst. Notably, applying active porphyrin molecules into the MOFs' structure enhances effectively the active surface concentration, which leads to accelerating CO_2 reduction kinetics. Furthermore, carbon black was introduced into PCN-222(Fe) with a mass ratio 1:2 in order to improve the catalytic activity of Fe-based MOF (denoted as PCN-222(Fe)/C). The PCN-222(Fe)/C catalyst was loaded on carbon paper for CO_2 electrochemical reduction. The BET surface area of PCN-222(Fe) is high, about $2200 \text{ m}^2 \text{ g}^{-1}$, which provides a great number of available sites for CO_2 adsorption and fixation, resulting in the increment of surface CO_2 concentration. Moreover, after adsorption, CO_2 activation is obtained by bending the CO_2 molecule, which significantly decreased the activating energy of the CO_2 reduction process. The faradaic efficiency (this term defines the efficiency with which electrons transferred in a system facilitate the CO_2 electroreduction reaction) of CO (FE_{CO}) increased with increasing the applied overpotential and the maximum FE_{CO} (91%) obtained at -0.6 V vs. RHE with the overpotential of 494 mV in a CO_2 -saturated 0.5 M KHCO_3 electrolyte. Additionally, the FE_{CO} was over 80% even after 10 h, implying high catalyst stability at -0.6 V vs. RHE. Overall, the PCN-222(Fe)/C had a significant catalytic effect on the CO_2 electrochemical reduction because of integrating the intrinsic activity of the porphyrin molecule, including the intrinsic macrocyclic framework and tunable metal centers with the tunable oxidation state, with the high CO_2 adsorption ability because of the conserved porosity and the great conductivity of carbon black.

Cobalt shows different oxidation states, e.g., Co (II), Co (III), and Co (IV), such that it be used for the synthesis of various Co-based MOF a wide range of coordination geometries. For example, Wang et al. [284] synthesized different polyoxometalate-metallocporphyrin organic frameworks (PMOFs) by applying tetrakis [4-carboxyphenyl]-porphyrin-M (M-TCPP) as linkers. Notably, polyoxometalate-based MOFs have high structural robustness and chemical stability which is necessary for the durability test of the CO_2 reduction reaction. In addition, different transition metals were utilized (i.e., Co, Fe, Ni, and Zn) to prepare PMOFs as shown in Figure 24a. These materials were tested as electrocatalyst for CO_2 reduction in CO_2 -saturated 0.5 M KHCO_3 solution, Figure 24b. As shown in Figure 24b, FE_{CO} continuously increases with increasing the potential and the maximum value of 98.7% was obtained at -0.8 V . Furthermore, Co-PMOF selectively converts CO_2 into CO with the highest FE_{CO} (98.7%) compared to the other M-PMOFs (Fe-PMOF, 28.8%, Ni-PMOF, 18.5%, and Zn-PMOF, 1.2%, respectively). This result was explained by the fact that polyoxometalates and Co-porphyrin have synergistic effects in the CO_2 reduction reaction. Also, the desirable active site is the Co in Co-TCPP instead of POM. Actually, Co-PMOF can transfer charges more efficiently and have a larger active surface in the catalytic process compared to other investigated M-PMOFs. Consequently, Co-PMOF can provide more active sites in electrocatalyst to contact the electrolyte which can enhance the reaction speed of electroreduction of CO_2 .

Copper (Cu) is a promising catalyst candidate for CO_2 electroreduction due to its ability to produce hydrocarbons. Nonetheless, copper produces a variety of reaction

products and selectivity of each product is low. One solution to improve its selectivity is the dispersion and specifications of the reaction site and changing the concentration of protons, which are necessary for CO_2 electrochemical reduction [28,285,286]. In this regard, the copper-based MOF was utilized as electrocatalysts for CO_2 reduction for the first time in 2012 [287,288]. For this purpose, a Cu-rubeanate MOF (CR-MOF) was synthesized for the electrocatalytic reduction of CO_2 into HCOOH . For this purpose, the prepared CR-MOF was dropped on the CP to form a working electrode, and also 0.5 M KHCO_3 was prepared as an electrolyte. The amount of produced HCOOH was $13.4 \mu\text{mol cm}^{-2} \text{ h}^{-1}$, which was 13 times greater than that of a Cu metal electrode ($1.14 \mu\text{mol cm}^{-2} \text{ h}^{-1}$) at the potential of -1.2 V vs. SHE. Additionally, the selectivity of produced HCOOH by CR-MOF electrodes among the CO_2 products was more than 98%. The density of electrons on the metallic site of the CR-MOF was smaller than that on the Cu metal, which was the cause of the weak adsorption of CO_2 on the reaction site and high selectivity of HCOOH [288]. In another study [287], $\text{Cu}_3(\text{BTC})_2$ was applied as am electrocatalysts in 0.01 M N,N-dimethylformamide (DMF) containing tetrabutylammonium tetrafluoroborate (TBATFB) for CO_2 reduction. They demonstrated that the CO_2 -saturated solution influences the activity and selectivity of the CO_2 reduction in addition to the structure of the catalyst. The obtained results indicated that $\text{Cu}_3(\text{BTC})_2$ on the glassy carbon electrode significantly reduces CO_2 into oxalic acid with 90% purity and FE of 51%. According to the proposed reaction pathway, a carbon dioxide radical anion was formed during the reduction process and dimerized to form oxalate anion. Then, oxalate anion abstracted proton from a non-aqueous DMF solvent and the oxalic acid was formed. In summary, these results revealed that the solvent and electrolytes influence the reaction pathways, final products, and CO_2 adsorption capacity of electrocatalysts.

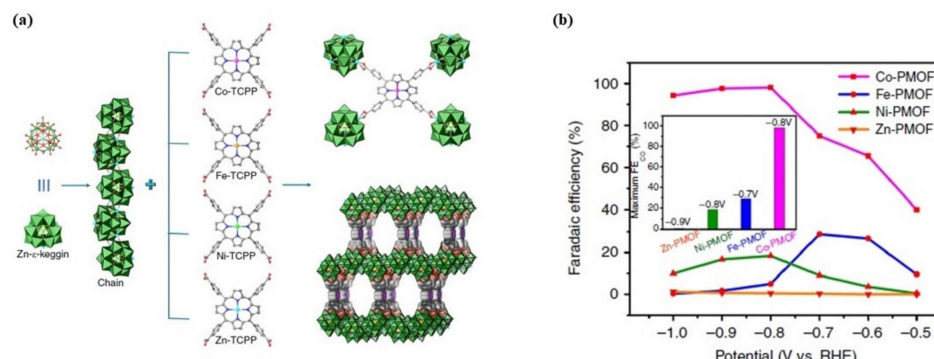


Figure 24. (a) Schematic of the structures of M-PMOFs (M = Co, Fe, Ni, Zn), (b) Faradaic efficiencies of M-PMOFs for CO [287].

Zn-based MOFs have drawn much interest due to their unique properties, which has led to various applications such as gas adsorption and separation, sensing, catalysis, and CO_2 capture [289]. On the other hand, ionic liquids (ILs) have unique properties such as nonvolatility, high chemical and thermal stability, high ionic conductivity, and a wide electrochemical window [290–292]. Electroreduction of CO_2 to CH_4 was investigated over deposited Zn-1,3,5-benzenetricarboxylic acid metal-organic frameworks (Zn-BTC MOFs) on carbon paper (CP) as cathodes by using ionic liquids (ILs) as the electrolytes. As shown in Figure 25a, the CH_4 production rate drastically enhanced at the potentials under -2.2 V vs. Ag/Ag^+ . Then, the rate of CH_4 production increased very slowly. Consequently, electrolysis less negative than -2.2 V vs. Ag/Ag^+ is more favorable for CH_4 production. According to the proposed mechanism in Figure 25b, first of all, the imidazolium cations were absorbed on the surface of the Zn-MOF. Afterward, CO_2 was captured by the adsorbed IL on the surface of the Zn-MOF, and a CO_2^{*-} intermediate was formed by taking one electron. Then, the CO_2^{*-} intermediate took another electron and generated CO. Because of the higher adsorption capacity of CO compared to CH_4 on the

Zn-MOF, CO prefers to reduce to CH₄ by taking six electrons instead of desorbing from the surface of the Zn-PMOF [293].

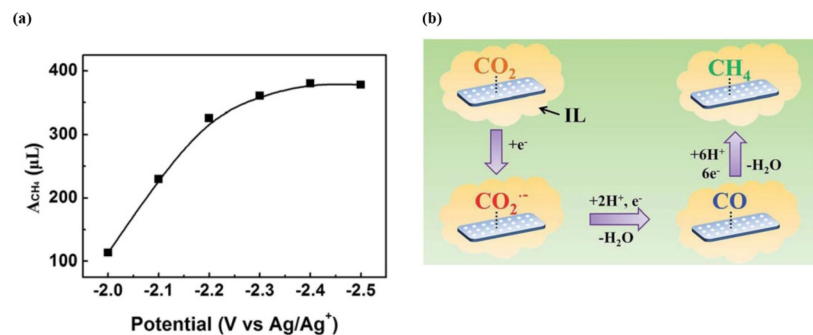


Figure 25. (a) The produced CH₄ (A_{CH_4} , volume at standard temperature and pressure) in 2 h as a function of potential, (b) the proposed reaction pathway for electroreduction of CO₂ to CH₄ on the Zn-MOF/CP cathode in ILs [293].

On the other hand, among zeolitic imidazolate frameworks (ZIFs), ZIF-8 has high CO₂ adsorption properties, e.g., a high surface area, well-ordered pores, a distinct morphology, and strong coordination between metal ions and ligands in the framework [294,295]. Wang et al. [295] investigated the effects of the counter anions and electrolyte on the CO₂ electrochemical reduction. For this purpose, different ZIFs with various zinc sources were synthesized and applied as an electrocatalyst for CO₂ reduction in an aqueous solution. Their experimental results showed that the synthesized ZIF-8 using ZnSO₄ had the best electroactivity towards CO₂ reduction with FE_{CO} of 65% at -1.8 V vs. Hg/Hg₂Cl₂ (SCE). The weaker interaction between SO₄²⁻ and Zn nodes was the main reason for the high activity and selectivity of ZIF-8^{SO4}. On the other hand, ZIF-8^{SO4} in 0.5 M NaCl electrolyte showed the highest FE compared to other electrolytes, NaHCO₃, NaClO₄, and NaHCO₃.

Noble metal-based MOFs showed high activity and selectivity in CO₂ electroreduction, but instability is their main disadvantage. For the first time, Ye et al. [296] incorporated a ReL(CO)₃Cl (L = 2,2'-bipyridine-5,5'-dicarboxylic acid) catalyst into highly oriented, surface-grafted MOF (SURMOF) thin films grown on a conductive fluorine-doped tin oxide (FTO) electrode by liquid-phase epitaxy. The Re-SURMOF-based electrode showed a significantly high faradaic efficiency of $93 \pm 5\%$ at -1.6 V vs. NHE for CO₂ electroreduction into CO, which is much more than other studied MOF thin film-based systems. The significant high faradic efficiency of Re-SURMOF is because of the excellent oriented structure of Re-SURMOF at the electrode surface compared to the other framework materials. The gaseous products were collected and analyzed via gas chromatography (GC). The main gaseous product was CO (40.5 μmol) with a small amount of H₂ (3.1 μmol). No other products were detected in both liquid and gas phases.

Ag is broadly utilized as an electrocatalyst for CO₂ reduction with CO as the main product. Many attempts have been devoted in order to improve the catalytic activity. Grafting of a catalyst on an electrode is one way to promote catalytic performance [289]. Another way to improve the CO faradaic efficiency over an Ag catalyst is applying MOFs. For this purpose, MOFs are decorated with a metal nanoparticle. In this respect, an Ag₂O/layered ZIF composite was synthesized by one-pot hydrothermal transformation of ZIF-7 nanoparticles (NPs) in an AgNO₃ aqueous solution. In this study, CO was the main product and H₂ was the byproduct. Furthermore, Ag₂O/layered ZIF showed the maximum catalytic performance at various potentials and the CO faradaic efficiency and current density were 80.5% and 26.2 mA cm⁻² at -1.2 V vs. the reversible hydrogen electrode (RHE), respectively. On the other hand, the CO faradaic efficiencies of ZIF-7, the layered ZIF, and the Ag/layered ZIF were 25, 61.6, and 54% at -1.2 V, respectively. The particle sizes of distributed Ag₂O NPs on the Ag₂O/layered ZIF were between 2 and 4 nm. On the other hand, the particle sizes of Ag NPs in the Ag/layered ZIF were between 4 and

30 nm with some particle aggregation. The BET surface areas of the Ag_2O /layered ZIF and Ag /layered ZIF were 25.5 and $10.9 \text{ m}^2\text{g}^{-1}$. Therefore, the small-sized Ag_2O NPs and the synergistic effect between the Ag_2O NPs and the layered ZIF with a high specific surface area greatly facilitated CO_2 mass transport, leading to a higher CO faradaic efficiency and partial current density for Ag_2O /layered ZIF compared to the other catalysts [297].

Among the large number of investigated MOFs for electrocatalytic CO_2 reduction, copper-based electrocatalysts have been found as promising, enabling the conversion of CO intermediate into multi-carbon product. However, the stability of Cu is not good for a long time and the required overpotential for CO_2 reduction at the Cu electrode is more than 1 V, particularly at the polycrystalline Cu electrode [298–300]. For instance, Zhao et al. [301] prepared oxide-derived Cu/carbon (OD Cu/C) catalysts via a facile carbonization of Cu-based MOF (HKUST-1) and utilized an electrocatalyst in 0.1 M KHCO_3 as the electrolyte. The results showed that the OD Cu/C selectively reduced CO_2 to methanol and ethanol with production rates of 5.1–12.4 and 3.7–13.4 $\text{mg L}^{-1}\text{h}^{-1}$, respectively, at potentials between -0.1 and -0.7 V vs. RHE, respectively. Moreover, in situ infrared reflectance (IR) spectroscopy and theoretical calculations implied that the CO_2^{*-} intermediate as a main intermediate during CO_2 electrochemical reduction was adsorbed on the surface of the OD Cu/C catalysts. The adsorbed CO_2^{*-} then reacted with another proton-electron pair and finally was reduced to the product of methanol. For ethanol production, C-C coupling took place between surface-bound C_1 oxygenates, accompanied by the formation of enol-like intermediates and then hydrogenation and dihydroxylation Figure 26.

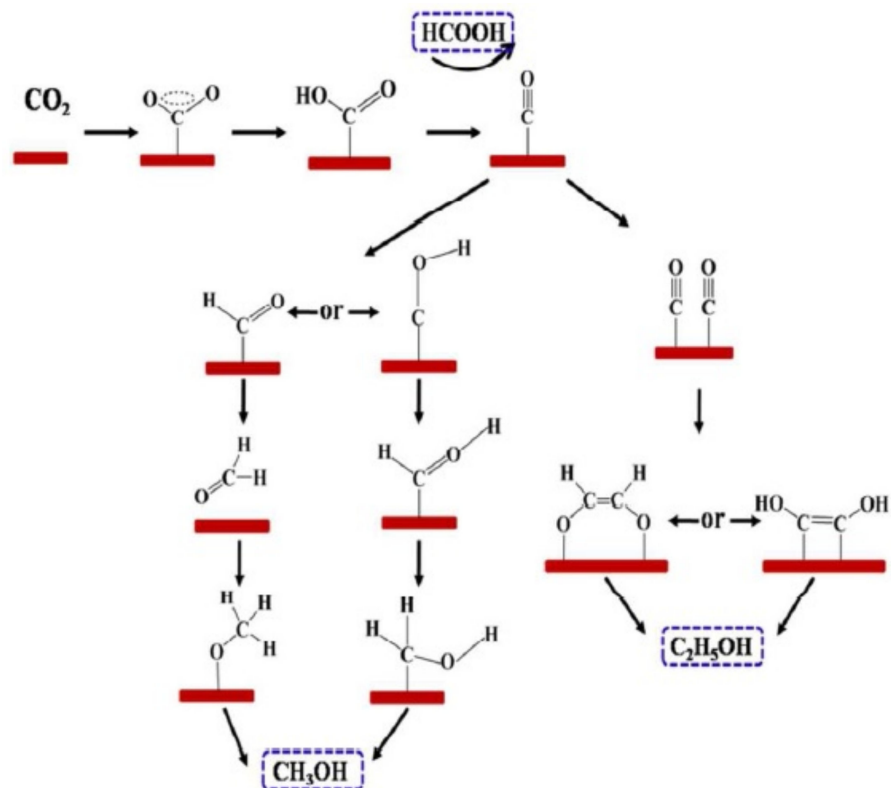


Figure 26. Proposed reaction pathways for electroconversion of CO_2 into alcohols on OD Cu/C-1000 [301].

Notably, the formation of hydrocarbons decreased with decreasing the Cu diameter below 5 nm due to the surface tendency to bind strongly with intermediates owing to d-band narrowing. Therefore, optimization of the surface topography and the size of Cu clusters to affect intermediate reaction pathways are interesting solutions to obtain high C₂ hydrocarbons' selectivity [302,303]. Therefore, a strategy was proposed to optimize the selectivity, activity, and efficiency for carbon dioxide reduction reaction. HKUST-1

($C_{18}H_6Cu_3O_{12}$, $Cu_3(btc)_2 \cdot xH_2O$, btc = benzene-1,3,5-tricarboxylate)-derived uncoordinated Cu sites enhanced the faradaic efficiency of C_2H_4 from 10 to 45% for calcinated HKUST-1 at 250 °C for 3 h with the lowest Cu-Cu coordination number (CN), which was greater than other MOF-derived Cu cluster catalysts. Moreover, H_2 production decreased to below 7%. The distortion of the Cu dimer in HKUST-1 applying the thermal treatment promoted the CO_2 photoreduction performance of Cu clusters, which was due to retaining a low Cu-Cu CN among the Cu clusters during the reaction. Generally, this study provides insight into the design and synthesis of potential electrocatalysts for CO_2 reduction to multi-carbon products [304]. Hwang et al. [305] synthesized a composite of $Cu_3(BTC)_2$ with graphene oxide sheets, denoted as Cu-MOF/GO. The prepared composite was utilized for CO_2 electroreduction in six different electrolyte systems, viz., $KHCO_3/H_2O$, tetrabutylammonium bromide (TBAB)/dimethylformamide (DMF), KBr/CH_3OH , CH_3COOK/CH_3OH , TBAB/ CH_3OH , and tetrabutylammonium perchlorate (TBAP)/ CH_3OH , to investigate their effect on product formation. According to the obtained results, the highest concentrations of $HCOOH$ as the main product for various electrolytes were 0.1404 mM (−0.1 V), 66.57 mM (−0.6 V), 0.2651 mM (−0.5 V), 0.2359 mM (−0.5 V), 0.7784 mM (−0.4 V), and 0.3050 mM (−0.45 V) in the various electrolytes, $KHCO_3/H_2O$, TBAB/DMF, KBr/CH_3OH , CH_3COOK/CH_3OH , TBAB/ CH_3OH , and TBAP/ CH_3OH , respectively. On the other hand, a significant Faradaic efficiency of 58% was achieved with 0.1 M TBAB/DMF electrolyte, which was about 1.5 times greater than that of Cu-MOF alone. Because of the significant conductivity of the graphene oxide and the basicity of Cu in MOF structures, which attracts the adhered gas molecules on the electrodes, the reduction process was promoted. As mentioned, the sizes of copper nanocrystals have a crucial role on the hydrocarbons' formation. Therefore, their sizes can be increased with increasing the pyrolysis temperatures, but the agglomeration of large metal atom clusters should be controlled at higher temperatures. With all these in mind, Rayer et al. [306] carbonized two commercial MOFs, HKUST-1 and PCN-62, at a temperature range of 400–800 °C and coated on the nickel and copper supports as inks. The prepared catalysts were used for CO_2 electroreduction in a conventional electrolytic cell with 0.05 M K_2CO_3 solution.

Table 6 summarizes the performance of the CO_2 reduction reaction (CO_2RR) catalysts and selectivity of the isopropanol formation over other carbon products ($FE_{isopropanol}/FE_{other}$). Even though both copper mesh and foil showed higher FE isopropanol than other tested catalysts, MOF-derived catalysts contained only small amounts of copper compared to the bulk metal, confirming that the high surface area of these prepared catalysts was significantly effective in CO_2RR . This is owing to the increment in the local pH at the catalytic surface, leading to the ethylene intermediates' formation, which improved propanol production. Additionally, Cu-HKUST-1 600 °C as a promising material among other prepared electrocatalysts indicated the highest selectivity of $FE_{isopropanol}/FE_{other}$ (2.7) with isopropanol as the main product (FE of 22.5%).

Table 6. The electrocatalytic performance of prepared catalysts for the CO_2 reduction reaction (CO_2RR) [306].

Electrocatalyst	FE_{CO2RR} (%)	$FE_{isopropanol}/FE_{other}$
Cu Mesh	43.3	1.5
Cu Foil	37.1	1.6
Cu-PCN62 800 °C	8.2	1.9
Cu-PCN62 600 °C	7.3	2
Ni-PCN62 800 °C	29.1	0.4
Cu-HKUST-1 600 °C	22.5	2.7
Ni-HKUST-1 600 °C	75.1	0.1
Ni-HKUST-1 400 °C	7.9	1.9

Single-atom catalysts typically enable high catalytic activity relative to their bulk counterparts due to their extraordinary electronic and geometric structures. In this context,

ZIF-8 assisted the generation of Ni single atoms distributed in nitrogen-doped porous carbon (Ni SAs/N-C) for efficient electroreduction of CO₂. The prepared catalyst showed an excellent Faradaic efficiency for CO production of 71.9% at a potential of −0.9 V, which was some 3-fold higher than that of Ni NPs/N-C. In addition, the obtained current density was 10.48 mA cm^{−2} with an overpotential of 0.89 V. The prepared single-atom catalyst promoted electron and mass transfer due to both the high synergetic effect of the enhanced number of surface-active sites and the excellent electrical conductivity and lower adsorption energy of CO over single Ni sites. Besides, Ni SAs/N-C implied a lower interfacial charge transfer, so electrons can transfer faster from electrodes to CO₂, which leads to facilitating CO₂^{•−} intermediate formation [301]. In another study [307], bimetallic Co/Zn ZIFs were synthesized with three atomically dispersed Co catalysts with different Co-N numbers at 800, 900, and 1000 °C and denoted as Co-N₄, Co-N₃, and Co-N₂, respectively. The electro-reaction was performed in a CO₂-saturated 0.5 M KHCO₃ solution as electrolyte. Among different applied catalysts, Co-N₂ showed the highest activity and selectivity, with the current density of about 18.1 mA cm^{−2} and the faradaic efficiency of 94% at an overpotential of 520 mV. Both experimental and theoretical calculations implied that the low coordination number promoted CO₂^{•−} intermediate formation and, therefore, increased electroactivity of CO₂ reduction. In other words, the first electron transfer can significantly affect the overall reduction process. In this context, Co-N₂ showed the lowest interfacial charge transfer, leading to electron transfer to CO₂ for CO₂^{•−} intermediate formation more rapidly. On the other hand, the potential for surface adsorption on Co-N₂ was more negative, which resulted in the stronger adsorption of CO₂^{•−} on Co-N₂. All these are beneficial for the CO₂ reduction reaction. Furthermore, iron-based, single-atom catalysts can also be obtained by pyrolysis of ZIF-8 as a template through confining the Fe precursor on the surface of the ZIF-8 to achieve numerous exposed active sites. For this purpose, ammonium ferric citrate (AFC) as the Fe precursor was applied to functionalize the surface of ZIF-8. The isolated single Fe atom catalysts were applied for CO₂ electroreduction in the KHCO₃ solution. In comparison to the Fe-based nanoparticles, the isolated single Fe atom showed high CO₂ reduction activity and selectivity. On the other hand, the results displayed that the performance of prepared catalysts was highly dependent on the synthesis method of single-atom catalysts. The isolated Fe-N sites on the surface of ZIF-8 provided more exposed active sites compared to the isolated iron species inside the cage of ZIF-8 [308]. Other recent studies have been summarized in Table 7. According to Table 7, the highest reported Faradaic Efficiency for CO can be achieved with Co-PP@CNT. In comparison to the traditional physical mixing method, chemically grafting cobalt porphyrins onto the surface of carbon nanotubes (CNT) can significantly increase the level of dispersion at the high loading of immobilized molecular catalysts. All these lead to stronger catalyst–substrate interaction and promotion of long-term stability and electron transfer to the intermediates. Therefore, a considerable performance for CO₂ electroreduction can be achieved by grafted Co-PP@CNT [309].

Co-PP@CNT: cobalt porphyrin was covalently grafted onto the surface of a carbon nanotube; CuBi12 (12% Bi): blending 79 wt.% HKUST-1 (Cu) with 21 wt.% CAU-17 (Bi); H-M-G: hemin and melamine molecules were synthesized through thermal pyrolysis on graphene for the fabrication of H-M-G; ZIF-A-LD: phenanthroline-doped ZIF-8, ZIF-7-A-LD: phenanthroline-doped ZIF-7; Ni@NC-900: Ni coordinated graphitic carbon shells; w-CCG/CoPc-A hybrid: washed cobalt (II) octaalkoxyphthalocyanine was immobilized on chemically converted graphene via π–π stacking; Cu₂O/Cu@NC-800 (carbonizing Cu_{btc} at 800 °C); Cu_{btc} (btc = benzene-1,3,5-tricarboxylate)-derived Cu₂O/Cu anchored in a nitrogen-doped porous carbon framework (Cu₂O/Cu@NC); PdAg_2 contains 61.9 wt% Pd and 38.1 wt% Ag; Ag₁–Cu_{1.1} NDs contains 52.4 wt% Cu.

Table 7. Summary of the recently studied electrocatalysts for CO₂ reduction reaction.

Electrocatalyst	Potential (V vs. RHE)	Electrolyte	Product	FE (%)	References
Co-PP@CNT	−0.49	0.5 M NaHCO ₃	CO	98.3	[309]
Cu-MOF-74 NPs	−1.3	0.1 M KHCO ₃	CH ₄	50	[310]
CuBi12	−0.21	0.5 M KHCO ₃	CH ₃ OH	8.6	[311]
			C ₂ H ₅ OH	28.3	
			alcohols	36.9	
H-M-G	−0.46	0.1 M KHCO ₃	CO	96.9	[312]
Ag ₁ –Cu _{1.1} NDs	−1.2	0.1 M KHCO ₃	C ₂ H ₃ O ₂ [−]	1.25	[313]
			(CH ₂ OH) ₂	0.34	
			C ₂ H ₅ OH	4.3	
			C ₃ H ₈ O	0.83	
ZIF-A-LD/CB	−1.1	0.1 M KHCO ₃	CO	90.57	[314]
ZIF-7-A-LD/CB				53.7	
Cu ₁₂ Sn ^a	−0.76	0.1 M KHCO ₃	CO	66.5	[315]
Cu ₄ Sn	−0.97		HCOO [−]	56.77	
Cu ₃ Sn ₂	−0.67		H ₂	50.33	
Sn-OH-5.9 branches	−1.6 V vs. Ag/AgCl	0.1 M KCl	HCOOH	82	[316]
			C1	93	
Ni@NC-900	−1	0.1 M KHCO ₃	CO	96	[317]
w-CCG/CoPc-A hybrid	−0.69	0.1 M KHCO ₃	H ₂	11.4	[318]
			CO	90.9	
	−0.79		H ₂	8.8	
			CO	91.5	
Cu ₂ O/Cu@NC-800	−6.8	0.1 M KHCO ₃	HCOO [−]	70.5	[16]
PdAg ₂	−0.27	0.1 M KHCO ₃	HCOO [−]	94	[319]
Sn-CHF (10 wt.%)	−0.78 ^b	0.1 M KHCO ₃	CO	8.91	[320]
	−0.98 ^b		HCOO [−]	0.88	
	−0.48 ^b		H ₂	87.72	
	−0.84 ^c		CO	48.36	
	−0.96 ^c		HCOO [−]	8.94	
	−0.32 ^c		H ₂	92.11	

^a Notably, the maximum obtained amount for each product is reported here. ^b CO₂ flow rate: 1 sccm, the maximum amount of detected products in the liquid phase. ^c CO₂ flow rate: 1 sccm, the maximum amount of detected products in the gas phase.

Potentials and Critical Research Challenges

As discussed above, the CO₂ electroreduction process has many advantages and immense environmental potential but there are still some practical challenges that require it to be improved before further development.

The main challenge of CO₂ electroreduction is the high energy requirement to activate a highly stable CO₂ molecule, which imposes more costs on this process. Impurities in the electrolytes and/or CO₂ feed gas and by-products resulting from corrosion of the electrolyzer components can poison catalysts. Therefore, the stability of the electrocatalyst, particularly under operating voltage/current conditions, is a challenge.

Similar to photocatalysis, the low solubility of CO₂ in water (~0.034 M [321]) is a tremendous challenge when utilizing aqueous electrolytes. A major research challenge is the solvent system for electrocatalytic CO₂ reduction that meets the demands of high CO₂ solubility, low cost, a wide electrochemical window, and low environmental impact.

Obtaining a high CO₂ selectivity to favorable products is yet another challenge to significantly reduce the complexity and costs of product separation processes. It is worth noting that achieving a high selectivity is also difficult owing to the different reactions of CO₂ and the competing hydrogen evolution reaction (HER), which all have almost the same standard potential. Of the possible products, CO and formic acid are the most profitable due to the greatest product value per electron, \$8000 and \$16,100/electron, respectively [322]. On the other hand, these products require little power, resulting in the reduction of the electricity cost and electrolyzer size. For formic acid, most of the cost is

related to the distillation step, which can be more cost effective by utilizing other industrial processes compared to the distillation. Therefore, the profitability of formic acid can be further improved. For instance, the operating and capital costs for formic acid separation are reduced to 50%, which gives a net present value of \$84,500,000 [322]. These are five important challenges for commercialization of this technology.

5. Conclusions

In this paper, the application of porous structures within CDR pathways such as solar thermochemical, photochemical, and electrochemical reduction technologies was reviewed. The porous materials, either entirely made from an active catalyst agent or being used as a catalyst support, will dramatically contribute to the enhancement of the reactions' kinetics through providing more available surface area for such surface-controlled reactions. Through summing up the results of the available research in literature, it was concluded that:

- The use of porous materials, made either entirely from or coated by the active reduction/oxidation materials, is a promising way to increase the conversion efficiency of solar to fuel in the solar thermochemical CDR cycle. The maximum reported solar-to-fuel efficiency is currently about 7.5%. Nevertheless, further research and development are needed to take the cyclic solar-to-fuel efficiency to about 20%, if the technology is to find a commercial use. This can be achieved through further optimization of both the porous materials' intrinsic properties, such as pore density, size, shape, tortuosity, etc., and the geometrical configuration of the reactive porous structures inside a solar receiver/reactor. Moreover, there is a need to decrease the temperature of the RedOx reactions to mitigate the parasitic heat losses, i.e., re-radiation and convective heat losses from the solar receiver/reactors through the reduction reaction step. In doing so, the porous structures need to be precisely pore-engineered both to efficiently absorb the thermal energy and to achieve a high conversion during RedOx cycles. The porous structures need to be also properly configured inside the solar reactor to proficiently trap and absorb the solar radiation, in case a directly irradiated reactor is employed.
- Since CO₂ solubility in water is very low and CO₂ adsorption and activation/excitation are more difficult than H₂O, finding a clean, non-toxic, and environmentally friendly solvent to increase CO₂ solubility/selectivity for the photocatalytic reduction process is still challenging.
- Finding solar-active and stable photocatalysts, enabling a high selectivity and conversion efficiency to completely suppress the competition reaction of water reduction to hydrogen, is also still challenging and requires a deeper understanding of the mechanisms and reaction pathways of the reduction of CO₂ on the heterogeneous photocatalysts within the porous structures.
- Development of a highly stable electrocatalyst for the long-term operation is challenging, while also the low solubility of CO₂ in water (~0.034 M) hinders reactions when aqueous electrolytes are employed. Additionally, obtaining a high CO₂ selectivity to favorable products is critical to reduce the costs and complexity of the down-stream process for the separation of products.
- There is a need to develop reactors facilitating the mass transfer from the gaseous CO₂ phase into the electrolyte and from the electrolyte into the active sites within the porous cathode catalysts.

Author Contributions: Conceptualization: A.M.P., N.S., A.R., M.J.; writing—original draft preparation: A.M.P., N.S., A.R.; writing—review and editing: M.J., C.J.S.; supervision: A.M.P., M.J.; visualization: A.M.P., N.S.; project administration: A.M.P. All authors have read and agreed to the published version of the manuscript.

Funding: This research received no external funding.

Institutional Review Board Statement: Not applicable.

Informed Consent Statement: Not applicable.

Acknowledgments: The authors would like to acknowledge the financial support of the ARENA IEP MI5 program. The valuable feedback on the original draft by the anonymous reviewers is also gratefully acknowledged.

Conflicts of Interest: The authors declare no conflict of interest.

Abbreviations

3DOM	Three-dimensionally ordered macroporous
AC	Activated carbon
AFC	Ammonium ferric citrate
ASU	Air separation unit
ATR	Auto-thermal reforming
bpy	Bipyridine
CB	Conduction band
CCD	Carbon dioxide dissociation
CDR	Carbon dioxide reutilization
CDS	Carbon dioxide splitting
CNNS	Carbon nitride nanosheets
Cp*	Pentamethylcyclopentadiene
CQD	Carbon quantum dots
CSP	Concentrated solar power
DMC	Dimethyl carbonate
DME	Di-methyl- ether
DMF	N,N-dimethylformamide
DMR	Dry-methane reforming
DMSO	Dimethyl sulfoxide
EGR	Enhanced gas recovery
EGS	Enhanced geothermal systems
EOR	Enhanced oil recovery
FE	Faradaic efficiencies
FT	Fischer-Tropsch
FTO	Fluorine-doped tin oxide
GC	Gas chromatography
GHG	Greenhouse gas
H ₂ ATA	2-aminoterephthalate acid
H ₂ DTA	2,5-diaminoterephthalic acid
HFSS	High flux solar simulator
IL	Ionic liquid
MeCN	Acetonitrile
MOF	Metal-organic framework
MPSZ	Magnesia partially stabilized zirconia
Mtonnes	Million tonnes
MWCNT	multi-walled carbon nanotubes
NHE	Normal hydrogen electrode
NOM	Nonordered macroporous

NPs	Nanoparticles
POX	Partial oxidation
RedOx	Reduction/oxidation
rGO	Reduced graphene oxide
RHE	Reversible hydrogen electrode
RPC	Reticulated porous ceramic
SDTR	Solar-driven thermochemical reactions
SMR	Steam methane reforming
SWCNT	Singe-walled carbon nanotubes
Syngas	Synthesis gas
TBAB	Tetrabutylammonium bromide
TBAP	Tetrabutylammonium perchlorate
TBATFB	Tetrabutylammonium tetrafluoroborate
TCPP	Tetrakis (4-carboxy phenyl) porphyrin
TEA	Triethylamine
TEOA	Triethanolamine
tpy	2,4,6-tris(4-pyridyl)pyridine
VB	Valence band
WS	Water splitting
ZIF	Zeolitic imidazolate framework

References

1. Figueroa, J.D.; Fout, T.; Plasynski, S.; McIlvried, H.; Srivastava, R.D. Advances in CO₂ capture technology—the us department of energy's carbon sequestration program. *Int. J. Greenh. Gas Control* **2008**, *2*, 9–20. [[CrossRef](#)]
2. Metz, B.; Davidson, O.; De Coninck, H. *Carbon Dioxide Capture and Storage: Special Report of the Intergovernmental Panel on Climate Change*; Cambridge University Press: Cambridge, UK, 2005.
3. He, F.; Han, T.; Hong, H.; Jin, H. Solar thermochemical hybrid trigeneration system with CO₂ capture using dimethyl ether-fueled chemical-looping combustion. In Proceedings of the ASME 2011 5th International Conference on Energy Sustainability, Washington, DC, USA, 7–10 August 2011; pp. 1651–1660.
4. IEA. *CO₂ Emissions from Fuel Combustion*; International Energy Agency: Paris, France, 2015.
5. ProOxygen. Atmospheric CO₂. Available online: <https://www.CO2.earth/> (accessed on 25 September 2021).
6. Rafiee, A.; Rajab Khalilpour, K.; Milani, D.; Panahi, M. Trends in CO₂ conversion and utilization: A review from process systems perspective. *J. Environ. Chem. Eng.* **2018**, *6*, 5771–5794. [[CrossRef](#)]
7. Jafarian, M.; Arjomandi, M.; Nathan, G.J. A hybrid solar chemical looping combustion system with a high solar share. *Appl. Energy* **2014**, *126*, 69–77. [[CrossRef](#)]
8. Zhao, L.; Oleson, K.; Bou-Zeid, E.; Krayenhoff, E.S.; Bray, A.; Zhu, Q.; Zheng, Z.; Chen, C.; Oppenheimer, M. Global multi-model projections of local urban climates. *Nat. Clim. Chang.* **2021**, *11*, 152–157. [[CrossRef](#)]
9. Huaman, R.N.E.; Jun, T.X. Energy related CO₂ emissions and the progress on ccs projects: A review. *Renew. Sustain. Energy Rev.* **2014**, *31*, 368–385. [[CrossRef](#)]
10. Adanez, J.; Abad, A.; Garcia-Labiano, F.; Gayan, P.; Luis, F. Progress in chemical-looping combustion and reforming technologies. *Prog. Energy Combust. Sci.* **2012**, *38*, 215–282. [[CrossRef](#)]
11. Yang, H.; Xu, Z.; Fan, M.; Gupta, R.; Slimane, R.B.; Bland, A.E.; Wright, I. Progress in carbon dioxide separation and capture: A review. *J. Environ. Sci.* **2008**, *20*, 14–27. [[CrossRef](#)]
12. Rafiee, A.; Khalilpour, K.R.; Milani, D. Chapter 8—CO₂ conversion and utilization pathways. In *Polygeneration with Polystorage for Chemical and Energy Hubs*; Khalilpour, K.R., Ed.; Academic Press: Cambridge, MA, USA, 2019; pp. 213–245.
13. Warsi, Y.; Kabanov, V.; Zhou, P.; Sinha, A. Novel carbon dioxide utilization technologies: A means to an end. *Front. Energy Res.* **2020**, *8*, 266. [[CrossRef](#)]
14. Haeussler, A.; Abanades, S.; Julbe, A.; Jouannaix, J.; Cartoixa, B. Two-step CO₂ and H₂O splitting using perovskite-coated ceria foam for enhanced green fuel production in a porous volumetric solar reactor. *J. CO₂ Util.* **2020**, *41*, 101257. [[CrossRef](#)]
15. Suter, S.; Steinfeld, A.; Haussener, S. Pore-level engineering of macroporous media for increased performance of solar-driven thermochemical fuel processing. *Int. J. Heat Mass Transf.* **2014**, *78*, 688–698. [[CrossRef](#)]
16. Li, D.; Liu, T.; Yan, Z.; Zhen, L.; Liu, J.; Wu, J.; Feng, Y. Mof-derived Cu₂O/Cu nanospheres anchored in nitrogen-doped hollow porous carbon framework for increasing the selectivity and activity of electrochemical CO₂-to-formate conversion. *ACS Appl. Mater. Interfaces* **2020**, *12*, 7030–7037. [[CrossRef](#)]
17. Arifin, D.; Aston, V.J.; Liang, X.; McDaniel, A.H.; Weimer, A.W. CoFe₂O₄ on a porous AL₂O₃ nanostructure for solar thermochemical CO₂ splitting. *Energy Environ. Sci.* **2012**, *5*, 9438–9443. [[CrossRef](#)]
18. Parvanian, A.M.; Salimjazi, H.; Shabaninejad, M.; Kreider, P.; Saadatfar, M. Ca/Al doped lanthanum manganite perovskite coated porous sic for CO₂ conversion. *Mater. Chem. Phys.* **2020**, *253*, 123306. [[CrossRef](#)]

19. Scheffe, J.R.; Steinfeld, A. Oxygen exchange materials for solar thermochemical splitting of H₂O and CO₂: A review. *Mater. Today* **2014**, *17*, 341–348. [\[CrossRef\]](#)
20. Guo, S.-H.; Qi, X.-J.; Zhou, H.-M.; Zhou, J.; Wang, X.-H.; Dong, M.; Zhao, X.; Sun, C.-Y.; Wang, X.-L.; Su, Z.-M. A bimetallic-mof catalyst for efficient CO₂ photoreduction from simulated flue gas to value-added formate. *J. Mater. Chem. A* **2020**, *8*, 11712–11718. [\[CrossRef\]](#)
21. Liu, Y.; Yang, Y.; Sun, Q.; Wang, Z.; Huang, B.; Dai, Y.; Qin, X.; Zhang, X. Chemical adsorption enhanced CO₂ capture and photoreduction over a copper porphyrin based metal organic framework. *ACS Appl. Mater. Interfaces* **2013**, *5*, 7654–7658. [\[CrossRef\]](#)
22. Cheng, X.; Zhang, J.; Tan, X.; Zheng, L.; Tan, D.; Liu, L.; Chen, G.; Wan, Q.; Zhang, B.; Zhang, F.; et al. Improved photocatalytic performance of metal–organic frameworks for CO₂ conversion by ligand modification. *Chem. Commun.* **2020**, *56*, 7637–7640. [\[CrossRef\]](#)
23. Loutzenhiser, P.G.; Meier, A.; Steinfeld, A. Review of the two-step H₂O/CO₂-splitting solar thermochemical cycle based on zn/zno redox reactions. *Materials* **2010**, *3*, 4922. [\[CrossRef\]](#)
24. Kovačič, Ž.; Likozar, B.; Huš, M. Photocatalytic CO₂ reduction: A review of ab initio mechanism, kinetics, and multiscale modeling simulations. *ACS Catal.* **2020**, *10*, 14984–15007. [\[CrossRef\]](#)
25. Shehzad, N.; Tahir, M.; Johari, K.; Murugesan, T.; Hussain, M. A critical review on TiO₂ based photocatalytic CO₂ reduction system: Strategies to improve efficiency. *J. CO₂ Util.* **2018**, *26*, 98–122. [\[CrossRef\]](#)
26. Ola, O.; Maroto-Valer, M.M. Review of material design and reactor engineering on TiO₂ photocatalysis for CO₂ reduction. *J. Photochem. Photobiol. C Photochem. Rev.* **2015**, *24*, 16–42. [\[CrossRef\]](#)
27. Low, J.; Cheng, B.; Yu, J. Surface modification and enhanced photocatalytic CO₂ reduction performance of TiO₂: A review. *Appl. Surf. Sci.* **2017**, *392*, 658–686. [\[CrossRef\]](#)
28. Gattrell, M.; Gupta, N.; Co, A. A review of the aqueous electrochemical reduction of CO₂ to hydrocarbons at copper. *J. Electroanal. Chem.* **2006**, *594*, 1–19. [\[CrossRef\]](#)
29. Li, K.; An, X.; Park, K.H.; Khraisheh, M.; Tang, J. A critical review of CO₂ photoconversion: Catalysts and reactors. *Catal. Today* **2014**, *224*, 3–12. [\[CrossRef\]](#)
30. Thompson, W.A.; Sanchez Fernandez, E.; Maroto-Valer, M.M. Review and analysis of CO₂ photoreduction kinetics. *ACS Sustain. Chem. Eng.* **2020**, *8*, 4677–4692. [\[CrossRef\]](#)
31. Luu, M.T.; Milani, D.; Bahadori, A.; Abbas, A. A comparative study of CO₂ utilization in methanol synthesis with various syngas production technologies. *J. CO₂ Util.* **2015**, *12*, 62–76. [\[CrossRef\]](#)
32. Milani, D.; Khalilpour, R.; Zahedi, G.; Abbas, A. A model-based analysis of CO₂ utilization in methanol synthesis plant. *J. CO₂ Util.* **2015**, *10*, 12–22. [\[CrossRef\]](#)
33. Luu, M.T.; Milani, D.; Sharma, M.; Zeaiter, J.; Abbas, A. Model-based analysis of CO₂ revalorization for di-methyl ether synthesis driven by solar catalytic reforming. *Appl. Energy* **2016**, *177*, 863–878. [\[CrossRef\]](#)
34. Rieks, M.; Bellinghausen, R.; Kockmann, N.; Mleczko, L. Experimental study of methane dry reforming in an electrically heated reactor. *Int. J. Hydrogen Energy* **2015**, *40*, 15940–15951. [\[CrossRef\]](#)
35. Aasberg-Petersen, K.; Christensen, T.S.; Dybkjaer, I.; Sehested, J.; Østberg, M.; Coertzen, R.M.; Keyser, M.J.; Steynberg, A.P. Chapter 4—synthesis gas production for ft synthesis. In *Studies in Surface Science and Catalysis*; Steynberg, A., Dry, M., Eds.; Elsevier: Amsterdam, The Netherlands, 2004; Volume 152, pp. 258–405.
36. Centi, G.; Quadrelli, E.A.; Perathoner, S. Catalysis for CO₂ conversion: A key technology for rapid introduction of renewable energy in the value chain of chemical industries. *Energy Environ. Sci.* **2013**, *6*, 1711–1731. [\[CrossRef\]](#)
37. Hillestad, M. Systematic staging in chemical reactor design. *Chem. Eng. Sci.* **2010**, *65*, 3301–3312. [\[CrossRef\]](#)
38. Anwar, M.N.; Fayyaz, A.; Sohail, N.F.; Khokhar, M.F.; Baqar, M.; Yasar, A.; Rasool, K.; Nazir, A.; Raja, M.U.F.; Rehan, M.; et al. CO₂ utilization: Turning greenhouse gas into fuels and valuable products. *J. Environ. Manag.* **2020**, *260*, 110059. [\[CrossRef\]](#)
39. Ateka, A.; Pérez-Uriarte, P.; Gamero, M.; Ereña, J.; Aguayo, A.T.; Bilbao, J. A comparative thermodynamic study on the CO₂ conversion in the synthesis of methanol and of dme. *Energy* **2017**, *120*, 796–804. [\[CrossRef\]](#)
40. Dieterich, V.; Buttler, A.; Hanel, A.; Spliethoff, H.; Fendt, S. Power-to-liquid via synthesis of methanol, dme or fischer-tropsch-fuels: A review. *Energy Environ. Sci.* **2020**, *13*, 3207–3252. [\[CrossRef\]](#)
41. Jadhav, S.G.; Vaidya, P.D.; Bhanage, B.M.; Joshi, J.B. Catalytic carbon dioxide hydrogenation to methanol: A review of recent studies. *Chem. Eng. Res. Des.* **2014**, *92*, 2557–2567. [\[CrossRef\]](#)
42. Park, N.; Park, M.-J.; Ha, K.-S.; Lee, Y.-J.; Jun, K.-W. Modeling and analysis of a methanol synthesis process using a mixed reforming reactor: Perspective on methanol production and CO₂ utilization. *Fuel* **2014**, *129*, 163–172. [\[CrossRef\]](#)
43. Rafiee, A. Staging of di-methyl-ether (dme) synthesis reactor from synthesis gas (syngas): Direct versus indirect route. *Chem. Eng. Res. Des.* **2020**, *163*, 157–168. [\[CrossRef\]](#)
44. Bonura, G.; Cannilla, C.; Frusteri, L.; Mezzapica, A.; Frusteri, F. Dme production by CO₂ hydrogenation: Key factors affecting the behaviour of cuznzr/ferrierite catalysts. *Catal. Today* **2017**, *281*, 337–344. [\[CrossRef\]](#)
45. Zhang, Y.; Li, D.; Zhang, S.; Wang, K.; Wu, J. CO₂ hydrogenation to dimethyl ether over cuo-zno-al2o3/hzsm-5 prepared by combustion route. *RSC Adv.* **2014**, *4*, 16391–16396. [\[CrossRef\]](#)
46. Ziae, M.; Panahi, M.; Fanaei, M.A.; Rafiee, A.; Khalilpour, K.R. Maximizing the profitability of integrated fischer-tropsch gtl process with ammonia and urea synthesis using response surface methodology. *J. CO₂ Util.* **2020**, *35*, 14–27. [\[CrossRef\]](#)

47. Otto, A.; Grube, T.; Schiebahn, S.; Stolten, D. Closing the loop: Captured CO₂ as a feedstock in the chemical industry. *Energy Environ. Sci.* **2015**, *8*, 3283–3297. [CrossRef]
48. Bose, A.; Jana, K.; Mitra, D.; De, S. Co-production of power and urea from coal with CO₂ capture: Performance assessment. *Clean Technol. Environ. Policy* **2015**, *17*, 1271–1280. [CrossRef]
49. Langanke, J.; Wolf, A.; Hofmann, J.; Bohm, K.; Subhani, M.A.; Muller, T.E.; Leitner, W.; Gurtler, C. Carbon dioxide (CO₂) as sustainable feedstock for polyurethane production. *Green Chem.* **2014**, *16*, 1865–1870. [CrossRef]
50. Zarandi, M.; Panahi, M.; Rafiee, A. Simulation of a natural gas-to-liquid process with a multitubular fischer–tropsch reactor and variable chain growth factor for product distribution. *Ind. Eng. Chem. Res.* **2020**, *59*, 19322–19333. [CrossRef]
51. Panzone, C.; Philippe, R.; Chappaz, A.; Fongarland, P.; Bengaouer, A. Power-to-liquid catalytic CO₂ valorization into fuels and chemicals: Focus on the fischer-tropsch route. *J. CO₂ Util.* **2020**, *38*, 314–347. [CrossRef]
52. Dimitriou, I.; Garcia-Gutierrez, P.; Elder, R.H.; Cuellar-Franca, R.M.; Azapagic, A.; Allen, R.W.K. Carbon dioxide utilisation for production of transport fuels: Process and economic analysis. *Energy Environ. Sci.* **2015**, *8*, 1775–1789. [CrossRef]
53. Agrafiotis, C.; Roeb, M.; Sattler, C. A review on solar thermal syngas production via redox pair-based water/carbon dioxide splitting thermochemical cycles. *Renew. Sustain. Energy Rev.* **2015**, *42*, 254–285. [CrossRef]
54. Yadav, D.; Banerjee, R. A review of solar thermochemical processes. *Renew. Sustain. Energy Rev.* **2016**, *54*, 497–532. [CrossRef]
55. Yuan, L.; Xu, Y.-J. Photocatalytic conversion of CO₂ into value-added and renewable fuels. *Appl. Surf. Sci.* **2015**, *342*, 154–167. [CrossRef]
56. Karamian, E.; Sharifnia, S. On the general mechanism of photocatalytic reduction of CO₂. *J. CO₂ Util.* **2016**, *16*, 194–203. [CrossRef]
57. Xu, D.; Dong, L.; Ren, J. Chapter 2—introduction of hydrogen routines. In *Hydrogen Economy*; Scipioni, A., Manzardo, A., Ren, J., Eds.; Academic Press: Cambridge, MA, USA, 2017; pp. 35–54.
58. Laursen, S.; Poudyal, S. Chapter 8—photo- and electro-catalysis: CO₂ mitigation technologies. In *Novel Materials for Carbon Dioxide Mitigation Technology*; Shi, F., Morreale, B., Eds.; Elsevier: Amsterdam, The Netherlands, 2015; pp. 233–268.
59. Al-Rowaili, F.N.; Jamal, A.; Ba Shammakh, M.S.; Rana, A. A review on recent advances for electrochemical reduction of carbon dioxide to methanol using metal–organic framework (mof) and non-mof catalysts: Challenges and future prospects. *ACS Sustain. Chem. Eng.* **2018**, *6*, 15895–15914. [CrossRef]
60. Duan, X.; Xu, J.; Wei, Z.; Ma, J.; Guo, S.; Wang, S.; Liu, H.; Dou, S. Metal-free carbon materials for CO₂ electrochemical reduction. *Adv. Mater.* **2017**, *29*, 1701784. [CrossRef]
61. Rackley, S.A. 22—CO₂ utilization and other sequestration options. In *Carbon Capture and Storage*, 2nd ed.; Rackley, S.A., Ed.; Butterworth-Heinemann: Boston, MA, USA, 2017; pp. 577–591.
62. Steinfeld, A.; Weimer, A.W. Thermochemical production of fuels with concentrated solar energy. *Opt. Express* **2010**, *18*, A100–A111. [CrossRef]
63. Nathan, G.J.; Jafarian, M.; Dally, B.B.; Saw, W.L.; Ashman, P.J.; Hu, E.; Steinfeld, A. Solar thermal hybrids for combustion power plant: A growing opportunity. *Prog. Energy Combust. Sci.* **2018**, *64*, 4–28. [CrossRef]
64. Jafarian, M.; Arjomandi, M.; Nathan, G.J. Thermodynamic potential of molten copper oxide for high temperature solar energy storage and oxygen production. *Appl. Energy* **2017**, *201*, 69–83. [CrossRef]
65. Schunk, L.O.; Steinfeld, A. Kinetics of the thermal dissociation of zno exposed to concentrated solar irradiation using a solar-driven thermogravimeter in the 1800–2100 k range. *AIChE J.* **2009**, *55*, 1497–1504. [CrossRef]
66. Silakhorri, M.; Jafarian, M.; Arjomandi, M.; Nathan, G.J. The energetic performance of a liquid chemical looping cycle with solar thermal energy storage. *Energy* **2019**, *170*, 93–101. [CrossRef]
67. Takeshita, T.; Yamaji, K. Important roles of fischer–tropsch synfuels in the global energy future. *Energy Policy* **2008**, *36*, 2773–2784. [CrossRef]
68. Nathan, G.; Dally, B.; Alwahabi, Z.; Van Eyk, P.; Jafarian, M.; Ashman, P. Research challenges in combustion and gasification arising from emerging technologies employing directly irradiated concentrating solar thermal radiation. *Proc. Combust. Inst.* **2017**, *36*, 2055–2074. [CrossRef]
69. Steinfeld, A. Solar thermochemical production of hydrogen—A review. *Sol. Energy* **2005**, *78*, 603–615. [CrossRef]
70. Chueh, W.C.; Falter, C.; Abbott, M.; Scipio, D.; Furley, P.; Haile, S.M.; Steinfeld, A. High-flux solar-driven thermochemical dissociation of CO₂ and H₂O using nonstoichiometric ceria. *Science* **2010**, *330*, 1797–1801. [CrossRef] [PubMed]
71. Kim, J.; Henao, C.A.; Johnson, T.A.; Dedrick, D.E.; Miller, J.E.; Stechel, E.B.; Maravelias, C.T. Methanol production from CO₂ using solar-thermal energy: Process development and techno-economic analysis. *Energy Environ. Sci.* **2011**, *4*, 3122–3132. [CrossRef]
72. Kim, J.; Johnson, T.A.; Miller, J.E.; Stechel, E.B.; Maravelias, C.T. Fuel production from CO₂ using solar-thermal energy: System level analysis. *Energy Environ. Sci.* **2012**, *5*, 8417–8429. [CrossRef]
73. Haeussler, A.; Abanades, S.; Julbe, A.; Jouannaix, J.; Cartoixa, B. Solar thermochemical fuel production from H₂O and CO₂ splitting via two-step redox cycling of reticulated porous ceria structures integrated in a monolithic cavity-type reactor. *Energy* **2020**, *201*, 117649. [CrossRef]
74. Alxneit, I. Assessing the feasibility of separating a stoichiometric mixture of zinc vapor and oxygen by a fast quench—Model calculations. *Sol. Energy* **2008**, *82*, 959–964. [CrossRef]
75. Steinfeld, A.; Larson, C.; Palumbo, R.; Foley, M., III. Thermodynamic analysis of the co-production of zinc and synthesis gas using solar process heat. *Energy* **1996**, *21*, 205–222. [CrossRef]

76. Silakhori, M.; Jafarian, M.; Arjomandi, M.; Nathan, G.J. Comparing the thermodynamic potential of alternative liquid metal oxides for the storage of solar thermal energy. *Sol. Energy* **2017**, *157*, 251–258. [[CrossRef](#)]
77. Weidenkaff, A.; Steinfeld, A.; Wokaun, A.; Auer, P.; Eichler, B.; Reller, A. Direct solar thermal dissociation of zinc oxide: Condensation and crystallisation of zinc in the presence of oxygen. *Sol. Energy* **1999**, *65*, 59–69. [[CrossRef](#)]
78. Steinfeld, A. Solar hydrogen production via a two-step water-splitting thermochemical cycle based on zn/zno redox reactions. *Int. J. Hydrogen Energy* **2002**, *27*, 611–619. [[CrossRef](#)]
79. Schunk, L.O.; Haeberling, P.; Wepf, S.; Wuillemin, D.; Meier, A.; Steinfeld, A. A receiver-reactor for the solar thermal dissociation of zinc oxide. *J. Sol. Energy Eng.* **2008**, *130*, 021009. [[CrossRef](#)]
80. Fletcher, E.A. Solarthermal and solar quasi-electrolytic processing and separations: Zinc from zinc oxide as an example. *Ind. Eng. Chem. Res.* **1999**, *38*, 2275–2282. [[CrossRef](#)]
81. Stamatou, A.; Loutzenhiser, P.; Steinfeld, A. Solar syngas production via H_2O/CO_2 -splitting thermochemical cycles with Zn/ZnO and FeO/Fe₃O₄ redox reactions. *Chem. Mater.* **2010**, *22*, 851–859. [[CrossRef](#)]
82. Lee, K.L.; Jafarian, M.; Ghanadi, F.; Arjomandi, M.; Nathan, G.J. An investigation into the effect of aspect ratio on the heat loss from a solar cavity receiver. *Sol. Energy* **2017**, *149*, 20–31. [[CrossRef](#)]
83. Davis, D.; Jafarian, M.; Chinnici, A.; Saw, W.L.; Nathan, G.J. Thermal performance of vortex-based solar particle receivers for sensible heating. *Sol. Energy* **2019**, *177*, 163–177. [[CrossRef](#)]
84. Perkins, C.; Lichty, P.R.; Weimer, A.W. Thermal zno dissociation in a rapid aerosol reactor as part of a solar hydrogen production cycle. *Int. J. Hydrogen Energy* **2008**, *33*, 499–510. [[CrossRef](#)]
85. Abanades, S.; Charvin, P.; Lemont, F.; Flamant, G. Novel two-step SnO₂/sno water-splitting cycle for solar thermochemical production of hydrogen. *Int. J. Hydrogen Energy* **2008**, *33*, 6021–6030. [[CrossRef](#)]
86. Charvin, P.; Abanades, S.; Lemont, F.; Flamant, G. Experimental study of SnO₂/SnO/Sn thermochemical systems for solar production of hydrogen. *AIChE J.* **2008**, *54*, 2759–2767. [[CrossRef](#)]
87. Le Gal, A.; Abanades, S. Dopant incorporation in ceria for enhanced water-splitting activity during solar thermochemical hydrogen generation. *J. Phys. Chem. C* **2012**, *116*, 13516–13523. [[CrossRef](#)]
88. Levèque, G.; Abanades, S.; Jumas, J.-C.; Olivier-Fourcade, J. Characterization of two-step tin-based redox system for thermochemical fuel production from solar-driven CO₂ and H₂O splitting cycle. *Ind. Eng. Chem. Res.* **2014**, *53*, 5668–5677. [[CrossRef](#)]
89. Ketteler, G.; Weiss, W.; Ranke, W.; Schlögl, R. Bulk and surface phases of iron oxides in an oxygen and water atmosphere at low pressure. *Phys. Chem. Chem. Phys.* **2001**, *3*, 1114–1122. [[CrossRef](#)]
90. Jafarian, M.; Arjomandi, M.; Nathan, G.J. Thermodynamic potential of high temperature chemical looping combustion with molten iron oxide as the oxygen carrier. *Chem. Eng. Res. Des.* **2017**, *120*, 69–81. [[CrossRef](#)]
91. Jafarian, M.; Arjomandi, M.; Nathan, G.J. Influence of the type of oxygen carriers on the performance of a hybrid solar chemical looping combustion system. *Energy Fuels* **2014**, *28*, 2914–2924. [[CrossRef](#)]
92. Tofighi, A.; Sibieude, F. Note on the condensation of the vapor phase above a melt of iron oxide in a solar parabolic concentrator. *Int. J. Hydrogen Energy* **1980**, *5*, 375–381. [[CrossRef](#)]
93. Sibieude, F.; Ducaroir, M.; Tofighi, A.; Ambriz, J. High temperature experiments with a solar furnace: The decomposition of Fe₃O₄, Mn₃O₄, CdO. *Int. J. Hydrogen Energy* **1982**, *7*, 79–88. [[CrossRef](#)]
94. Tofighi, A.; Sibieude, F. Dissociation of magnetite in a solar furnace for hydrogen-production—Tentative production evaluation of a 1000 kw concentrator from small-scale (2 kw) experimental results. *Int. J. Hydrogen Energy* **1984**, *9*, 293–296. [[CrossRef](#)]
95. Haseli, P.; Jafarian, M.; Nathan, G.J. High temperature solar thermochemical process for production of stored energy and oxygen based on CuO/Cu₂O redox reactions. *Sol. Energy* **2017**, *153*, 1–10. [[CrossRef](#)]
96. Allen, K.M.; Klausner, J.F.; Coker, E.N.; AuYeung, N.; Mishra, R. Synthesis and analysis of cobalt ferrite in ysz for use as reactive material in solar thermochemical water and carbon dioxide splitting. In Proceedings of the ASME 2013 7th International Conference on Energy Sustainability collocated with the ASME 2013 Heat Transfer Summer Conference and the ASME 2013 11th International Conference on Fuel Cell Science, Engineering and Technology, Minneapolis, MN, USA, 14–19 July 2013.
97. Gokon, N.; Murayama, H.; Nagasaki, A.; Kodama, T. Thermochemical two-step water splitting cycles by monoclinic zro₂-supported nife₂o₄ and fe₃o₄ powders and ceramic foam devices. *Sol. Energy* **2009**, *83*, 527–537. [[CrossRef](#)]
98. Coker, E.N.; Ambrosini, A.; Rodriguez, M.A.; Miller, J.E. Ferrite-ysz composites for solar thermochemical production of synthetic fuels: In operando characterization of CO₂ reduction. *J. Mater. Chem.* **2011**, *21*, 10767–10776. [[CrossRef](#)]
99. Coker, E.N.; Ambrosini, A.; Miller, J.E. Compositional and operational impacts on the thermochemical reduction of CO₂ to co by iron oxide/yttria-stabilized zirconia. *RSC Adv.* **2021**, *11*, 1493–1502. [[CrossRef](#)]
100. Scheffe, J.R.; Li, J.; Weimer, A.W. A spinel ferrite/hercynite water-splitting redox cycle. *Int. J. Hydrogen Energy* **2010**, *35*, 3333–3340. [[CrossRef](#)]
101. Kaneko, H.; Yokoyama, T.; Fuse, A.; Ishihara, H.; Hasegawa, N.; Tamaura, Y. Synthesis of new ferrite, Al–Cu ferrite, and its oxygen deficiency for solar H₂ generation from H₂O. *Int. J. Hydrogen Energy* **2006**, *31*, 2256–2265. [[CrossRef](#)]
102. Lougou, B.G.; Shuai, Y.; Zhang, H.; Ahouannou, C.; Zhao, J.; Kounouhewa, B.B.; Tan, H. Thermochemical CO₂ reduction over nife₂o₄@ alumina filled reactor heated by high-flux solar simulator. *Energy* **2020**, *197*, 117267. [[CrossRef](#)]
103. Millican, S.L.; Androshchuk, I.; Tran, J.T.; Trottier, R.M.; Bayon, A.; Al Salik, Y.; Idriss, H.; Musgrave, C.B.; Weimer, A.W. Oxidation kinetics of hercynite spinels for solar thermochemical fuel production. *Chem. Eng. J.* **2020**, *401*, 126015. [[CrossRef](#)]
104. Otsuka, K.; Hatano, M.; Morikawa, A. Hydrogen from water by reduced cerium oxide. *J. Catal.* **1983**, *79*, 493–496. [[CrossRef](#)]

105. Otsuka, K.; Hatano, M.; Morikawa, A. Decomposition of water by cerium oxide of δ -phase. *Inorg. Chim. Acta* **1985**, *109*, 193–197. [[CrossRef](#)]
106. Abanades, S.; Flamant, G. Thermochemical hydrogen production from a two-step solar-driven water-splitting cycle based on cerium oxides. *Sol. Energy* **2006**, *80*, 1611–1623. [[CrossRef](#)]
107. Chueh, W.C.; Haile, S.M. Ceria as a thermochemical reaction medium for selectively generating syngas or methane from H_2O and CO_2 . *ChemSusChem* **2009**, *2*, 735–739. [[CrossRef](#)]
108. Abanades, S.; Legal, A.; Cordier, A.; Peraudeau, G.; Flamant, G.; Julbe, A. Investigation of reactive cerium-based oxides for H_2 production by thermochemical two-step water-splitting. *J. Mater. Sci.* **2010**, *45*, 4163–4173. [[CrossRef](#)]
109. Chueh, W.C.; Haile, S.M. A thermochemical study of ceria: Exploiting an old material for new modes of energy conversion and CO_2 mitigation. *Philos. Trans. R. Soc. A* **2010**, *368*, 3269–3294. [[CrossRef](#)]
110. Meng, Q.L.; Lee, C.I.; Ishihara, T.; Kaneko, H.; Tamaura, Y. Reactivity of ceo(2)-based ceramics for solar hydrogen production via a two-step water-splitting cycle with concentrated solar energy. *Int. J. Hydrogen Energy* **2011**, *36*, 13435–13441. [[CrossRef](#)]
111. Scheffe, J.R.; Steinfeld, A. Thermodynamic analysis of cerium-based oxides for solar thermochemical fuel production. *Energy Fuels* **2012**, *26*, 1928–1936. [[CrossRef](#)]
112. Jang, J.T.; Yoon, K.J.; Han, G.Y. Methane reforming and water splitting using zirconia-supported cerium oxide in a volumetric receiver-reactor with different types of foam devices. *Sol. Energy* **2014**, *101*, 29–39. [[CrossRef](#)]
113. Venstrom, L.J.; Petkovich, N.; Rudisill, S.; Stein, A.; Davidson, J.H. The effects of morphology on the oxidation of ceria by water and carbon dioxide. *J. Sol. Energy Eng.* **2011**, *134*, 011005. [[CrossRef](#)]
114. Furler, P.; Scheffe, J.; Gorbar, M.; Moes, L.; Vogt, U.; Steinfeld, A. Solar thermochemical CO_2 splitting utilizing a reticulated porous ceria redox system. *Energy Fuels* **2012**, *26*, 7051–7059. [[CrossRef](#)]
115. Le Gal, A.; Abanades, S.; Bion, N.; Le Mercier, T.; Harlé, V. Reactivity of doped ceria-based mixed oxides for solar thermochemical hydrogen generation via two-step water-splitting cycles. *Energy Fuels* **2013**, *27*, 6068–6078. [[CrossRef](#)]
116. Call, F.; Roeb, M.; Schmücker, M.; Bru, H.; Curulla-Ferre, D.; Sattler, C.; Pitz-Paal, R. Thermogravimetric analysis of zirconia-doped ceria for thermochemical production of solar fuel. *Am. J. Anal. Chem.* **2013**, *4*, 37. [[CrossRef](#)]
117. Bader, R.; Venstrom, L.J.; Davidson, J.H.; Lipiński, W. Thermodynamic analysis of isothermal redox cycling of ceria for solar fuel production. *Energy Fuels* **2013**, *27*, 5533–5544. [[CrossRef](#)]
118. Furler, P.; Scheffe, J.; Marxer, D.; Gorbar, M.; Bonk, A.; Vogt, U.; Steinfeld, A. Thermochemical CO_2 splitting via redox cycling of ceria reticulated foam structures with dual-scale porosities. *Phys. Chem. Chem. Phys.* **2014**, *16*, 10503–10511. [[CrossRef](#)]
119. Jang, J.T.; Yoon, K.J.; Bae, J.W.; Han, G.Y. Cyclic production of syngas and hydrogen through methane-reforming and water-splitting by using ceria-zirconia solid solutions in a solar volumetric receiver-reactor. *Sol. Energy* **2014**, *109*, 70–81. [[CrossRef](#)]
120. Call, F.; Roeb, M.; Schmücker, M.; Sattler, C.; Pitz-Paal, R. Ceria doped with zirconium and lanthanide oxides to enhance solar thermochemical production of fuels. *J. Phys. Chem. C* **2015**, *119*, 6929–6938. [[CrossRef](#)]
121. Muhich, C.L.; Evanko, B.W.; Weston, K.C.; Lichty, P.; Liang, X.; Martinek, J.; Musgrave, C.B.; Weimer, A.W. Efficient generation of h_2 by splitting water with an isothermal redox cycle. *Science* **2013**, *341*, 540. [[CrossRef](#)] [[PubMed](#)]
122. Bhosale, R.R. Thermodynamic efficiency analysis of zinc oxide based solar driven thermochemical H_2O splitting cycle: Effect of partial pressure of O_2 , thermal reduction and H_2O splitting temperatures. *Int. J. Hydrogen Energy* **2018**, *43*, 14915–14924. [[CrossRef](#)]
123. Bhosale, R.R.; Takalkar, G.; Sutar, P.; Kumar, A.; AlMomani, F.; Khraisheh, M. A decade of ceria based solar thermochemical H_2O/CO_2 splitting cycle. *Int. J. Hydrogen Energy* **2019**, *44*, 34–60. [[CrossRef](#)]
124. Bhosale, R.R.; Kumar, A.; AlMomani, F.; Ghosh, U.; Al-Muhtaseb, S.; Gupta, R.; Alxneit, I. Assessment of $Ce_xZr_yHf_zO_2$ based oxides as potential solar thermochemical CO_2 splitting materials. *Ceram. Int.* **2016**, *42*, 9354–9362. [[CrossRef](#)]
125. Lee, K.L.; Chinnici, A.; Jafarian, M.; Arjomandi, M.; Dally, B.; Nathan, G. The influence of wind speed, aperture ratio and tilt angle on the heat losses from a finely controlled heated cavity for a solar receiver. *Renew. Energy* **2019**, *143*, 1544–1553. [[CrossRef](#)]
126. Lee, K.L.; Chinnici, A.; Jafarian, M.; Arjomandi, M.; Dally, B.; Nathan, G. The influence of wall temperature distribution on the mixed convective losses from a heated cavity. *Appl. Therm. Eng.* **2019**, *155*, 157–165. [[CrossRef](#)]
127. Miller, J.E.; Allendorf, M.D.; Diver, R.B.; Evans, L.R.; Siegel, N.P.; Stuecker, J.N. Metal oxide composites and structures for ultra-high temperature solar thermochemical cycles. *J. Mater. Sci.* **2008**, *43*, 4714–4728. [[CrossRef](#)]
128. Scheffe, J.R.; Weibel, D.; Steinfeld, A. Lanthanum–strontium–manganese perovskites as redox materials for solar thermochemical splitting of H_2O and CO_2 . *Energy Fuels* **2013**, *27*, 4250–4257. [[CrossRef](#)]
129. McDaniel, A.H.; Miller, E.C.; Arifin, D.; Ambrosini, A.; Coker, E.N.; O’Hayre, R.; Chueh, W.C.; Tong, J. Sr- and mn-doped $LaAlO_{3-\delta}$ for solar thermochemical H_2 and co production. *Energy Environ. Sci.* **2013**, *6*, 2424–2428. [[CrossRef](#)]
130. Nalbandian, L.; Evdou, A.; Zaspalis, V. $La(1-x)Sr(x)Mo(3)$ ($m = mn, fe$) perovskites as materials for thermochemical hydrogen production in conventional and membrane reactors. *Int. J. Hydrogen Energy* **2009**, *34*, 7162–7172. [[CrossRef](#)]
131. McDaniel, A.H.; Ambrosini, A.; Coker, E.N.; Miller, J.E.; Chueh, W.C.; O’Hayre, R.; Tong, J. Nonstoichiometric perovskite oxides for solar thermochemical H_2 and co production. *Energy Procedia* **2014**, *49*, 2009–2018. [[CrossRef](#)]
132. Demont, A.; Abanades, S. Solar thermochemical conversion of CO_2 into fuel via two-step redox cycling of non-stoichiometric mn-containing perovskite oxides. *J. Mater. Chem. A* **2015**, *3*, 3536–3546. [[CrossRef](#)]
133. Bork, A.H.; Kubicek, M.; Struzik, M.; Rupp, J.L.M. Perovskite $La_{0.6}Sr_{0.4}Cr_{1-x}Co_xO_{3-\delta}$ solid solutions for solar-thermochemical fuel production: Strategies to lower the operation temperature. *J. Mater. Chem. A* **2015**, *3*, 15546–15557. [[CrossRef](#)]

134. Cooper, T.; Scheffe, J.R.; Galvez, M.E.; Jacot, R.; Patzke, G.; Steinfeld, A. Lanthanum manganite perovskites with ca/sr a-site and al b-site doping as effective oxygen exchange materials for solar thermochemical fuel production. *Energy Technol. Ger.* **2015**, *3*, 1130–1142. [[CrossRef](#)]
135. Takacs, M.; Hoes, M.; Caduff, M.; Cooper, T.; Scheffe, J.R.; Steinfeld, A. Oxygen nonstoichiometry, defect equilibria, and thermodynamic characterization of lamno₃ perovskites with ca/sr a-site and al b-site doping. *Acta Mater.* **2016**, *103*, 700–710. [[CrossRef](#)]
136. Parvanian, A.M.; Salimjazi, H.; Shabariejad, M.; Troitzsch, U.; Kreider, P.; Lipiński, W.; Saadatfar, M. Thermochemical CO₂ splitting performance of perovskite coated porous ceramics. *RSC Adv.* **2020**, *10*, 23049–23057. [[CrossRef](#)]
137. Gokon, N.; Hasegawa, T.; Takahashi, S.; Kodama, T. Thermochemical two-step water-splitting for hydrogen production using fe-ysz particles and a ceramic foam device. *Energy* **2008**, *33*, 1407–1416. [[CrossRef](#)]
138. Kawakami, S.; Myojin, T.; Cho, H.S.; Hatamachi, T.; Gokon, N.; Kodama, T. Thermochemical two-step water splitting cycle using ni-ferrite and CeO₂ coated ceramic foam devices by concentrated xe-light radiation. *Energy Procedia* **2014**, *49*, 1980–1989. [[CrossRef](#)]
139. Marxer, D.; Furler, P.; Takacs, M.; Steinfeld, A. Solar thermochemical splitting of CO₂ into separate streams of co and O₂ with high selectivity, stability, conversion, and efficiency. *Energy Environ. Sci.* **2017**, *10*, 1142–1149. [[CrossRef](#)]
140. Guene Lougou, B.; Shuai, Y.; Pan, R.; Chaffa, G.; Ahouannou, C.; Zhang, H.; Tan, H. Radiative heat transfer and thermal characteristics of fe-based oxides coated sic and alumina rpc structures as integrated solar thermochemical reactor. *Sci. China Technol. Sci.* **2018**, *61*, 1788–1801. [[CrossRef](#)]
141. Agrafiotis, C.; Roeb, M.; Konstandopoulos, A.G.; Nalbandian, L.; Zaspalis, V.T.; Sattler, C.; Stobbe, P.; Steele, A.M. Solar water splitting for hydrogen production with monolithic reactors. *Sol. Energy* **2005**, *79*, 409–421. [[CrossRef](#)]
142. Walker, L.S.; Miller, J.E.; Hilmas, G.E.; Evans, L.R.; Corral, E.L. Coextrusion of zirconia–iron oxide honeycomb substrates for solar-based thermochemical generation of carbon monoxide for renewable fuels. *Energy Fuels* **2012**, *26*, 712–721. [[CrossRef](#)]
143. Gokon, N.; Kodama, T.; Imaizumi, N.; Umeda, J.; Seo, T. Ferrite/zirconia-coated foam device prepared by spin coating for solar demonstration of thermochemical water-splitting. *Int. J. Hydrogen Energy* **2011**, *36*, 2014–2028. [[CrossRef](#)]
144. Rouquerol, J.; Avnir, D.; Fairbridge, C.W.; Everett, D.H.; Haynes, J.M.; Pernicone, N.; Ramsay, J.D.F.; Sing, K.S.W.; Unger, K.K. Recommendations for the characterization of porous solids (technical report). *Pure Appl. Chem.* **1994**, *66*, 1739–1758. [[CrossRef](#)]
145. Levy, M.; Rubin, R.; Rosin, H.; Levitan, R. Methane reforming by direct solar irradiation of the catalyst. *Energy* **1992**, *17*, 749–756. [[CrossRef](#)]
146. Levy, M.; Rosin, H.; Levitan, R. Chemical reactions in a solar furnace by direct solar irradiation of the catalyst. *J. Sol. Energy Eng.* **1989**, *111*, 96–97. [[CrossRef](#)]
147. Roeb, M.; Sattler, C.; Klüser, R.; Monnerie, N.; de Oliveira, L.; Konstandopoulos, A.G.; Agrafiotis, C.; Zaspalis, V.T.; Nalbandian, L.; Steele, A.; et al. Solar hydrogen production by a two-step cycle based on mixed iron oxides. *J. Sol. Energy Eng.* **2005**, *128*, 125–133. [[CrossRef](#)]
148. Diver, R.B.; Miller, J.E.; Allendorf, M.D.; Siegel, N.P.; Hogan, R.E. Solar thermochemical water-splitting ferrite-cycle heat engines. *J. Sol. Energy Eng.* **2008**, *130*, 041001. [[CrossRef](#)]
149. Roeb, M.; Säck, J.P.; Rietbrock, P.; Prahl, C.; Schreiber, H.; Neises, M.; de Oliveira, L.; Graf, D.; Ebert, M.; Reinalter, W.; et al. Test operation of a 100 kw pilot plant for solar hydrogen production from water on a solar tower. *Sol. Energy* **2011**, *85*, 634–644. [[CrossRef](#)]
150. Furler, P.; Scheffe, J.R.; Steinfeld, A. Syngas production by simultaneous splitting of H₂O and CO₂ via ceria redox reactions in a high-temperature solar reactor. *Energy Environ. Sci.* **2012**, *5*, 6098–6103. [[CrossRef](#)]
151. Rudisill, S.G.; Venstrom, L.J.; Petkovich, N.D.; Quan, T.; Hein, N.; Boman, D.B.; Davidson, J.H.; Stein, A. Enhanced oxidation kinetics in thermochemical cycling of CeO₂ through templated porosity. *J. Phys. Chem. C* **2013**, *117*, 1692–1700. [[CrossRef](#)]
152. Rhodes, N.R.; Bobek, M.M.; Allen, K.M.; Hahn, D.W. Investigation of long term reactive stability of ceria for use in solar thermochemical cycles. *Energy* **2015**, *89*, 924–931. [[CrossRef](#)]
153. Marxer, D.; Furler, P.; Scheffe, J.; Geerlings, H.; Falter, C.; Batteiger, V.; Sizmann, A.; Steinfeld, A. Demonstration of the entire production chain to renewable kerosene via solar thermochemical splitting of H₂O and CO₂. *Energy Fuels* **2015**, *29*, 3241–3250. [[CrossRef](#)]
154. Chuayboon, S.; Abanades, S.; Rodat, S. Syngas production via solar-driven chemical looping methane reforming from redox cycling of ceria porous foam in a volumetric solar reactor. *Chem. Eng. J.* **2019**, *356*, 756–770. [[CrossRef](#)]
155. Luyten, J.; Cooymans, J.; Smolders, C.; Vercauteren, S.; Vansant, E.; Leysen, R. Shaping of multilayer ceramic membranes by dip coating. *J. Eur. Ceram. Soc.* **1997**, *17*, 273–279. [[CrossRef](#)]
156. Diver, R. Receiver/Reactor Concepts for Thermochemical Transport of Solar Energy. *ASME. J. Sol. Energy Eng.* **1987**, *109*, 199–204. [[CrossRef](#)]
157. Lee, K.L.; Chinnici, A.; Jafarian, M.; Arjomandi, M.; Dally, B.; Nathan, G. Experimental investigation of the effects of wind speed and yaw angle on heat losses from a heated cavity. *Sol. Energy* **2018**, *165*, 178–188. [[CrossRef](#)]
158. Yuan, C.; Jarrett, C.; Chueh, W.; Kawajiri, Y.; Henry, A. A new solar fuels reactor concept based on a liquid metal heat transfer fluid: Reactor design and efficiency estimation. *Sol. Energy* **2015**, *122*, 547–561. [[CrossRef](#)]
159. Jafarian, M.; Abdollahi, M.R.; Nathan, G.J. Preliminary evaluation of a novel solar bubble receiver for heating a gas. *Sol. Energy* **2019**, *182*, 264–277. [[CrossRef](#)]

160. Silakhori, M.; Jafarian, M.; Arjomandi, M.; Nathan, G.J. Experimental assessment of copper oxide for liquid chemical looping for thermal energy storage. *J. Energy Storage* **2019**, *21*, 216–221. [[CrossRef](#)]
161. Jafarian, M.; Chisti, Y.; Nathan, G.J. Gas-lift circulation of a liquid between two inter-connected bubble columns. *Chem. Eng. Sci.* **2020**, *218*, 115574. [[CrossRef](#)]
162. Jafarian, M.; Arjomandi, M.; Nathan, G.J. A hybrid solar and chemical looping combustion system for solar thermal energy storage. *Appl. Energy* **2013**, *103*, 671–678. [[CrossRef](#)]
163. Jafarian, M.; Arjomandi, M.; Nathan, G.J. The influence of high intensity solar radiation on the temperature and reduction of an oxygen carrier particle in hybrid chemical looping combustion. *Chem. Eng. Sci.* **2013**, *95*, 331–342. [[CrossRef](#)]
164. Romero, M.; Steinfeld, A. Concentrating solar thermal power and thermochemical fuels. *Energy Environ. Sci.* **2012**, *5*, 9234–9245. [[CrossRef](#)]
165. Lu, Z.; Jafarian, M.; Arjomandi, M.; Nathan, G.J. Analytical assessment of a novel rotating fluidized bed solar reactor for steam gasification of char particles. *Sol. Energy* **2016**, *140*, 113–123. [[CrossRef](#)]
166. Maag, G.; Lipiński, W.; Steinfeld, A. Particle–gas reacting flow under concentrated solar irradiation. *Int. J. Heat Mass Transf.* **2009**, *52*, 4997–5004. [[CrossRef](#)]
167. Z’Graggen, A.; Haueter, P.; Trommer, D.; Romero, M.; De Jesus, J.; Steinfeld, A. Hydrogen production by steam-gasification of petroleum coke using concentrated solar power—ii reactor design, testing, and modeling. *Int. J. Hydrogen Energy* **2006**, *31*, 797–811. [[CrossRef](#)]
168. Piatkowski, N.; Wieckert, C.; Steinfeld, A. Experimental investigation of a packed-bed solar reactor for the steam-gasification of carbonaceous feedstocks. *Fuel Process. Technol.* **2009**, *90*, 360–366. [[CrossRef](#)]
169. Amy, C.; Budenstein, D.; Bagepalli, M.; England, D.; DeAngelis, F.; Wilk, G.; Jarrett, C.; Kelsall, C.; Hirshey, J.; Wen, H.; et al. Pumping liquid metal at high temperatures up to 1,673 kelvin. *Nature* **2017**, *550*, 199–203. [[CrossRef](#)]
170. Long, S.; Lau, T.C.; Chinnici, A.; Nathan, G.J. The flow-field within a vortex-based solar cavity receiver with an open aperture. *Exp. Therm. Fluid Sci.* **2021**, *123*, 110314. [[CrossRef](#)]
171. Inoue, T.; Fujishima, A.; Konishi, S.; Honda, K. Photoelectrocatalytic reduction of carbon dioxide in aqueous suspensions of semiconductor powders. *Nature* **1979**, *277*, 637–638. [[CrossRef](#)]
172. Zhu, S.; Wang, D. Photocatalysis: Basic principles, diverse forms of implementations and emerging scientific opportunities. *Adv. Energy Mater.* **2017**, *7*, 1700841. [[CrossRef](#)]
173. Shtyka, O.; Ciesielski, R.; Kedziora, A.; Maniukiewicz, W.; Dubkov, S.; Gromov, D.; Maniecki, T. Photocatalytic reduction of CO₂ over me (Pt, Pd, Ni, Cu)/TiO₂ catalysts. *Top. Catal.* **2020**, *63*, 113–120. [[CrossRef](#)]
174. Jeffrey, C.S. 17—photocatalytic reduction of carbon dioxide (CO₂). In *Developments and Innovation in Carbon Dioxide (CO₂) Capture and Storage Technology*; Maroto-Valer, M.M., Ed.; Woodhead Publishing: Cambridge, UK, 2010; Volume 2, pp. 463–501.(CO₂). In *Developments and Innovation in Carbon Dioxide (CO₂) Capture and Storage Technology*; Maroto-Valer, M.M., Ed.; Woodhead Publishing: Cambridge, UK, 2010; Volume 2, pp. 463–501.
175. Abdullah, H.; Khan, M.M.R.; Ong, H.R.; Yaakob, Z. Modified TiO₂ photocatalyst for CO₂ photocatalytic reduction: An overview. *J. CO₂ Util.* **2017**, *22*, 15–32. [[CrossRef](#)]
176. Dong, H.; Zeng, G.; Tang, L.; Fan, C.; Zhang, C.; He, X.; He, Y. An overview on limitations of TiO₂-based particles for photocatalytic degradation of organic pollutants and the corresponding countermeasures. *Water Res.* **2015**, *79*, 128–146. [[CrossRef](#)]
177. Tasbihi, M.; Călin, I.; Šuligoj, A.; Fanetti, M.; Lavrenčić Štangar, U. Photocatalytic degradation of gaseous toluene by using TiO₂ nanoparticles immobilized on fiberglass cloth. *J. Photochem. Photobiol. A Chem.* **2017**, *336*, 89–97. [[CrossRef](#)]
178. Baloyi, J.; Seadira, T.; Raphulu, M.; Ochieng, A. Preparation, characterization and growth mechanism of dandelion-like TiO₂ nanostructures and their application in photocatalysis towards reduction of cr(vi). *Mater. Today Proc.* **2015**, *2*, 3973–3987. [[CrossRef](#)]
179. Tsang, C.H.A.; Li, K.; Zeng, Y.; Zhao, W.; Zhang, T.; Zhan, Y.; Xie, R.; Leung, D.Y.C.; Huang, H. Titanium oxide based photocatalytic materials development and their role of in the air pollutants degradation: Overview and forecast. *Environ. Int.* **2019**, *125*, 200–228. [[CrossRef](#)]
180. Liu, X.; Xing, Z.; Zhang, Y.; Li, Z.; Wu, X.; Tan, S.; Yu, X.; Zhu, Q.; Zhou, W. Fabrication of 3d flower-like black n-TiO₂-x@mos₂ for unprecedented-high visible-light-driven photocatalytic performance. *Appl. Catal. B Environ.* **2017**, *201*, 119–127. [[CrossRef](#)]
181. Carp, O.; Huisman, C.L.; Reller, A. Photoinduced reactivity of titanium dioxide. *Prog. Solid State Chem.* **2004**, *32*, 33–177. [[CrossRef](#)]
182. Tahir, M.; Amin, N.S. Indium-doped TiO₂ nanoparticles for photocatalytic CO₂ reduction with H₂O vapors to CH₄. *Appl. Catal. B Environ.* **2015**, *162*, 98–109. [[CrossRef](#)]
183. Dhakshinamoorthy, A.; Navalon, S.; Corma, A.; Garcia, H. Photocatalytic CO₂ reduction by TiO₂ and related titanium containing solids. *Energy Environ.* **2012**, *5*, 9217–9233. [[CrossRef](#)]
184. Liu, C.; Yu, T.; Tan, X.; Huang, X. Comparison n-cu-codoped nanotitania and n-doped nanotitania in photocatalytic reduction of CO₂ under uv light. *Inorg. Nano Met. Chem.* **2017**, *47*, 9–14. [[CrossRef](#)]
185. Zaleska, A. Doped-TiO₂: A review. *Recent Pat. Eng.* **2008**, *2*, 157–164. [[CrossRef](#)]
186. Nematollahi, R.; Ghotbi, C.; Khorasheh, F.; Larimi, A. Ni-bi co-doped TiO₂ as highly visible light response nano-photocatalyst for CO₂ photo-reduction in a batch photo-reactor. *J.CO₂ Util.* **2020**, *41*, 101289. [[CrossRef](#)]

187. Poznyak, S.K.; Talapin, D.V.; Kulak, A.I. Structural, optical, and photoelectrochemical properties of nanocrystalline $\text{TiO}_2-\text{In}_2\text{O}_3$ composite solids and films prepared by sol–gel method. *J. Phys. Chem. B* **2001**, *105*, 4816–4823. [[CrossRef](#)]
188. Kuo, Y.; Frye, C.D.; Ikenberry, M.; Klabunde, K.J. Titanium-indium oxy(nitride) with and without RuO_2 loading as photocatalysts for hydrogen production under visible light from water. *Catal. Today* **2013**, *199*, 15–21. [[CrossRef](#)]
189. Ran, J.; Jaroniec, M.; Qiao, S.-Z. Cocatalysts in semiconductor-based photocatalytic CO_2 reduction: Achievements, challenges, and opportunities. *Adv. Mater.* **2018**, *30*, 1704649. [[CrossRef](#)]
190. Wang, W.-N.; An, W.-J.; Ramalingam, B.; Mukherjee, S.; Niedzwiedzki, D.M.; Gangopadhyay, S.; Biswas, P. Size and structure matter: Enhanced CO_2 photoreduction efficiency by size-resolved ultrafine pt nanoparticles on TiO_2 single crystals. *J. Am. Chem. Soc.* **2012**, *134*, 11276–11281. [[CrossRef](#)]
191. Xie, S.; Wang, Y.; Zhang, Q.; Deng, W.; Wang, Y. MgO - and pt-promoted TiO_2 as an efficient photocatalyst for the preferential reduction of carbon dioxide in the presence of water. *ACS Catal.* **2014**, *4*, 3644–3653. [[CrossRef](#)]
192. Feng, X.; Sloppy, J.D.; LaTempa, T.J.; Paulose, M.; Komarneni, S.; Bao, N.; Grimes, C.A. Synthesis and deposition of ultrafine pt nanoparticles within high aspect ratio TiO_2 nanotube arrays: Application to the photocatalytic reduction of carbon dioxide. *J. Mater. Chem.* **2011**, *21*, 13429–13433. [[CrossRef](#)]
193. Tasibihi, M.; Fresno, F.; Simon, U.; Villar-García, I.J.; Pérez-Dieste, V.; Escudero, C.; de la Peña O’Shea, V.A. On the selectivity of CO_2 photoreduction towards CH_4 using pt/ TiO_2 catalysts supported on mesoporous silica. *Appl. Catal. B Environ.* **2018**, *239*, 68–76. [[CrossRef](#)]
194. Larimi, A.; Rahimi, M.; Khorasheh, F. Carbonaceous supports decorated with pt– TiO_2 nanoparticles using electrostatic self-assembly method as a highly visible-light active photocatalyst for CO_2 photoreduction. *Renew. Energy* **2020**, *145*, 1862–1869. [[CrossRef](#)]
195. Elahifard, M.R.; Ahmadvand, S.; Mirzanejad, A. Effects of ni-doping on the photo-catalytic activity of TiO_2 anatase and rutile: Simulation and experiment. *Mater. Sci. Semicond. Process.* **2018**, *84*, 10–16. [[CrossRef](#)]
196. Ranjitha, A.; Muthukumarasamy, N.; Thambidurai, M.; Velauthapillai, D.; Balasundaraprabhu, R.; Agilan, S. Fabrication of ni-doped TiO_2 thin film photoelectrode for solar cells. *Sol. Energy* **2014**, *106*, 159–165. [[CrossRef](#)]
197. Yoshinaga, M.; Yamamoto, K.; Sato, N.; Aoki, K.; Morikawa, T.; Muramatsu, A. Remarkably enhanced photocatalytic activity by nickel nanoparticle deposition on sulfur-doped titanium dioxide thin film. *Appl. Catal. B Environ.* **2009**, *87*, 239–244. [[CrossRef](#)]
198. Tseng, H.-H.; Wei, M.-C.; Hsiung, S.-F.; Chiou, C.-W. Degradation of xylene vapor over ni-doped TiO_2 photocatalysts prepared by polyol-mediated synthesis. *Chem. Eng. J.* **2009**, *150*, 160–167. [[CrossRef](#)]
199. Ren, C.; Qiu, W.; Zhang, H.; He, Z.; Chen, Y. Degradation of benzene on $\text{TiO}_2/\text{SiO}_2/\text{Bi}_2\text{O}_3$ photocatalysts under uv and visible light. *J. Mol. Catal. A Chem.* **2015**, *398*, 215–222. [[CrossRef](#)]
200. He, R.A.; Cao, S.; Zhou, P.; Yu, J. Recent advances in visible light bi-based photocatalysts. *Chin. J. Catal.* **2014**, *35*, 989–1007. [[CrossRef](#)]
201. Murcia-López, S.; Hidalgo, M.C.; Navío, J.A. Synthesis, characterization and photocatalytic activity of bi-doped TiO_2 photocatalysts under simulated solar irradiation. *Appl. Catal. A Gen.* **2011**, *404*, 59–67. [[CrossRef](#)]
202. Spadaro, L.; Arena, F.; Negro, P.; Palella, A. Sunfuels from CO_2 exhaust emissions: Insights into the role of photoreactor configuration by the study in laboratory and industrial environment. *J. CO₂ Util.* **2018**, *26*, 445–453. [[CrossRef](#)]
203. Xiong, Z.; Zhao, X.S. Nitrogen-doped titanate-anatase core–shell nanobelts with exposed {101} anatase facets and enhanced visible light photocatalytic activity. *J. Am. Chem. Soc.* **2012**, *134*, 5754–5757. [[CrossRef](#)] [[PubMed](#)]
204. Mittal, A.; Mari, B.; Sharma, S.; Kumari, V.; Maken, S.; Kumari, K.; Kumar, N. Non-metal modified TiO_2 : A step towards visible light photocatalysis. *J. Mater. Sci. Mater. Electron.* **2019**, *30*, 3186–3207. [[CrossRef](#)]
205. Pelaez, M.; Nolan, N.T.; Pillai, S.C.; Seery, M.K.; Falaras, P.; Kontos, A.G.; Dunlop, P.S.M.; Hamilton, J.W.J.; Byrne, J.A.; O’Shea, K.; et al. A review on the visible light active titanium dioxide photocatalysts for environmental applications. *Appl. Catal. B Environ.* **2012**, *125*, 331–349. [[CrossRef](#)]
206. Morikawa, T.; Asahi, R.; Ohwaki, T.; Aoki, K.; Taga, Y. Band-gap narrowing of titanium dioxide by nitrogen doping. *Jpn. J. Appl. Phys.* **2001**, *40*, L561–L563. [[CrossRef](#)]
207. Matějová, L.; Kočí, K.; Tropová, I.; Šihor, M.; Edelmannová, M.; Lang, J.; Čapek, L.; Matěj, Z.; Kuśtrowski, P.; Obalová, L. TiO_2 and nitrogen doped TiO_2 prepared by different methods; on the (micro)structure and photocatalytic activity in CO_2 reduction and N_2O decomposition. *J. Nanosci. Nanotechnol.* **2018**, *18*, 688–698. [[CrossRef](#)]
208. Li, M.; Wang, M.; Zhu, L.; Li, Y.; Yan, Z.; Shen, Z.; Cao, X. Facile microwave assisted synthesis of n-rich carbon quantum dots/dual-phase TiO_2 heterostructured nanocomposites with high activity in CO_2 photoreduction. *Appl. Catal. B Environ.* **2018**, *231*, 269–276. [[CrossRef](#)]
209. Zeng, S.; Zhang, X.; Bai, L.; Zhang, X.; Wang, H.; Wang, J.; Bao, D.; Li, M.; Liu, X.; Zhang, S. Ionic-liquid-based CO_2 capture systems: Structure, interaction and process. *Chem. Rev.* **2017**, *117*, 9625–9673. [[CrossRef](#)]
210. Sheridan, Q.R.; Schneider, W.F.; Maginn, E.J. Role of molecular modeling in the development of CO_2 –reactive ionic liquids. *Chem. Rev.* **2018**, *118*, 5242–5260. [[CrossRef](#)]
211. Rebecca, S.; Miguel, T.; Katherine, B.; Nora, H. Reduction of carbon dioxide to formate at low overpotential using a superbase ionic liquid. *Angew. Chem. Int. Ed.* **2015**, *127*, 14370–14374.
212. Lin, J.; Ding, Z.; Hou, Y.; Wang, X. Ionic liquid co-catalyzed artificial photosynthesis of CO. *Sci. Rep.* **2013**, *3*, 1056. [[CrossRef](#)]

213. Chen, Y.; Zhao, Y.; Yu, B.; Wu, Y.; Yu, X.; Guo, S.; Han, B.; Liu, Z. Visible light-driven photoreduction of CO₂ to CH₄ over TiO₂ using a multiple-site ionic liquid as an absorbent and photosensitizer. *ACS Sustain. Chem. Eng.* **2020**, *8*, 9088–9094. [CrossRef]
214. Banerjee, S.; Mohapatra, S.K.; Das, P.P.; Misra, M. Synthesis of coupled semiconductor by filling 1d TiO₂ nanotubes with cds. *Chem. Mater.* **2008**, *20*, 6784–6791. [CrossRef]
215. Shi, L.; Li, C.; Gu, H.; Fang, D. Morphology and properties of ultrafine SnO₂–TiO₂ coupled semiconductor particles. *Mater. Chem. Phys.* **2000**, *62*, 62–67. [CrossRef]
216. Xu, Y.-F.; Wang, X.-D.; Liao, J.-F.; Chen, B.-X.; Chen, H.-Y.; Kuang, D.-B. Amorphous-TiO₂-encapsulated CsPbBr₃ nanocrystal composite photocatalyst with enhanced charge separation and CO₂ fixation. *Adv. Mater. Interfaces* **2018**, *5*, 1801015. [CrossRef]
217. Crake, A.; Christoforidis, K.C.; Godin, R.; Moss, B.; Kafizas, A.; Zafeiratos, S.; Durrant, J.R.; Petit, C. Titanium dioxide/carbon nitride nanosheet nanocomposites for gas phase CO₂ photoreduction under uv-visible irradiation. *Appl. Catal. B Environ.* **2019**, *242*, 369–378. [CrossRef]
218. Tan, J.Z.Y.; Xia, F.; Maroto-Valer, M.M. Raspberry-like microspheres of core–shell Cr₂O₃@TiO₂ nanoparticles for CO₂ photoreduction. *ChemSusChem* **2019**, *12*, 5246–5252. [CrossRef]
219. Iqbal, F.; Mumtaz, A.; Shahabuddin, S.; Abd Mutalib, M.I.; Shaharun, M.S.; Nguyen, T.D.; Khan, M.R.; Abdullah, B. Photocatalytic reduction of CO₂ to methanol over ZnFe₂O₄/TiO₂ (p–n) heterojunctions under visible light irradiation. *J. Chem. Technol. Biotechnol.* **2020**, *95*, 2208–2221. [CrossRef]
220. Sadeghi, N.; Sillanpää, M. High selective photocatalytic CO₂ conversion into liquid solar fuel over a cobalt porphyrin-based metal–organic framework. *Photochem. Photobiol. Sci.* **2021**, *20*, 391–399. [CrossRef]
221. Li, R.; Zhang, W.; Zhou, K. Metal–organic-framework-based catalysts for photoreduction of CO₂. *Adv. Mater.* **2018**, *30*, 1705512. [CrossRef]
222. Llabrés i Xamena, F.X.; Corma, A.; Garcia, H. Applications for metal–organic frameworks (mofs) as quantum dot semiconductors. *J. Phys. Chem. C* **2007**, *111*, 80–85. [CrossRef]
223. Khajavi, H.; Gascon, J.; Schins, J.M.; Siebbeles, L.D.A.; Kapteijn, F. Unraveling the optoelectronic and photochemical behavior of zn4o-based metal organic frameworks. *J. Phys. Chem. C* **2011**, *115*, 12487–12493. [CrossRef]
224. Fu, Y.; Sun, D.; Chen, Y.; Huang, R.; Ding, Z.; Fu, X.; Li, Z. An amine-functionalized titanium metal–organic framework photocatalyst with visible-light-induced activity for CO₂ reduction. *Angew. Chem. Int. Ed.* **2012**, *51*, 3364–3367. [CrossRef]
225. Sun, D.; Fu, Y.; Liu, W.; Ye, L.; Wang, D.; Yang, L.; Fu, X.; Li, Z. Studies on photocatalytic CO₂ reduction over nh2-uio-66(zr) and its derivatives: Towards a better understanding of photocatalysis on metal–organic frameworks. *Chem. A Eur. J.* **2013**, *19*, 14279–14285. [CrossRef]
226. Wang, D.; Huang, R.; Liu, W.; Sun, D.; Li, Z. Fe-based mofs for photocatalytic CO₂ reduction: Role of coordination unsaturated sites and dual excitation pathways. *ACS Catal.* **2014**, *4*, 4254–4260. [CrossRef]
227. Li, S.; Huo, F. Metal–organic framework composites: From fundamentals to applications. *Nanoscale* **2015**, *7*, 7482–7501. [CrossRef]
228. Blanco, L.A.; Gracia, F. 3–2d structures for CO₂ utilization. In *Nanomaterials for Sustainable Energy and Environmental Remediation*; Naushad, M., Saravanan, R., Raju, K., Eds.; Elsevier: Amsterdam, The Netherlands, 2020; pp. 47–58.
229. Wu, J.; Wen, C.; Zou, X.; Jimenez, J.; Sun, J.; Xia, Y.; Fonseca Rodrigues, M.-T.; Vinod, S.; Zhong, J.; Chopra, N.; et al. Carbon dioxide hydrogenation over a metal-free carbon-based catalyst. *ACS Catal.* **2017**, *7*, 4497–4503. [CrossRef]
230. Kumar, A.; Xu, Q. Two-dimensional layered materials as catalyst supports. *ChemNanoMat* **2018**, *4*, 28–40. [CrossRef]
231. Liu, Q.; Low, Z.-X.; Li, L.; Razmjou, A.; Wang, K.; Yao, J.; Wang, H. Zif-8/zn2geo4 nanorods with an enhanced CO₂ adsorption property in an aqueous medium for photocatalytic synthesis of liquid fuel. *J. Mater. Chem. A* **2013**, *1*, 11563–11569. [CrossRef]
232. Wang, S.; Lin, J.; Wang, X. Semiconductor–redox catalysis promoted by metal–organic frameworks for CO₂ reduction. *Phys. Chem. Chem. Phys.* **2014**, *16*, 14656–14660. [CrossRef]
233. Li, R.; Hu, J.; Deng, M.; Wang, H.; Wang, X.; Hu, Y.; Jiang, H.-L.; Jiang, J.; Zhang, Q.; Xie, Y.; et al. Integration of an inorganic semiconductor with a metal–organic framework: A platform for enhanced gaseous photocatalytic reactions. *Adv. Mater.* **2014**, *26*, 4783–4788. [CrossRef] [PubMed]
234. Izumi, Y. Recent advances (2012–2015) in the photocatalytic conversion of carbon dioxide to fuels using solar energy: Feasibility for a new energy. In *Advances in CO₂ Capture, Sequestration, and Conversion*; American Chemical Society: Washington, DC, USA, 2015; Volume 1194, pp. 1–46.
235. Lai, L.; Chen, L.; Zhan, D.; Sun, L.; Liu, J.; Lim, S.H.; Poh, C.K.; Shen, Z.; Lin, J. One-step synthesis of nh2-graphene from in situ graphene-oxide reduction and its improved electrochemical properties. *Carbon* **2011**, *49*, 3250–3257. [CrossRef]
236. Dikin, D.A.; Stankovich, S.; Zimney, E.J.; Piner, R.D.; Dommett, G.H.B.; Evmenenko, G.; Nguyen, S.T.; Ruoff, R.S. Preparation and characterization of graphene oxide paper. *Nature* **2007**, *448*, 457–460. [CrossRef] [PubMed]
237. Jahan, M.; Bao, Q.; Loh, K.P. Electrocatalytically active graphene–porphyrin mof composite for oxygen reduction reaction. *J. Am. Chem. Soc.* **2012**, *134*, 6707–6713. [CrossRef]
238. Sadeghi, N.; Sharifnia, S.; Do, T.-O. Enhanced CO₂ photoreduction by a graphene–porphyrin metal–organic framework under visible light irradiation. *J. Mater. Chem. A* **2018**, *6*, 18031–18035. [CrossRef]
239. Zhou, A.; Dou, Y.; Zhao, C.; Zhou, J.; Wu, X.-Q.; Li, J.-R. A leaf-branch TiO₂/carbon@ mof composite for selective CO₂ photoreduction. *Appl. Catal. B Environ.* **2020**, *264*, 118519. [CrossRef]
240. Lohse, M.S.; Bein, T. Covalent organic frameworks: Structures, synthesis, and applications. *Adv. Funct. Mater.* **2018**, *28*, 1705553. [CrossRef]

241. Shi, R.; Lv, D.; Chen, Y.; Wu, H.; Liu, B.; Xia, Q.; Li, Z. Highly selective adsorption separation of light hydrocarbons with a porphyrinic zirconium metal-organic framework pcn-224. *Sep. Purif. Technol.* **2018**, *207*, 262–268. [[CrossRef](#)]
242. Wang, L.; Jin, P.; Huang, J.; She, H.; Wang, Q. Integration of copper(II)-porphyrin zirconium metal-organic framework and titanium dioxide to construct z-scheme system for highly improved photocatalytic CO₂ reduction. *ACS Sustain. Chem. Eng.* **2019**, *7*, 15660–15670. [[CrossRef](#)]
243. Ahmed, I.; Jhung, S.H. Composites of metal-organic frameworks: Preparation and application in adsorption. *Mater. Today* **2014**, *17*, 136–146. [[CrossRef](#)]
244. Schröder, F.; Henke, S.; Zhang, X.; Fischer, R.A. Simultaneous gas-phase loading of mof-5 with two metal precursors: Towards bimetallics@mof. *EurJIC* **2009**, *2009*, 3131–3140. [[CrossRef](#)]
245. Sun, D.; Liu, W.; Fu, Y.; Fang, Z.; Sun, F.; Fu, X.; Zhang, Y.; Li, Z. Noble metals can have different effects on photocatalysis over metal-organic frameworks (mofs): A case study on m/nh2-mil-125(ti) (m=pt and au). *Chem. A Eur. J.* **2014**, *20*, 4780–4788. [[CrossRef](#)]
246. Call, A.; Cibian, M.; Yamamoto, K.; Nakazono, T.; Yamauchi, K.; Sakai, K. Highly efficient and selective photocatalytic CO₂ reduction to co in water by a cobalt porphyrin molecular catalyst. *ACS Catal.* **2019**, *9*, 4867–4874. [[CrossRef](#)]
247. Zhang, J.; Grzelczak, M.; Hou, Y.; Maeda, K.; Domen, K.; Fu, X.; Antonietti, M.; Wang, X. Photocatalytic oxidation of water by polymeric carbon nitride nanohybrids made of sustainable elements. *Chem. Sci.* **2012**, *3*, 443–446. [[CrossRef](#)]
248. Wang, S.; Yao, W.; Lin, J.; Ding, Z.; Wang, X. Cobalt imidazolate metal-organic frameworks photosplit CO₂ under mild reaction conditions. *Angew. Chem.* **2014**, *126*, 1052–1056. [[CrossRef](#)]
249. Chambers, M.B.; Wang, X.; Elgrishi, N.; Hendon, C.H.; Walsh, A.; Bonnefoy, J.; Canivet, J.; Quadrelli, E.A.; Farrusseng, D.; Mellot-Draznieks, C.; et al. Photocatalytic carbon dioxide reduction with rhodium-based catalysts in solution and heterogenized within metal-organic frameworks. *ChemSusChem* **2015**, *8*, 603–608. [[CrossRef](#)]
250. Sadeghi, N.; Sharifnia, S.; Sheikh Arabi, M. A porphyrin-based metal organic framework for high rate photoreduction of CO₂ to CH₄ in gas phase. *J. CO₂ Util.* **2016**, *16*, 450–457. [[CrossRef](#)]
251. Lee, J.H.; Lee, H.; Kang, M. Remarkable photoconversion of carbon dioxide into methane using bi-doped TiO₂ nanoparticles prepared by a conventional sol-gel method. *Mater. Lett.* **2016**, *178*, 316–319. [[CrossRef](#)]
252. Torres, J.A.; Nogueira, A.E.; da Silva, G.T.S.T.; Lopes, O.F.; Wang, Y.; He, T.; Ribeiro, C. Enhancing TiO₂ activity for CO₂ photoreduction through mgo decoration. *J. CO₂ Util.* **2020**, *35*, 106–114. [[CrossRef](#)]
253. Feng, S.; Zhao, J.; Bai, Y.; Liang, X.; Wang, T.; Wang, C. Facile synthesis of mo-doped TiO₂ for selective photocatalytic CO₂ reduction to methane: Promoted H₂O dissociation by mo doping. *J. CO₂ Util.* **2020**, *38*, 1–9. [[CrossRef](#)]
254. Chen, M.; Wu, J.; Lu, C.; Luo, X.; Huang, Y.; Jin, B.; Gao, H.; Zhang, X.; Argyle, M.; Liang, Z. Photoreduction of CO₂ in the presence of CH₄ over g-c3n4 modified with TiO₂ nanoparticles at room temperature. *Green Energy Environ.* **2020**, *6*, 938–951. [[CrossRef](#)]
255. Lee, Y.; Kim, S.; Kang, J.K.; Cohen, S.M. Photocatalytic CO₂ reduction by a mixed metal (zr/ti), mixed ligand metal-organic framework under visible light irradiation. *Chem. Commun.* **2015**, *51*, 5735–5738. [[CrossRef](#)]
256. Yan, S.; Ouyang, S.; Xu, H.; Zhao, M.; Zhang, X.; Ye, J. Co-zif-9/tio 2 nanostructure for superior co 2 photoreduction activity. *J. Mater. Chem. A* **2016**, *4*, 15126–15133. [[CrossRef](#)]
257. He, X.; Gan, Z.; Fisenko, S.; Wang, D.; El-Kaderi, H.M.; Wang, W.-N. Rapid formation of metal-organic frameworks (mofs) based nanocomposites in microdroplets and their applications for CO₂ photoreduction. *ACS Appl. Mater. Interfaces* **2017**, *9*, 9688–9698. [[CrossRef](#)]
258. Wang, M.; Wang, D.; Li, Z. Self-assembly of cpo-27-mg/TiO₂ nanocomposite with enhanced performance for photocatalytic CO₂ reduction. *Appl. Catal. B Environ.* **2016**, *183*, 47–52. [[CrossRef](#)]
259. Shi, L.; Wang, T.; Zhang, H.; Chang, K.; Ye, J. Electrostatic self-assembly of nanosized carbon nitride nanosheet onto a zirconium metal-organic framework for enhanced photocatalytic CO₂ reduction. *Adv. Funct. Mater.* **2015**, *25*, 5360–5367. [[CrossRef](#)]
260. Crake, A.; Christoforidis, K.C.; Kafizas, A.; Zafeiratos, S.; Petit, C. CO₂ capture and photocatalytic reduction using bifunctional TiO₂/mof nanocomposites under uv-vis irradiation. *Appl. Catal. B Environ.* **2017**, *210*, 131–140. [[CrossRef](#)]
261. Ulagappan, N.; Frei, H. Mechanistic study of CO₂ photoreduction in ti silicalite molecular sieve by ft-ir spectroscopy. *J. Phys. Chem. A* **2000**, *104*, 7834–7839. [[CrossRef](#)]
262. Chen, J.; Xin, F.; Qin, S.; Yin, X. Photocatalytically reducing CO₂ to methyl formate in methanol over zns and ni-doped zns photocatalysts. *Chem. Eng. J.* **2013**, *230*, 506–512. [[CrossRef](#)]
263. Chen, J.; Xin, F.; Yin, X.; Xiang, T.; Wang, Y. Synthesis of hexagonal and cubic znin2s4 nanosheets for the photocatalytic reduction of CO₂ with methanol. *RSC Adv.* **2015**, *5*, 3833–3839. [[CrossRef](#)]
264. Sadeghi, N.; Sharifnia, S.; Do, T.-O. Optimization and modeling of CO₂ photoconversion using a response surface methodology with porphyrin-based metal organic framework. *React. Kinet. Mech. Catal.* **2018**, *125*, 411–431. [[CrossRef](#)]
265. Li, G.; Ciston, S.; Saponjic, Z.V.; Chen, L.; Dimitrijevic, N.M.; Rajh, T.; Gray, K.A. Synthesizing mixed-phase TiO₂ nanocomposites using a hydrothermal method for photo-oxidation and photoreduction applications. *J. Catal.* **2008**, *253*, 105–110. [[CrossRef](#)]
266. Sun, D.; Liu, W.; Qiu, M.; Zhang, Y.; Li, Z. Introduction of a mediator for enhancing photocatalytic performance via post-synthetic metal exchange in metal-organic frameworks (mofs). *Chem. Commun.* **2015**, *51*, 2056–2059. [[CrossRef](#)] [[PubMed](#)]
267. Tu, W.; Zhou, Y.; Zou, Z. Photocatalytic conversion of CO₂ into renewable hydrocarbon fuels: State-of-the-art accomplishment, challenges, and prospects. *Adv. Mater.* **2014**, *26*, 4607–4626. [[CrossRef](#)] [[PubMed](#)]

268. Takata, T.; Jiang, J.; Sakata, Y.; Nakabayashi, M.; Shibata, N.; Nandal, V.; Seki, K.; Hisatomi, T.; Domen, K. Photocatalytic water splitting with a quantum efficiency of almost unity. *Nature* **2020**, *581*, 411–414. [[CrossRef](#)]
269. Ham, Y.; Hisatomi, T.; Goto, Y.; Moriya, Y.; Sakata, Y.; Yamakata, A.; Kubota, J.; Domen, K. Flux-mediated doping of srtio₃ photocatalysts for efficient overall water splitting. *J. Mater. Chem. A* **2016**, *4*, 3027–3033. [[CrossRef](#)]
270. Kurashige, W.; Mori, Y.; Ozaki, S.; Kawachi, M.; Hossain, S.; Kawasaki, T.; Shearer, C.J.; Iwase, A.; Metha, G.F.; Yamazoe, S. Activation of water-splitting photocatalysts by loading with ultrafine rh-cr mixed-oxide cocatalyst nanoparticles. *Angew. Chem. Int. Ed.* **2020**, *59*, 7076–7082. [[CrossRef](#)]
271. Fu, S.; Liu, X.; Ran, J.; Jiao, Y. Theoretical considerations on activity of the electrochemical CO₂ reduction on metal single-atom catalysts with asymmetrical active sites. *Catal. Today* **2021**. [[CrossRef](#)]
272. Wang, Q.; Zhang, Y.; Lin, H.; Zhu, J. Recent advances in metal–organic frameworks for photo-/electrocatalytic CO₂ reduction. *Chem. A Eur. J.* **2019**, *25*, 14026–14035. [[CrossRef](#)]
273. Li, J.; Chen, G.; Zhu, Y.; Liang, Z.; Pei, A.; Wu, C.-L.; Wang, H.; Lee, H.R.; Liu, K.; Chu, S. Efficient electrocatalytic CO₂ reduction on a three-phase interface. *Nat. Catal.* **2018**, *1*, 592–600. [[CrossRef](#)]
274. Trickett, C.A.; Helal, A.; Al-Maythalony, B.A.; Yamani, Z.H.; Cordova, K.E.; Yaghi, O.M. The chemistry of metal–organic frameworks for CO₂ capture, regeneration and conversion. *Nat. Rev. Mater.* **2017**, *2*, 17045. [[CrossRef](#)]
275. Loiudice, A.; Lobaccaro, P.; Kamali, E.A.; Thao, T.; Huang, B.H.; Ager, J.W.; Buonsanti, R. Tailoring copper nanocrystals towards C₂ products in electrochemical CO₂ reduction. *Angew. Chem. Int. Ed.* **2016**, *55*, 5789–5792. [[CrossRef](#)]
276. Kimura, K.W.; Fritz, K.E.; Kim, J.; Suntivich, J.; Abruna, H.D.; Hanrath, T. Controlled selectivity of CO₂ reduction on copper by pulsing the electrochemical potential. *ChemSusChem* **2018**, *11*, 1781–1786. [[CrossRef](#)]
277. Park, S.; Wijaya, D.T.; Na, J.; Lee, C.W. Towards the large-scale electrochemical reduction of carbon dioxide. *Catalysts* **2021**, *11*, 253. [[CrossRef](#)]
278. Gu, Z.-G.; Zhang, J. Epitaxial growth and applications of oriented metal–organic framework thin films. *Coord. Chem. Rev.* **2019**, *378*, 513–532. [[CrossRef](#)]
279. Lei, Z.; Xue, Y.; Chen, W.; Qiu, W.; Zhang, Y.; Horike, S.; Tang, L. Mofs-based heterogeneous catalysts: New opportunities for energy-related CO₂ conversion. *Adv. Energy Mater.* **2018**, *8*, 1801587. [[CrossRef](#)]
280. Zhang, H.-X.; Liu, M.; Wen, T.; Zhang, J. Synthetic design of functional boron imidazolate frameworks. *Coord. Chem. Rev.* **2016**, *307*, 255–266. [[CrossRef](#)]
281. Yang, M.; Zhou, Y.-N.; Cao, Y.-N.; Tong, Z.; Dong, B.; Chai, Y.-M. Advances and challenges of fe-mofs based materials as electrocatalysts for water splitting. *Appl. Mater. Today* **2020**, *20*, 100692. [[CrossRef](#)]
282. Hod, I.; Sampson, M.D.; Deria, P.; Kubiak, C.P.; Farha, O.K.; Hupp, J.T. Fe-porphyrin-based metal–organic framework films as high-surface concentration, heterogeneous catalysts for electrochemical reduction of CO₂. *ACS Catal.* **2015**, *5*, 6302–6309. [[CrossRef](#)]
283. Dong, B.-X.; Qian, S.-L.; Bu, F.-Y.; Wu, Y.-C.; Feng, L.-G.; Teng, Y.-L.; Liu, W.-L.; Li, Z.-W. Electrochemical reduction of CO₂ to co by a heterogeneous catalyst of fe–porphyrin-based metal–organic framework. *ACS Appl. Energy Mater.* **2018**, *1*, 4662–4669. [[CrossRef](#)]
284. Wang, Y.-R.; Huang, Q.; He, C.-T.; Chen, Y.; Liu, J.; Shen, F.-C.; Lan, Y.-Q. Oriented electron transmission in polyoxometalate–metalloporphyrin organic framework for highly selective electroreduction of CO₂. *Nat. Commun.* **2018**, *9*, 4466. [[CrossRef](#)] [[PubMed](#)]
285. Hori, Y.; Murata, A.; Takahashi, R. Formation of hydrocarbons in the electrochemical reduction of carbon dioxide at a copper electrode in aqueous solution. *J. Chem. Soc. Faraday Trans. 1 Phys. Chem. Condens. Phases* **1989**, *85*, 2309–2326. [[CrossRef](#)]
286. Watanabe, M.; Shibata, M.; Kato, A.; Azuma, M.; Sakata, T. Design of alloy electrocatalysts for CO₂ reduction: III. The selective and reversible reduction of on cu alloy electrodes. *J. Electrochem. Soc.* **1991**, *138*, 3382–3389. [[CrossRef](#)]
287. Senthil Kumar, R.; Senthil Kumar, S.; Anbu Kulandainathan, M. Highly selective electrochemical reduction of carbon dioxide using cu based metal organic framework as an electrocatalyst. *Electrochim. Commun.* **2012**, *25*, 70–73. [[CrossRef](#)]
288. Hinogami, R.; Yotsuhashi, S.; Deguchi, M.; Zenitani, Y.; Hashiba, H.; Yamada, Y. Electrochemical reduction of carbon dioxide using a copper rubeanate metal organic framework. *ECS Electrochem. Lett.* **2012**, *1*, H17. [[CrossRef](#)]
289. Shao, P.; Yi, L.; Chen, S.; Zhou, T.; Zhang, J. Metal-organic frameworks for electrochemical reduction of carbon dioxide: The role of metal centers. *J. Energy Chem.* **2020**, *40*, 156–170. [[CrossRef](#)]
290. Wang, H.; Gurau, G.; Rogers, R.D. Ionic liquid processing of cellulose. *Chem. Soc. Rev.* **2012**, *41*, 1519–1537. [[CrossRef](#)]
291. Lei, Z.; Dai, C.; Chen, B. Gas solubility in ionic liquids. *Chem. Rev.* **2014**, *114*, 1289–1326. [[CrossRef](#)]
292. Lui, M.Y.; Crowhurst, L.; Hallett, J.P.; Hunt, P.A.; Niedermeyer, H.; Welton, T. Salts dissolved in salts: Ionic liquid mixtures. *Chem. Sci.* **2011**, *2*, 1491–1496. [[CrossRef](#)]
293. Kang, X.; Zhu, Q.; Sun, X.; Hu, J.; Zhang, J.; Liu, Z.; Han, B. Highly efficient electrochemical reduction of CO₂ to CH₄ in an ionic liquid using a metal–organic framework cathode. *Chem. Sci.* **2016**, *7*, 266–273. [[CrossRef](#)]
294. Liu, P.-F.; Tao, K.; Li, G.-C.; Wu, M.-K.; Zhu, S.-R.; Yi, F.-Y.; Zhao, W.-N.; Han, L. In situ growth of zif-8 nanocrystals on layered double hydroxide nanosheets for enhanced CO₂ capture. *Dalton Trans.* **2016**, *45*, 12632–12635. [[CrossRef](#)]
295. Wang, Y.; Hou, P.; Wang, Z.; Kang, P. Zinc imidazolate metal–organic frameworks (zif-8) for electrochemical reduction of CO₂ to co. *ChemPhysChem* **2017**, *18*, 3142–3147. [[CrossRef](#)]

296. Ye, L.; Liu, J.; Gao, Y.; Gong, C.; Addicoat, M.; Heine, T.; Wöll, C.; Sun, L. Highly oriented mof thin film-based electrocatalytic device for the reduction of CO₂ to co exhibiting high faradaic efficiency. *J. Mater. Chem. A* **2016**, *4*, 15320–15326. [[CrossRef](#)]
297. Jiang, X.; Wu, H.; Chang, S.; Si, R.; Miao, S.; Huang, W.; Li, Y.; Wang, G.; Bao, X. Boosting CO₂ electroreduction over layered zeolitic imidazolate frameworks decorated with ag2o nanoparticles. *J. Mater. Chem. A* **2017**, *5*, 19371–19377. [[CrossRef](#)]
298. Zhang, B.; Zhang, J. Rational design of cu-based electrocatalysts for electrochemical reduction of carbon dioxide. *J. Energy Chem.* **2017**, *26*, 1050–1066. [[CrossRef](#)]
299. Yoshio, H.; Katsuhei, K.; Shin, S. Production of co and CH4 in electrochemical reduction of CO₂ at metal electrodes in aqueous hydrogencarbonate solution. *Chem. Lett.* **1985**, *14*, 1695–1698.
300. Hori, Y.; Murata, A.; Takahashi, R.; Suzuki, S. Electroreduction of carbon monoxide to methane and ethylene at a copper electrode in aqueous solutions at ambient temperature and pressure. *J. Am. Chem. Soc.* **1987**, *109*, 5022–5023. [[CrossRef](#)]
301. Zhao, C.; Dai, X.; Yao, T.; Chen, W.; Wang, X.; Wang, J.; Yang, J.; Wei, S.; Wu, Y.; Li, Y. Ionic exchange of metal–organic frameworks to access single nickel sites for efficient electroreduction of CO₂. *J. Am. Chem. Soc.* **2017**, *139*, 8078–8081. [[CrossRef](#)]
302. Zhang, X.; Liu, J.-X.; Zijlstra, B.; Filot, I.A.W.; Zhou, Z.; Sun, S.; Hensen, E.J.M. Optimum cu nanoparticle catalysts for CO₂ hydrogenation towards methanol. *Nano Energy* **2018**, *43*, 200–209. [[CrossRef](#)]
303. Reske, R.; Mistry, H.; Behafarid, F.; Roldan Cuenya, B.; Strasser, P. Particle size effects in the catalytic electroreduction of CO₂ on cu nanoparticles. *J. Am. Chem. Soc.* **2014**, *136*, 6978–6986. [[CrossRef](#)]
304. Nam, D.-H.; Bushuyev, O.S.; Li, J.; De Luna, P.; Seifitokaldani, A.; Dinh, C.-T.; García de Arquer, F.P.; Wang, Y.; Liang, Z.; Proppe, A.H.; et al. Metal–organic frameworks mediate cu coordination for selective CO₂ electroreduction. *J. Am. Chem. Soc.* **2018**, *140*, 11378–11386. [[CrossRef](#)] [[PubMed](#)]
305. Hwang, S.-M.; Choi, S.Y.; Youn, M.H.; Lee, W.; Park, K.T.; Gothandapani, K.; Grace, A.N.; Jeong, S.K. Investigation on electroreduction of CO₂ to formic acid using cu3(btc)2 metal–organic framework (cu-mof) and graphene oxide. *ACS Omega* **2020**, *5*, 23919–23930. [[CrossRef](#)] [[PubMed](#)]
306. Rayer, A.V.; Reid, E.; Kataria, A.; Luz, I.; Thompson, S.J.; Lail, M.; Zhou, J.; Soukri, M. Electrochemical carbon dioxide reduction to isopropanol using novel carbonized copper metal organic framework derived electrodes. *J. CO2 Util.* **2020**, *39*, 101159. [[CrossRef](#)]
307. Wang, X.; Chen, Z.; Zhao, X.; Yao, T.; Chen, W.; You, R.; Zhao, C.; Wu, G.; Wang, J.; Huang, W. Regulation of coordination number over single co sites: Triggering the efficient electroreduction of CO₂. *Angew. Chem.* **2018**, *130*, 1962–1966. [[CrossRef](#)]
308. Ye, Y.; Cai, F.; Li, H.; Wu, H.; Wang, G.; Li, Y.; Miao, S.; Xie, S.; Si, R.; Wang, J.; et al. Surface functionalization of zif-8 with ammonium ferric citrate toward high exposure of fe-n active sites for efficient oxygen and carbon dioxide electroreduction. *Nano Energy* **2017**, *38*, 281–289. [[CrossRef](#)]
309. Zhu, M.; Chen, J.; Huang, L.; Ye, R.; Xu, J.; Han, Y.-F. Covalently grafting cobalt porphyrin onto carbon nanotubes for efficient CO₂ electroreduction. *Angew. Chem. Int. Ed.* **2019**, *58*, 6595–6599. [[CrossRef](#)]
310. Kim, M.K.; Kim, H.J.; Lim, H.; Kwon, Y.; Jeong, H.M. Metal–organic framework-mediated strategy for enhanced methane production on copper nanoparticles in electrochemical CO₂ reduction. *Electrochim. Acta* **2019**, *306*, 28–34. [[CrossRef](#)]
311. Albo, J.; Perfecto-Irigaray, M.; Beobide, G.; Irabien, A. Cu/bi metal–organic framework-based systems for an enhanced electrochemical transformation of CO₂ to alcohols. *J. CO2 Util.* **2019**, *33*, 157–165. [[CrossRef](#)]
312. Zhang, H.; Li, J.; Xi, S.; Du, Y.; Hai, X.; Wang, J.; Xu, H.; Wu, G.; Zhang, J.; Lu, J. A graphene-supported single-atom fen5 catalytic site for efficient electrochemical CO₂ reduction. *Angew. Chem.* **2019**, *131*, 15013–15018. [[CrossRef](#)]
313. Huang, J.; Mensi, M.; Oveisi, E.; Mantella, V.; Buonsanti, R. Structural sensitivities in bimetallic catalysts for electrochemical CO₂ reduction revealed by ag–cu nanodimers. *J. Am. Chem. Soc.* **2019**, *141*, 2490–2499. [[CrossRef](#)]
314. Dou, S.; Song, J.; Xi, S.; Du, Y.; Wang, J.; Huang, Z.F.; Xu, Z.J.; Wang, X. Boosting electrochemical CO₂ reduction on metal–organic frameworks via ligand doping. *Angew. Chem.* **2019**, *131*, 4081–4085. [[CrossRef](#)]
315. Vasileff, A.; Zhi, X.; Xu, C.; Ge, L.; Jiao, Y.; Zheng, Y.; Qiao, S.-Z. Selectivity control for electrochemical CO₂ reduction by charge redistribution on the surface of copper alloys. *ACS Catal.* **2019**, *9*, 9411–9417. [[CrossRef](#)]
316. Deng, W.; Zhang, L.; Li, L.; Chen, S.; Hu, C.; Zhao, Z.-J.; Wang, T.; Gong, J. Crucial role of surface hydroxyls on the activity and stability in electrochemical CO₂ reduction. *J. Am. Chem. Soc.* **2019**, *141*, 2911–2915. [[CrossRef](#)]
317. Daiyan, R.; Lu, X.; Tan, X.; Zhu, X.; Chen, R.; Smith, S.C.; Amal, R. Antipoisoning nickel–carbon electrocatalyst for practical electrochemical CO₂ reduction to co. *ACS Appl. Energy Mater.* **2019**, *2*, 8002–8009. [[CrossRef](#)]
318. Choi, J.; Wagner, P.; Gambhir, S.; Jalili, R.; MacFarlane, D.R.; Wallace, G.G.; Officer, D.L. Steric modification of a cobalt phthalocyanine/graphene catalyst to give enhanced and stable electrochemical CO₂ reduction to co. *ACS Energy Lett.* **2019**, *4*, 666–672. [[CrossRef](#)]
319. Zhou, Y.; Zhou, R.; Zhu, X.; Han, N.; Song, B.; Liu, T.; Hu, G.; Li, Y.; Lu, J.; Li, Y. Mesoporous pdag nanospheres for stable electrochemical CO₂ reduction to formate. *Adv. Mater.* **2020**, *32*, 2000992. [[CrossRef](#)]
320. Lee, M.-Y.; Ringe, S.; Kim, H.; Kang, S.; Kwon, Y. Electric field mediated selectivity switching of electrochemical CO₂ reduction from formate to co on carbon supported sn. *ACS Energy Lett.* **2020**, *5*, 2987–2994. [[CrossRef](#)]
321. Sun, Z.; Ma, T.; Tao, H.; Fan, Q.; Han, B. Fundamentals and challenges of electrochemical CO₂ reduction using two-dimensional materials. *Chem* **2017**, *3*, 560–587. [[CrossRef](#)]
322. Jouny, M.; Luc, W.; Jiao, F. Correction to “general techno-economic analysis of CO₂ electrolysis systems”. *Ind. Eng. Chem. Res.* **2020**, *59*, 8121–8123. [[CrossRef](#)]